Development of quantitative chemical exchange saturation transfer MRI for functional kidney imaging

Inaugural-Dissertation

zur Erlangung des Doktorgrades
der Mathematisch-Naturwissenschaftlichen Fakultät
der Heinrich-Heine-Universität Düsseldorf

vorgelegt von

Julia Stabińska

aus Giżycko

Düsseldorf, August 2020

aus dem Institut für Diagnostische und Interventionelle Radiologie
der Heinrich-Heine-Universität Düsseldorf

Gedruckt mit der Genehmigung der
Mathematisch-Naturwissenschaftlichen Fakultät der
Heinrich-Heine-Universität Düsseldorf

Berichterstatter:
1. Prof. Dr. rer. nat. Hans-Jörg Wittsack
2. Prof. Dr. rer. nat. Axel Görlitz

Tag der müundlichen Prüfung: 05.10.2020

Acknowledgements

An dieser Stelle möchte ich mich bei all denjenigen bedanken, die mich bei der Fertigstellung dieser Dissertation unterstützt haben.

Ein besonderer Dank gilt Prof. Hans-Jörg Wittsack für die umfassende Betreuung und Hilfsbereitschaft während der gesamten Promotion. Das von Ihm mir entgegengebrachte Vertrauen hat es mir ermöglicht, mich persönlich und wissenschaftlich frei zu entwickeln.

Weiterhin bedanke ich mich bei meinem Zweitgutachter, Prof. Axel Görlitz, für die Begutachtung meiner Arbeit und die Hilfestellung bei den formellen Fragen des Promotionsverfahrens.

Prof. Gerald Antoch bin ich dankbar für die Möglichkeit meine Promotion in seinem Institut anzufertigen und die Unterstützung zur Teilnahme an internationalen Konferenzen.

Dr. Anja Müller-Lutz danke ich für die Begeisterung für die CEST-Bildgebung, sehr gute Betreuung der Arbeit und kritische Durchsicht der Manuskripte.

Ein weiterer Dank geht an Dr. Alexandra Ljimani für ihr persönliches Engagement, sowie die fachliche und logistische Hilfestellung bei der Patientenakquise.

Für die gute Kooperation mit dem Forschungszentrum Jülich und die gemeinsame Durchführung der WEX-Experimente möchte ich mich bei Dr. Philipp Neudecker bedanken.

Der gesamten AG Medizinische Physik (Anja Müller-Lutz, Alexandra Ljimani, Eric Bechler, Helge Zöllner, Thomas Thiel, Benedikt Kamp und Frithjof Wickrath) bin ich dankbar für die schöne fünf Jahren, in denen ich mich stets heimisch gefühlt habe.

Auch Erika Rädisch ist an dieser Stelle für ihre Hilfe und Unterhaltung während der zahlreichen MR-Messungen zu danken.

Mein herzlicher Dank gilt außerdem Helge für seinen Rückhalt in den letzten Wochen und die konstruktiven Kommentare zu meiner Dissertation.

Szczególne podziękowania należą się również moim Rodzicom, Dziadkom i Bratu, którzy wspierali mnie na każdym etapie mojej edukacji i pracy naukowej.

Author's Declaration

I, Julia Stabińska, hereby declare, that the work for my dissertation:

Development of quantitative chemical exchange saturation transfer MRI for functional kidney imaging

was realized independently and without using illicit help. Only the declared sources have been used, and all direct and analogous quotes have been marked as such. The work has not been submitted in identical or similar variety at any other institution. This is my first attempt at acquiring a doctoral degree.

Düsseldorf, August 13th 2020

Julia Stabińska

First Authorships

Stabinska J, Cronenberg T, Wittsack HJ, Lanzman RS, Müller-Lutz A. Quantitative pulsed CEST-MRI at a clinical 3T MRI system. Magn Reson Mater Phy. 2017; 30:505–516. doi: 10.1007/s10334-017-0625-0.

Stabinska J, Neudecker P, Ljimani A, Wittsack HJ, Lanzman RS, Müller-Lutz A. Proton exchange in aqueous urea solutions measured by water-exchange (WEX) NMR spectroscopy and chemical exchange saturation transfer (CEST) imaging in vitro. Magn Reson Med. 2019; 82:935–947. doi: 10.1002/mrm.27778

Stabinska J, Müller-Lutz A, Wittsack HJ, Tell C, Rump LC, Ertas N, Antoch G, Ljimani A. Dixon-based CEST MRI in renal transplant recipients: a preliminary study. (*Submitted to Magn Reson Imaging*)

This dissertation is based on these publications. Personal contributions and impact factors are listed in Appendix A, Appendix B, and Appendix C.

Abstract

The kidneys play a crucial role in balancing the body's internal environment. Their primary functions are to filter and remove metabolic waste products, and maintain homeostasis by regulating acid-base balance, fluid volume, and blood pressure. Besides their excretory and osmoregulatory function, the kidneys also produce and secrete various hormones that have a vital role within the human body.

The overall kidney function can be estimated using several non-invasive tests such as serum creatinine, urinalysis, and blood pressure measurements. In addition to these simple screening methods, medical imaging has become a fundamental diagnostic tool in clinical nephrology. Apart from ultrasound and computed tomography, magnetic resonance imaging (MRI) has evolved over the past decades and is now an established modality in renal imaging. MRI relies upon the magnetic properties of hydrogen nuclei in water molecules, whose abundance in the human body enables the generation of a measurable signal. Besides providing high-resolution anatomical images, MRI can also be used for obtaining functional images of tissue-specific physiological parameters. In particular, considerable attention has recently been drawn towards the use of so-called chemical exchange saturation transfer (CEST) imaging as a novel MRI contrast mechanism, in which low-concentration metabolites and proteins can be detected indirectly through the transfer of magnetization from labile solute protons to water protons. The underlying proton exchange mechanism is affected by the metabolite/protein concentration and exchange rate, which, in turn, depends on temperature and pH. CEST MRI offers, therefore, not only the possibility to detect certain metabolites, but can also provide insights into the molecular mechanisms of renal disease.

This dissertation aimed at exploring the potential of CEST MRI for functional kidney imaging. For this purpose, various chemical compounds and kidney metabolites were investigated for their suitability in clinical CEST imaging. A particular focus was placed on urea, which is an important diagnostic marker of renal function. Additionally, different CEST acquisition protocols and quantification methods were evaluated using both simulated and phantom data. Finally, in order to enable the in vivo translation of CEST imaging to human kidney, a new CEST MRI pulse sequence and a post-processing pipeline were developed, and subsequently applied in a clinical cohort of renal transplant recipients.

In the course of this work, the feasibility of quantitative pulsed CEST MRI (qCEST) on clinical MRI systems was tested. To determine exchange parameters associated with CEST, the apparent exchange-dependent relaxation (AREX) metric and Ω-plot method were used. The applicability and accuracy of these two qCEST approaches combined with two different preparation schemes were then analyzed using Bloch-McConnell (BM) simulations for a two pool chemical exchange model, and MRI experiments on creatine aqueous solutions prepared at varying pH and concentrations. Overall it was found that quantitative pulsed CEST MRI is capable to produce reasonable results on clinical scanners when imaging amine protons at intermediate exchange rates between 50 and 530 Hz at 3T.

In a subsequent study, proton exchange properties of urea were characterized using water exchange (WEX) ^{1}H-nuclear magnetic resonance (NMR) spectroscopy at ultrahigh magnetic field strength of 14.1T, and compared with those obtained by the quantitative CEST MRI analysis at 3T. Furthermore, the feasibility of endogenous urea-weighted CEST (urCEST) MRI was evaluated by studying CEST effects from urea and other important abundant kidney metabolites. Both WEX and CEST experiments revealed that the acid- and base-catalyzed exchange between amide protons of urea and water protons is outstandingly slow, especially in the physiological pH range. Nevertheless, this study verified that CEST imaging is sensitive to the pH- and concentration-dependent chemical exchange process in aqueous urea solution. Furthermore, several other chemical compounds with exchangeable protons have been shown to produce a measurable pH-dependent CEST effect at 3T and are expected to contribute to the overall CEST signal measured in the kidney.

In a final study, feasibility of in vivo endogenous CEST imaging in the kidney transplant recipients was evaluated for the first time. For the CEST data acquisition, a multi-echo magnetization transfer (MT)-prepared gradient echo (GRE) MRI sequence was developed. Furthermore, to correct for lipid artifacts in CEST images, the utility of two-point Dixon water-fat separation was explored. With the optimized CEST acquisition and post-processing protocol, it was possible to quantify cortical and medullary CEST effects in the renal tissue. In line with literature, the highest CESTeffect was measured at about 1 ppm downfield of the water resonance, indicating urea as a major contributor to the total CEST signal in the kidney. Moreover, this preliminary work showed that the specificity of endogenous amide proton transfer (APT) contrast in the kidney could be enhanced by applying Dixon-based CEST analysis.

The findings from this dissertation have implications for the understanding of saturation transfer effects from certain chemical compounds and kidney metabolites related to the renal function. The optimized CEST acquisition and post-processing protocol can be used to further investigate the molecular mechanisms underlying kidney disease.

Zusammenfassung

Neben der Reinigung und Entgiftung des Blutes spielen die Nieren eine zentrale Rolle bei der homöostatischen Regelung des Säure-Basen-Haushalts, des Flüssigkeitsvolumen und des Blutdrucks. Darüber hinaus produzieren sie verschiedene Hormone und greifen dadurch in die Regulation des menschlichen Organismus ein.

Die Gesamtnierenfunktion lässt sich anhand relativ einfacher Tests wie z.B. die Bestimmung des Serumkreatinins, Urinanalyse, und Blutdruckmessungen abschätzen. Um jedoch eine seitengetrennte Beurteilung der Nierenfunktion zu ermöglichen, wird die bildgebende Diagnostik in der klinischen Routine eingesetzt. Neben der Sonographie und Computertomographie hat sich die Magnetresonanztomographie (MRT) als ein nichtinvasives Untersuchungsverfahren in der Nierendiagnostik etabliert. Das Prinzip der Magnetresonanzbildgebung beruht auf den magnetischen Eigenschaften der Wasserstoffkerne in freiem und gebundenem Wasser. Dabei bietet die MRT sowohl eine räumlich hochaufgelöste Darstellung der anatomischen Strukturen in lebenden Geweben, als auch die Möglichkeit verschiedene physiologische Parameter zu bestimmen. Beispielweise können niedrig konzentrierte Metabolite oder Proteine anhand ihres Magnetisierungstransfers mit Wasser mittels der Chemical Exchange Saturation Transfer (CEST)-Bildgebung indirekt detektiert werden. Der Protonenaustausch-Prozess, welcher der Methode zugrunde liegt, wird durch die Konzentration des Metaboliten und die chemische Austauschrate beeinflusst. Da die Austausschrate wiederum von der Temperatur und dem pH-Wert abhängt, ermöglicht die CEST-Bildgebung nicht nur die Detektion von Metaboliten oder Proteinen, sondern liefert auch Einblicke in die physiologischen und pathologischen Prozesse auf molekularer Ebene.

Das Ziel der vorliegenden Dissertation war die Entwicklung und Evaluierung der CEST-Bildgebung für die funktionelle Nierenbildgebung. Dazu wurden mehrere Nierenmetabolite untersucht, die zur Generierung eines messbaren CEST-Kontrastes an klinischen magnetic resonance (MR)-Tomographen benutzt werden können. Ein besonderer Schwerpunkt lag dabei in der Charaktisierung des chemischen Protonenaustauschs in wässrigen Lösungen von Harnstoff, dessen Konzentration im Blut einen wichtigen Marker zur Überprüfung der Nierenfunktion darstellt. Zusätzlich wurden verschiedene CEST-Akquisitonsprotokolle und Quantifizierungsmethoden unter Verwendung von simulierten und experimentellen MR-Daten evaluiert. Um die in vivo Übertragung der CEST-Bildgebung auf die menschliche Niere zu ermöglichen, wurden des Weiteren eine neue CEST-Pulssequenz und eine Nachbearbeitungs-pipeline entwickelt und anschließend in einer klinischen Kohorte von Nierentransplantatempfängern angewendet.

Im Verlauf der Arbeit wurde die Anwendbarkeit der quantitativen gepulsten CEST-Bildgebung (qCEST) an einem 3-Tesla-Ganzkörper-MR-Scanner getestet. Um die Austauschparameter zu bestimmen, wurden die AREX-Metrik und die erweiterte Ω-Plot-Methode verwendet. Die Gültigkeit und Genauigkeit dieser beiden qCEST-Ansätze in Kombination mit zwei verschiedenen CEST-Sättigungsschemata wurden dann durch Bloch-McConnell-Simulationen überprüft und mittels Messungen an Kreatin-Modellösungen an

einem 3-Tesla-MR-Gerät verifiziert. Dabei konnte gezeigt werden, dass die quantitative CEST-Analyse für die Bestimmung der Austauschraten im mittleren Austauschbereich zwischen ca. 50 und 530 Hz an einem klinischen 3-Tesla-MRT-System erfolgreich eingesetzt werden kann.

In einer anschließenden Studie wurden die Protonenaustausch-Eigenschaften von Harnstoff mittels WEX-Spektroskopie an einem Ultrahochfeld-NMR-Spektrometer mit einer Magnetfeldstärke von 14.1-Tesla charakterisiert. Darüber hinaus wurde die Machbarkeit der endogenen Harnstoff-gewichteten CEST-Bildgebung (urCEST) bei einer Feldstärke von 3-Tesla getestet. Zum Einen wurde hier der auf Harnstoff basierende urCEST-Effekt eingehend hinsichtlich seiner pH- und Konzentrationsabhängigkeit untersucht, und zum Anderen wurden die CEST-Effekte anderer endogener Nierenmetaboliten quantifiziert, um die Spezifität des urCEST-Effektes abzuschätzen. Insgesamt bestätigte die Studie, dass mithilfe der CEST-Bildgebung simultan Konzentration- und pH-gewichtete-Bilder erzeugt werden können. Sowohl die WEX- als auch die CEST-Experimente zeigten jedoch, dass der säure- und basenkatalysierte Austausch zwischen Amidprotonen von Harnstoff- und Wasserprotonen im physiologischen pH-Bereich außerordentlich langsam ist. Des Weiteren wurden mehrere wichtige Metabolite identifiziert, die einen messbaren CEST-Effekt für den physiologisch relevanten pH-Bereich aufweisen und zum gesamten in der Niere gemessenen CEST-Signal beitragen können.

In der letzten Studie wurde die CEST-Bildgebung erstmals erfolgreich bei Patienten mit einer transplantierten Niere durchgeführt. Da die Anwendung der Methode in der Niere von fettsignalinduzierten Störeinflüssen beeinträchtigt ist, wurde in dieser Arbeit eine Zweipunkt-Dixon-Technik implementiert, um Wasser- und Fettsignale zu trennen und somit eine fettfreie CEST-Bildgebung zu ermöglichen. Darüber hinaus wurde eine Multiecho-Gradienten-Echo-Sequenz mit selektiver Sättigungspulsfolge zur schnellen Detektion von präparierten CEST-Effekten an klinischen MR-Tomographen entwickelt. Unter Verwendung des optimierten CEST-Datenakquisitions- und Nachbearbeitungsprotokolls konnten kortikale und medulläre CEST-Effekte im Nierengewebe quantifiziert werden. In Übereinstimmung mit der Literatur wurde der höchste CEST-Effekt bei etwa 1 ppm Offset von der Wasserresonanz gemessen. Dies weist darauf hin, dass Harnstoff einen wesentlichen Beitrag zum gesamten CEST-Signal in der Niere leistet. Darüber hinaus konnte gezeigt werden, dass die Spezifität der endogenen Amidprotonen-gewichteten CEST-Bildgebung (APT) in der Niere durch Anwendung der Dixon-basierten CEST-Analyse verbessert werden kann.

Die vorliegende Arbeit leistet einen Beitrag zum besseren Verständnis der CEST-Effekte verschiedener Nierenmetabolite, deren Konzentration in Blut und Urin oft im Zusammenhang mit der Nierenfunktion steht. Des Weiteren kann das optimierte Verfahren zur Akquisition und Auswertung von CEST-gewichteten Daten zur nichtinvasiven metabolischen Bildgebung der menschlichen Niere verwendet werden.

Contents

Abbreviations

APT amide proton transfer

AREX apparent exchange-dependent relaxation

BM Bloch-McConnell

CEST chemical exchange saturation transfer

CW continuous wave

DC duty cycle

DWS direct water saturation

FID free induction decay

FLASH fast low angle shot

FOV field-of-view

GRE gradient echo

LS large-shift limit

MR magnetic resonance

MRI magnetic resonance imaging

MT magnetization transfer

MTC magnetization transfer contrast

NMR nuclear magnetic resonance

NOE nuclear Overhauser effect

qCEST quantitative CEST

RF radio-frequency

rNOE exchange-relayed NOE

ROI region-of-interest

SAR specific absorption rate

TE echo time

TR repetition time

urCEST urea-weighted CEST

WASSR WAter Saturation Shift Referencing

WEX water exchange

List of Figures

List of Tables

Chapter 1

Introduction

Over the past decades, MRI has become one of the most important and versatile tools in clinical diagnostics and biomedical research. While the phenomenon of NMR has been discovered independently by Bloch [1] and Purcell [2] in 1946, it was not until 1977 that the first whole-body MR image was demonstrated by Damadian [3].

During that time, NMR has evolved into a powerful spectroscopic technique to characterize atomic species and molecules. Critical to the early development of the NMR spectroscopy, was the discovery of the chemical shift by Proctor and Yu in 1950 [4]. Soon afterwards, in 1951, Arnold, Dharmatti and Packard separated signals from three groups of non-equivalent hydrogen nuclei in ethanol [5]. From these results, it became apparent that nuclei in different local chemical environments can be identified based on their slightly different resonant frequencies. In the early 1970s, Damadian reported that MR signal of a tumorous tissue substantially differs from that of a normal tissue, suggesting that the NMR technique could be used as a diagnostic tool for detecting cancer [6].

In 1973, Lauterbur proposed applying magnetic field gradients to encode the NMR signal originating from different volume elements (voxels) [7]. Furthermore, he was able to reconstruct a two-dimensional image from the NMR data of a water phantom employing the filtered back-projection algorithms, which are commonly used in computed tomography (CT). The same year, Mansfield also described the use of linear field gradients to spatially encode the resonance signals [8]. Moreover, he created a mathematical model to quickly analyze the signals for image reconstruction, which led to the invention of fast echo-planar imaging [9]. For their pioneering works, Lauterbur and Mansfield were awarded the 2003 Nobel Prize in medicine [10]. Over the past half century, MR imaging has developed rapidly and became a routine method within medical diagnostics. In addition to high-resolution anatomical images, MRI also provides information about structural properties (diffusion-weighted imaging - DWI [11, 12], MR elastography [13]), physiological function (perfusion [14], blood oxygenation level dependent imaging - BOLD [15], functional MRI [16]) and metabolism (chemical exchange saturation transfer - CEST [17, 18]) of individual organs.

CEST is a novel MRI contrast mechanism, which enables indirect detection of exchangeable protons from a variety of functional groups, such as hydroxyl, amine and amide groups, by observing changes of the bulk water signal following selective saturation of the labile protons at varying frequency offsets [19–21]. CEST imaging is advantageous for mapping low concentration (at most in the mM range) metabolites such as creatine [22–24], glucose [25–27], glutamate [28–30], glycogen [31], myo-inostol [32] and urea [33, 34], which

are not observable with the conventional MRI. Furthermore, the so-called CEST effect is sensitive to the microenvironmental properties, such as pH and temperature [35]. Therefore, CEST-based MRI is a promising research area with a great potential for clinical applications. Up to now, the utility of this method has been demonstrated for imaging tumors [36, 37], stroke [38] and intervertebral disc degeneration [39].

Numerous recent studies have also shown the potential of CEST for detecting molecular and cellular changes associated with renal and urinary diseases such as diabetic nephropathy (DN) [40], unilateral ureter obstruction (UUO) [41], kidney fibrosis [42], sepsis-induced acute kidney injury [43] and acute renal allograft rejection (AR) [44]. Because of its high sensitivity to pH changes, the CEST imaging has been proposed to measure renal pH values and induced pH alterations following an acute renal failure [45], reperfusion ischemia [46] and chronic kidney disease (CKD) [47].

Although these encouraging preclinical findings are of great importance for the fundamental understanding of molecular mechanisms underlying renal pathophysiology, their potential translation into clinical settings is limited to date. Firstly, most of the renal CEST MRI studies have been performed exclusively in animal models, which do not fully recapitulate human kidney structures and function [48]. Secondly, the CEST experiments have mostly been conducted at high magnetic field strengths and using long CEST saturation pulses. While higher magnetic field strengths are beneficial for CEST imaging, routine clinically-approved scanners operate at field strengths that usually do not surpass 3T. Besides, due to the hardware limitations and specific absorption rate (SAR) guidelines, only pulse-train pre-saturation can be utilized in clinical CEST experiments [49, 50]. Last but not least, all of the prior mentioned renal CEST imaging studies have been performed using exogenous CEST-responsive contrast agents, which may pose a risk in patients with impaired kidney function [51, 52].

The main goal of the present thesis was to evaluate of the utility of the CEST technique for imaging human kidneys. Three independent studies were conducted to evaluate the potential application of renal CEST MRI on clinical systems. Firstly, two different CEST quantification methods and saturation schemes were compared in terms of their applicability for measuring exchange-related parameters of amine protons. Secondly, comprehensive phantom experiments have been performed in order to identify kidney metabolites with exchangeable protons capable of providing CEST effect under physiological conditions. An particular focus was put on examining urea, which is the most abundant nonaqueous constituent of urine and an important marker of renal function. To better understand the saturation transfer effects observed in the human kidney in vivo, proton exchange properties were thoroughly characterized by water exchange (WEX) ^{1}H-NMR spectroscopy [53] at ultra-high magnetic field strength of 14.1T, and validated using quantitative CEST analysis at 3T. Thirdly, an optimized CEST acquisition protocol and post-processing pipeline tailored to renal graft applications were developed and applied in renal transplant recipients.

Chapter 2

Basic theory

2.1 Principles of NMR

The phenomenon of nuclear magnetic resonance (NMR) is based on the concept of nuclear spin, which can be quantitatively described only in terms of quantum mechanics. On the other hand, to visualize the effects of radio-frequency (RF) pulses on macroscopic magnetization vectors the classical viewpoint is more convenient. This section is intended to provide both the quantum mechanical and classical description of the dynamics of a nuclear spin exposed to static and time-varying magnetic fields. A more detailed and thorough coverage of the NMR principles can be found in [54–57].

2.1.1 Nuclear spin in a magnetic field

A magnetic system, such as an atomic nucleus, possess angular momentum $\vec{J}$, which is always associated with the magnetic dipole moment $\vec{\mu}$. In the quantum theory, any physical quantity corresponds to a quantum mechanical operator. The operator of the nuclear magnetic moment $\hat{\vec{\mu}}$ is often expressed in terms of the gyromagnetic ratio γ for a nucleus:

$$\hat{\vec{\mu}} = \gamma \hat{\vec{J}} = \gamma \hbar \hat{\vec{I}} \tag{2.1}$$

where $\hbar$ is the Planck's constant divided by 2π ($\hbar = 1.055{\cdot}10^{-34}$ J·s).

Since the angular momentum $\vec{J}$ of an isolated system is a conserved quantity, any component of the dimensionless momentum operator $\hat{\vec{I}}$ (for example $\hat{I}_z$) and the square of the momentum $\hat{\vec{I}}^2$ form a pair of mutually commuting operators and have, therefore, common eigenfunctions. In Dirac notation, $\mid I, m\rangle$ describes the eigenvectors of the spin system with well-defined eigenvalues:

$$\hat{\vec{I}}^2 \mid I, m\rangle = I(I+1) \mid I, m\rangle \tag{2.2}$$

$$\hat{I}_z \mid I, m\rangle = m \mid I, m\rangle \tag{2.3}$$

where I is an integer or a half-integer and represents the spin quantum number (or more simply the spin). For protons, neutrons, electrons and nuclei with an odd mass number, the spin number equals $\frac{1}{2}$. The magnetic quantum number, m have $2I+1$ values and goes from $-I$ to $+I$ by steps of 1.

The magnetic moment $\vec{\mu}$ in an external magnetic field along the z-direction $\vec{B} = (0, 0, B_0)$ has an associated magnetic energy, defined by a simple Hamiltonian $\hat{\mathcal{H}}_z$:

$$\hat{\mathcal{H}}_z = -\hbar \hat{I}_z \gamma B_0 \tag{2.4}$$

To find the allowed energy levels of the quantum mechanical system, the time-independent Schrödinger equation is solved:

$$\hat{\mathcal{H}} \mid I, m\rangle = E_m \mid I, m\rangle \tag{2.5}$$

The eigenvalues of the Hamiltonian $\hat{\mathcal{H}}_z$ are simply multiples ($\hbar\gamma B_0$) of the eigenvalues of $\hat{I}_z$, thus:

$$E_m = -\hbar\gamma B_0 m \tag{2.6}$$

The energy levels E_m split into $2I+1$ equidistant terms (the so-called Zeeman components). A proton, and other nuclei with $I = \frac{1}{2}$ have just two possible energy levels with the α-spin state: $\mid \frac{1}{2}, -\frac{1}{2}\rangle = \mid \alpha\rangle$ and the β-spin state: $\mid \frac{1}{2}, +\frac{1}{2}\rangle = \mid \beta\rangle$, which are separated by:

$$\Delta E = E_{m-1} - E_m = \hbar\gamma B_0 \tag{2.7}$$

The spins in the lower energy level (β-spin state) are oriented parallel to B_0 (the most stable configuration), while the magnetic moments in the higher energy level (α-spin state) have an anti-parallel alignment (less stable configuration) with B_0. Figure 2.1 illustrates the Zeeman splitting of the spin states for an $I = \frac{1}{2}$ system.

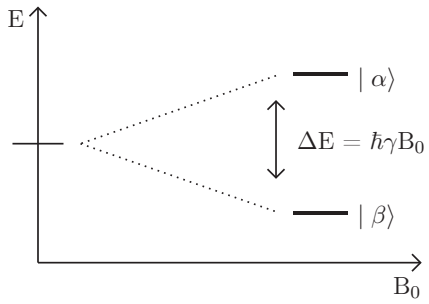

Figure 2.1: Zeeman splitting of the spin states for an $I = \frac{1}{2}$ system placed in an external static magnetic field B_0. The energy transition between two possible energy levels is defined by the energy difference ΔE, which is directly proportional to the applied magnetic field strength.

If a spin system is subjected to an additional alternating magnetic field with a frequency close to $\upsilon_0 = \Delta E/\hbar$, transitions between the energy levels will be induced. This phenomenon is known as magnetic resonance and forms the basis for all NMR experiments. The so-called Larmor precession frequency υ_0 depends on the field strength B_0 and the gyromagnetic ratio γ, which is unique for each specific nucleus and particle. For the proton in a magnetic field of $B_0 = 3$T, $\upsilon_0 = 127.729$ MHz.

2.1.2 Macroscopic magnetization

Until now, the behavior of an elementary system involving individual nuclear spins has been considered. However, a macroscopic sample includes a great number of interacting spins and the statistical treatment has to be applied in order to describe the whole set of systems distributed randomly within the measured sample. According to the Boltzmann distribution of nuclei at energy levels, the number n_m of nuclei at the level with the quantuum number m can be expressed as:

$$n_m = N\frac{exp[-E_m/(k_BT)]}{\sum_{m=-I}^{I} exp[-E_m/k_BT]} = N\frac{exp[\hbar\gamma B_0 m/(k_BT)]}{\sum_{m=-I}^{I} exp[\hbar\gamma B_0 m/(k_BT)]} \tag{2.8}$$

where N is the total number of nuclei per unit volume of the sample, E_m is the energy of the level m, and k_B denotes the Boltzmann constant. For typical values of B_0 and T (high temperature approximation), the exponential can be represented by the first two terms of its Taylor series:

$$n_m = N\frac{1+\hbar\gamma B_0 m/(k_BT)}{\sum_{m=-I}^{I} 1+\hbar\gamma B_0 m/(k_BT)} \approx \frac{N}{2I+1}\Big(1+\frac{\hbar\gamma B_0 m}{k_BT}\Big) \tag{2.9}$$

In the simple case of a macroscopic ensemble of nuclear spin I =1/2, the populations n_α^0 and n_β^0 match the energy levels m = -1/2 and m = +1/2 and are given by:

$$n_\alpha^0 = \frac{N}{2}(1-\frac{\hbar\gamma B_0}{2k_BT}) \tag{2.10}$$

$$n_\beta^0 = \frac{N}{2}(1+\frac{\hbar\gamma B_0}{2k_BT}) \tag{2.11}$$

Thus, the static equilibrium difference in level populations can be obtained from:

$$\Delta n = n_\beta^0 - n_\alpha^0 = \frac{N\hbar\gamma B_0}{2k_BT} \tag{2.12}$$

In a magnetic field of B_0 = 1T at room temperature T = 25°C, the difference in spin populations is very small, in the range of 3×10^{-6}. The net magnetic moment, $\vec{M}$, of a macroscopic system is the total average magnetic moment of nuclei per unit volume. The population difference results in a net component of $\vec{M}$ parallel to B_0. At thermal equilibrium, the longitudinal magnetization, $\vec{M}_0$ is equal to:

$$\vec{M}_0 = \sum_{i=1}^{N} \langle\hat{\mu}_z\rangle_i = \frac{\hbar}{2}\gamma\Delta n \tag{2.13}$$

Using equations (2.12) and (2.13), the macroscopic magnetization vector, $\vec{M}_0$ can be expressed as follows:

$$\vec{M}_0 = (\gamma\hbar)^2(\frac{NB_0}{4k_BT}) = \mathcal{X}_0 \cdot B_0 \tag{2.14}$$

where $n = n_\alpha + n_\beta$ is the total number of nuclear spins per unit volume. Equation 2.14 is an expression of the Curie law, according to which the paramagnetic susceptibility of magnetic microparticles, $\mathcal{X}_0$, is inversely proportional to the absolute temperature T and independent of the applied field B_0.

2.1.3 Bloch equations and relaxation

For a particle in a time-varying magnetic field, the time-dependent Schrödinger equation takes the form:

$$i\hbar\frac{\partial}{\partial t}|I,m\rangle = \hat{\mathcal{H}}_z(t)|I,m\rangle \tag{2.15}$$

where $\hat{\mathcal{H}}(t) = -\vec{\hat{\mu}}\cdot\vec{B}(t)$ is the time-dependent Hamilton operator. Since all experimental systems consist of a whole ensemble of N individual spins, only the expectation value of the magnetic moment $\langle\vec{\hat{\mu}}\rangle$ in a volume V is assessable. The behavior of the macroscopic magnetization $\vec{M} = \frac{N}{V}\langle\vec{\mu}\rangle$ in the presence of an arbitrary field $\vec{B}(t)$ can be expressed as follows:

$$\frac{d\vec{M}}{dt} = \vec{M}\times\gamma\vec{B}(t) \tag{2.16}$$

Assuming an external $\vec{B_0} = (0,0,B_0)^T$ magnetic field and a resonant irradiation of a $\vec{B_1}(t)$ radio-frequency field, acting perpendicular to the static field, the resultant $\vec{B}(t)$ vector can be written as:

$$\vec{B}(t) = \vec{B_0} + \vec{B_1}(t) = \begin{pmatrix} 0 \\ 0 \\ B_0 \end{pmatrix} + B_1\begin{pmatrix} cos(\omega_{RF}t) \\ sin(\omega_{RF}t) \\ 0 \end{pmatrix} \tag{2.17}$$

where B_1 is the amplitude and ω_{RF} the angular frequency of the RF field. After the transformation in the reference frame $(x', y', z' = z)$ rotating with the angular frequency ω_{RF}, the equation of motion simplifies to:

$$\frac{d\vec{M'}}{dt} = \vec{M'}\times\gamma\begin{pmatrix} B_1 \\ 0 \\ B_0 - \frac{\omega_{RF}}{\gamma} \end{pmatrix} = \vec{M'}\times\gamma\vec{B}_{eff} \tag{2.18}$$

In the case of a resonant RF irradiation with $\omega_{RF} = \omega_0 = \gamma B_0$, the effective field collapses to $\vec{B}_{eff} = (B_1, 0, 0)^T$. As a result, the external magnetic field affects solely the magnetization $\vec{M}$ in x'-direction that undergoes precession in the y'-z-plane at the frequency ω_1. The final flip angle α of the magnetization with respect to the direction of the main magnetic flux density field for a given amplitude B_1 and duration t_{pd} of the applied RF pulse is defined as:

$$\alpha = \int_0^{t_{pd}}\omega_1(\tau)\mathrm{d}\tau = \int_0^{t_{pd}}\gamma B_1(\tau)\mathrm{d}\tau \tag{2.19}$$

In an NMR experiment, after switching off the RF field, the spin system strives to achieve the thermal equilibrium. In a classical approach, the time development of the macroscopic magnetization is described by the Bloch equations [1]:

$$\begin{aligned} \frac{dM_x}{dt} &= \gamma(\vec{M}\times\vec{B})_x - \frac{M_x}{T_2} \\ \frac{dM_y}{dt} &= \gamma(\vec{M}\times\vec{B})_y - \frac{M_y}{T_2} \\ \frac{dM_z}{dt} &= \gamma(\vec{M}\times\vec{B})_z - \frac{M_z - M_0}{T_1} \end{aligned} \tag{2.20}$$

with the Cartesian components of the magnetization M_i (where $i = x, y, z$) and the equilibrium magnetization M_0. The time constants T_1 and T_2 account for the longitudinal and transversal relaxation, respectively.

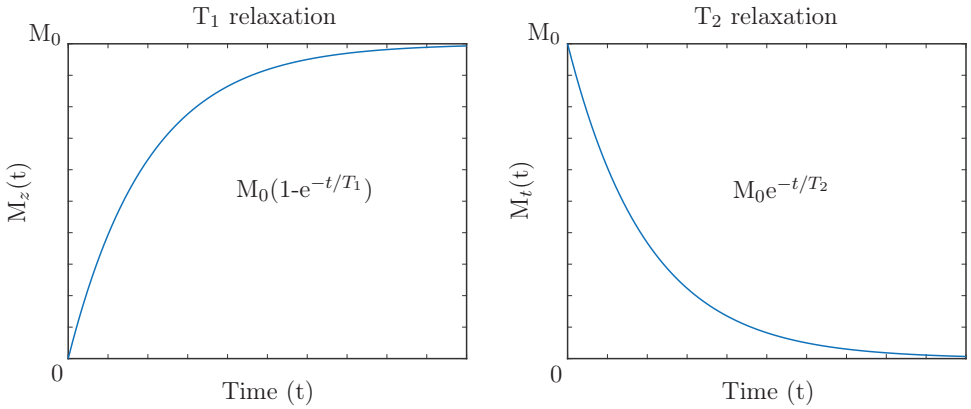

Figure 2.2: Longitudinal (T_1) and transversal (T_2) relaxation of nuclear magnetization after an exciting 90° RF pulse. T_1 describes the exponential recovery of the longitudinal magnetization M_z, whereas T_2 refers to the exponential decay of the transverse magnetization M_t.

The relaxation time T_1 is the time required for the z-component of the magnetization M_z to recover approximately 63% of its initial value after the excitation pulse has been applied. The longitudinal relaxation involves thermal interactions between excited hydrogen nuclei (spins) and neighboring molecules (lattice) within the sample. The relaxation time T_2 is defined as the time required for the transverse magnetization M_t to decay down to about 37% of its initial maximum value. Directly after the exciting 90° RF pulse, the nuclear spins are aligned in one direction (phase coherent). However, direct interactions between the spins (without energy transfer to lattice) lead to spin dephasing and phase coherence lost, which in turn causes the reduction of the transverse component of the magnetization M_t. Figure 2.2 depicts the T_1 and T_2 relaxation of nuclear magnetization after an exciting 90° RF pulse.

2.1.4 MR signal formation

The transverse component of the precessing magnetization $M_t(t)$ generates a periodically oscillating voltage in the receiver RF coils based on the Faraday-Lenz Law of electromagnetism:

$$M_t(t) = M_x(t) + iM_y(t) = |M_t(t)|e^{i\theta} \tag{2.21}$$

This exponentially decaying signal is known as free induction decay (FID) and is presented in figure 2.3. For detection of the real and imaginary components of the complex signal, a demodulation technique called quadrature detection is generally used. This signal processing method uses two detector channels sensitive to magnetic flux in two orthogonal directions, and thus the direction of rotation (clockwise or counterclockwise) in the rotating frame can be distinguished. In any real NMR experiment, the signal decay of the

FID due to the spin-spin interactions is enhanced by the local field inhomogeneities ΔB_0, susceptibility differences within the sample, chemical shift, eddy currents, imperfect coil geometry and other processes. To account for these effects, a characteristic rate T_2^* is introduced:

$$\frac{1}{T_2^*} = \frac{1}{T_2} + \gamma|\Delta B_0| \tag{2.22}$$

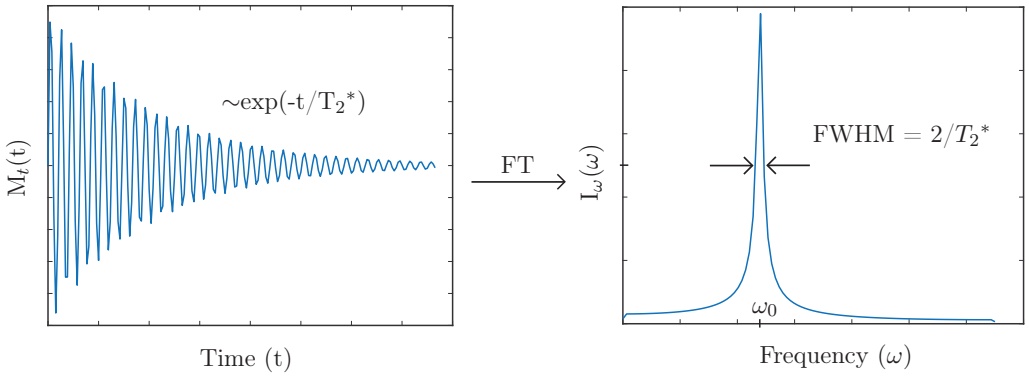

Figure 2.3: Exponential decay of the NMR signal due to T_2^* relaxation. The Fourier transform (FT) of the FID (left) yields a Lorentzian lineshape at the frequency offset ω_0 (right).

Table 2.1 contains values for longitudinal and transversal relaxation times measured for different human tissues at a magnetic field strength of 3T.

Table 2.1: T_1 and T_2 relaxation times for various human tissues at 3T [58].

Tissue	T_1 [ms]	T_2 [ms]
Kidney	1194 ± 27	56 ± 4
Liver	812 ± 64	42 ± 3
Skeletal muscle	1412 ± 13	50 ± 4
White matter	1084 ± 45	69 ± 3
Gray matter	1820 ± 114	99 ± 7
Blood	1932 ± 85	275 ± 5

2.1.5 Chemical shift

Most nuclei are embedded in orbitals with electrons around them. The applied magnetic field B_0 induces circulations of the electrons surrounding the nucleus, which in turn generate a weak induced magnetic field $\vec{B}_{ind}$. According to Lenz's law, the induced field is proportional to the static magnetic field $\vec{B}_0$ but is opposite in direction. The local magnetic field experienced by a nucleus is the sum of the external magnetic field and the induced field:

$$\vec{B}_{loc} = \vec{B}_0 + \vec{B}_{ind} = \vec{B}_0(1 - \sigma) \tag{2.23}$$

where σ is the shielding factor. In general, higher electron density causes more shielding and results in a lower Larmor frequency. The resonant frequency ω of the nucleus relative to a reference substance at a given magnetic field is known as chemical shift δ_i, and is defined as:

$$\delta_i[ppm] = \frac{\omega - \omega_{ref}}{\omega_{ref}} \tag{2.24}$$

where ω_{ref} is the resonance frequency of the reference nucleus. In high-resolution NMR, tetramethylsilane (TMS) is usually used as a standard reference compound. Chemical shift δ is reported in dimensionless unit of parts per million (ppm). Conventionally, TMS is assigned a value of 0 ppm.

2.2 Magnetic resonance imaging (MRI)

Magnetic resonance imaging is a noninvasive imaging technique to produce cross-sectional images of the body in any arbitrary orientation. The theoretical description of the MRI principles in this dissertation is based on [59, 60].

2.2.1 Spatial encoding

Spatial encoding over the sample is accomplished by the superposition of linearly-varying magnetic fields, $\vec{G}(t)$ to the stationary and spatially independent B_0 field:

$$\vec{G}(t) = \begin{pmatrix} G_x \\ G_y \\ G_z \end{pmatrix} = \begin{pmatrix} \frac{\partial B}{\partial x} \\ \frac{\partial B}{\partial y} \\ \frac{\partial B}{\partial z} \end{pmatrix} \tag{2.25}$$

with the cartesian components of the gradient field $G_i(t)$ (where $i = x, y, z$). Thus, the resonance frequency $\omega(r)$ becomes position- and time-dependent:

$$\omega(\vec{r}, t) = \gamma(B_0 + \underbrace{\vec{G}(t) \cdot \vec{r}}_{\Delta\omega}) \tag{2.26}$$

where $\vec{r} = (x, y, z)^T$ is a vector describing the spatial position. The magnetic field produced by the gradient system changes the Larmor frequency by $\Delta\omega$, and therefore causes a phase shift $\Delta\phi$:

$$\Delta\phi = \int_0^t -\Delta\omega(\vec{r}, t)\mathrm{d}\tau = \int_0^t -\gamma\vec{G}(\tau) \cdot \vec{r}\mathrm{d}\tau = -\vec{k}(t) \cdot \vec{r} \tag{2.27}$$

where $\vec{k}(t)$ is the wave vector in the reciprocal space, defined as:

$$\vec{k}(t) = \gamma \begin{pmatrix} \int_0^{t_x} G_x(\tau)\mathrm{d}\tau \\ \int_0^{t_y} G_y(\tau)\mathrm{d}\tau \\ \int_0^{t_z} G_z(\tau)\mathrm{d}\tau \end{pmatrix} \tag{2.28}$$

$\vec{k}$ is the conjugate variable for $\vec{r}$. After a RF pulse, the transverse magnetization $M_t(\vec{r},t)$ is manipulated by the spatial encoding gradient $\vec{G}(t)$, which in turn determines the reciprocal space vector $\vec{k}$. The phase shift $\Delta\phi$ can be included in the equation for the complex signal of the precessing magnetization:

$$M_t(\vec{r},t) = M_t(\vec{r})e^{i\Delta\phi(\vec{r},t)} = M_t(\vec{r})e^{-i\vec{k}(t)\cdot\vec{r}} \tag{2.29}$$

A wide variety of MRI pulse sequences can be created by combining slice selection, frequency encoding and phase encoding, which are introduced briefly in the following.

2.2.2 Slice selection

To isolate a single plane in a three-dimensional object being imaged, only spins within the slice of interest should be excited. By applying a gradient field $\vec{G} = (0,\, 0,\, G_z)^T$ the Larmor frequency becomes position-dependent:

$$\omega_0(z,t) = \gamma(B_0 + G_z \cdot z) \tag{2.30}$$

When a frequency-selective RF pulse is applied simultaneously with the magnetic field gradient, only a selective range of frequencies, and hence spatial positions, is excited. The thickness of the selected slice is determined by the spectral width of the excitation pulse and by the strength of the corresponding gradient field. A thinner spatial slice is usually achieved by decreasing the RF pulse bandwidth while keeping the gradient field strength constant. Similarly, the spatial position of the slice, in which the resonance condition is met, is also affected by two factors, the magnetic field strength and the transmitter frequency of the RF pulse. To excite spins that are not located exactly in the magnet's isocenter, the transmitter frequency should be adjusted according to equation 2.30.

2.2.3 Frequency and phase encoding

Since the spins outside the slice of interest are not affected by the excitation pulse, a transverse magnetization, and hence the MR signal, is only generated within the selected plane. For the position distinction within the excited volume, spatial encoding is used. To determine the position in the transverse plane, linear field gradients G_x and G_y are applied along the x and y-axis, respectively.

Generally, the function of the first gradient, G_y, is to introduce a phase-shift in the FID-signal dependent on the position along the y-axis, given by:

$$\phi(y,t) = \gamma y \int_0^{t_y} G_y(\tau)\mathrm{d}\tau \tag{2.31}$$

which simplifies for a constant amplitude gradient, $\vec{G_y}(t) = \vec{G_y}$ to:

$$\phi(y,t) = \gamma y t_y G_y(\tau) \tag{2.32}$$

When the G_y gradient is removed, the transverse magnetization at each position on the y-axis is prepared with a specific phase-shift $\phi(y,t)$. Then, the second gradient, G_x is played out and the precession frequency of the spins becomes a function of the position in the x-direction. Since the data acquisition is performed during the frequency encoding (readout), the spatially dependent frequencies are recorded.

2.2.4 MR image reconstruction

The resulting MR signal is composed of the individual signals measured by the receiver coils and is given by the integral over location $\vec{r}$:

$$S(\vec{k}(t),t) \propto \int_V M_t(\vec{r},t)\mathrm{d}\vec{r} = \int_V \varrho_0(\vec{r})e^{-i\vec{k}(t)\cdot\vec{r}}\mathrm{d}\vec{r} \tag{2.33}$$

with the position-dependent spin density $\varrho_0(\vec{r})$. The contribution of each frequency component to the MR signal can be easily determined by fast discrete Fourier transformation of the measured signal.

$$\varrho_0(\vec{r}) = \mathcal{F}\{S(\vec{k}(t))\} = \frac{1}{(2\pi)^3}\int_V S(\vec{k}(t))e^{i\vec{k}(t)\cdot\vec{r}}\mathrm{d}\vec{k} \tag{2.34}$$

2.3 Gradient echo imaging (GRE)

The gradient echo imaging uses a magnetic field gradient during the FID to produce a spatially encoded echo event. A pulse sequence diagram for the fast low angle shot (FLASH) gradient-echo MRI sequence is displayed in Figure 2.4 [61].

The FLASH technique utilizes a low flip-angle RF excitation pulse, which leaves a significant longitudinal magnetization for an immediate excitation and gradient echo data collection with a short repetition time (TR). Each repetition of the basic pulse sequence acquires one k-space line along the phase encoding direction. To minimize the interferences with the next k-space line measurement, the residual transverse magnetization is dephased in the xy-plane using spoiling gradients, which is an artificial equivalent to the natural dephasing due to B_0 inhomogeneity. In order to collect the data for an N×N image, N repeats must be acquired.

2.4 Lipids in MRI

Lipids are a large and diverse class of naturally occurring molecules that are related by their high solubility in non-polar organic solvents and low solubility in water [62]. The term fat describes a subgroup of lipids called triglycerides, which are the main constituents of body fat stored in the adipose tissue.

Protons in lipids and water experience different local magnetic fields as a result of the different field-shielding contribution of the electron clouds. Highly electronegative oxygen

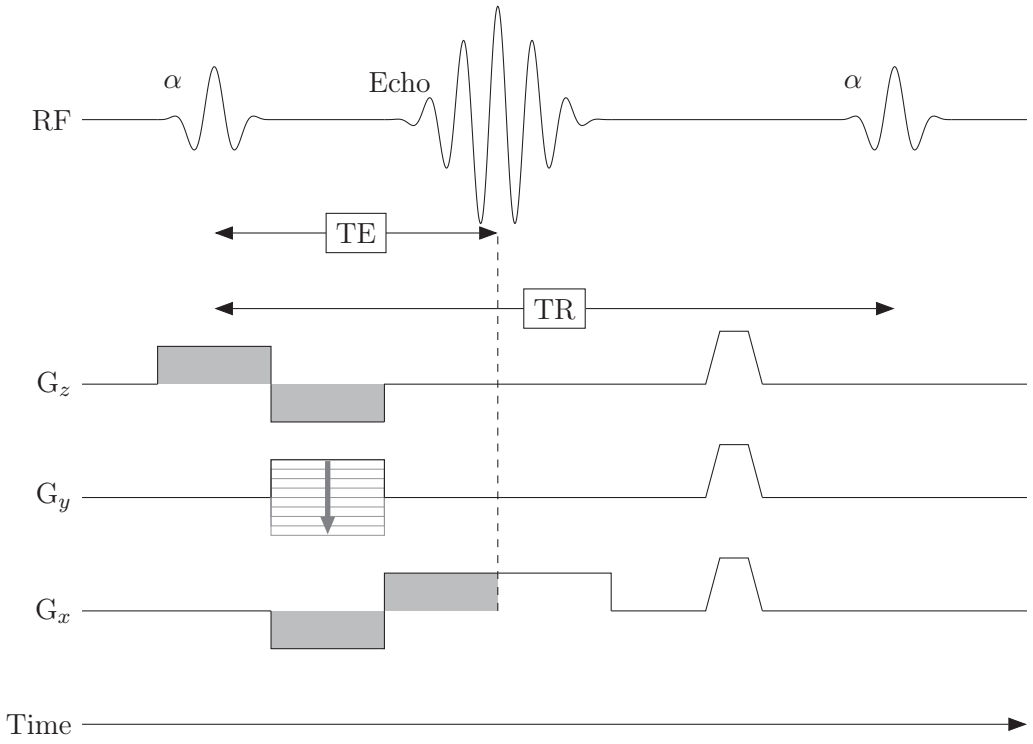

Figure 2.4: Pulse sequence diagram of a FLASH gradient echo sequence. The combination of a low flip angle (α) RF excitation and acquisition of a gradient echo at short echo time (TE) allows to obtain short repetition time (TR), thus enabling rapid imaging. The spatial information is encoded by the G_z, G_y, and G_x gradients (slice selection, phase encoding and readout gradients, respectively).

atom pulls the electron clouds away from the hydrogen protons in water more strongly than the relatively electroneutral carbon atoms in fats. As a consequence, the protons in fat are more shielded from the static magnetic field than those in water, and therefore precess at lower frequencies than the water protons. The absolute chemical shift is 3.5 ppm.

Because of this difference in the resonant frequency, the fat and water signals within the same voxel are mapped to slightly different spatial locations along the the frequency-encoding dimension. This effect, known as the chemical shift artifact of the first kind, is especially noticable at fat-soft tissues boundaries, such as the kidney and perinephric fat. Furthermore, the constructive and destructive interferences of the water and fat signals based on their phase difference cause a cyclic variation in measured MR signal intensity. This so-called chemical shift artifact of the second kind occurs exclusively in gradient echo sequences. Images acquired when the transverse magnetization vectors for the fat (F) and water (W) protons are parallel aligned are referred to as in-phase images ($S_{IP} = W + F$), whereas those obtained in the case of an anti-parallel alignment are referred to as out-of-phase images ($S_{OP} = W - F$). In-phase and out-of-phase images, as presented in figure 2.5, can be selected by choosing an appropriate TE. The TE-dependent phase relation is exploited in Dixon-based fat suppression approaches, which are widely used in

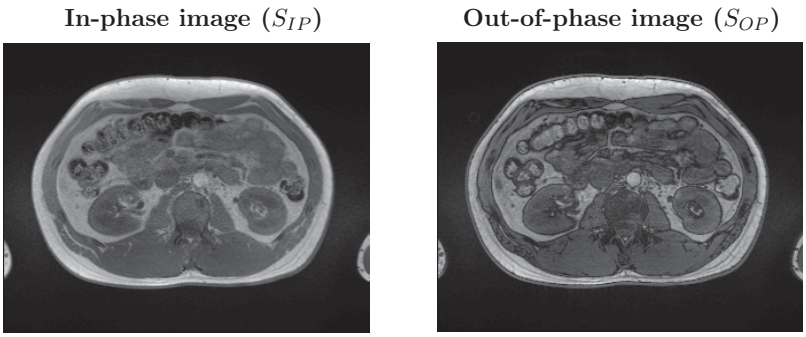

Figure 2.5: Chemical shift MR imaging in the abdomen. At an in phase (IP) TE, water and fat transverse magnetization vectors point in the same direction, and therefore the collected MR signal is a sum of the water and fat signals (left). At an out-of-phase (OP) TE, the water and fat transverse magnetizations are aligned in the opposite direction, and thus the net magnetization is the absolute value of difference between the signal intensities from water and fat protons (right).

most abdominal protocols nowadays [63]. The basic Dixon method relies on acquiring a pair of GRE images at the same TR but with two different TE, one in-phase and the second out-of-phase. The water-only, and the fat-only images can then be obtained as follows:

$$F = \frac{1}{2} \cdot (S_{IP} - S_{OP}) \tag{2.35}$$

$$W = \frac{1}{2} \cdot (S_{IP} + S_{OP}) \tag{2.36}$$

Chapter 3

Magnetization transfer and CEST

3.1 Magnetization transfer processes

So far, a single spin system, whose dynamics is characterized by the Bloch equations, has been assumed. If several different spin systems are considered, interactions occurring between spins in different magnetic environments have to be taken into account. These interactions can be either via the direct exchange of protons or water molecules between different locations in space or between molecules, or through-space dipolar coupling between the hydrogen nuclei [64]. As a result of the chemical and dipolar exchange, magnetization is transferred from one spin population to another. The spin system with the same physical properties, such as chemical shift, exchange rate and relaxation parameters, is described as a pool. The schematic structure of a simple two-pool model is presented in figure 3.1.

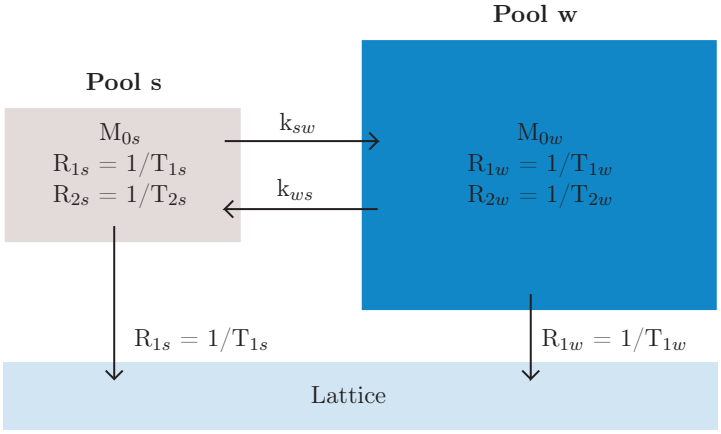

Figure 3.1: A kinetic two-pool model of a large bulk water pool (pool w) and a less abundant solute pool (pool s) with forward exchange rate k_{sw}. The pools are defined by their thermal equilibrium magnetizations M_{0i}, and relaxation rates R_{1i} and R_{2i} (where $i = w, s$). The ratio of the magnetizations, M_{0s}/M_{0w}, is conserved by the the backward exchange rate k_{ws}.)

In the CEST experiment, large bulk water pool (pool w) and a less abundant solute pool (pool s) are considered. In aqueous solutions, the chemical and physical interactions between the two pools are governed by two different mechanisms described briefly in the following sections.

3.1.1 Dipolar interactions

In a two-spin system formed by neighboring protons, spin exchange can occur via through-space cross-relaxation owing to the existence of a dipolar-coupling between the two pools. A phenomenon that arises from the dipole relaxation is termed the nuclear Overhauser effect (NOE), and represents the change of magnetization of a particular proton due to the perturbation of magnetization of an another proton nearby in space. The strength of the NOE depends on the distance between two nuclei, their gyromagnetic ratio and relative orientations [65].

Besides the homo-nuclear NOE between protons (^{1}H-^{1}H NOE), the magnetization transfer between different nuclei (hetero-nuclear NOE: ^{1}H-^{31}P, ^{1}H-^{13}C) can be observed in NMR experiments. Moreover, the dipolar coupling can occur within a molecule (intramolecular) and between different molecules (intermolecular) [64].

3.1.2 Chemical exchange

In general, hydrogen proton exchange between functional groups in metabolites, proteins, peptides etc. and water is both acid- and base-catalyzed and therefore strongly pH-dependent [66, 67]:

$$k_{sw} = k_b \cdot 10^{pH-pK_w} + k_a \cdot 10^{-pH} + k_0 \tag{3.1}$$

where k_a, k_b and k_0 (in Hz l/mol) are rate constants for the acid-, base- and water-catalyzed protolysis, respectively. The rate of the spontaneous reaction k_0 is very slow compared to the acid and based catalysis, and thus often assumed negligible [67]. The pK_w refers to a logarithm of the ionization constant, which is temperature dependent and given by the solution of the van't Hoff equation [68, 69]:

$$pK_w(T) = pK_w(T_0) - \frac{\Delta H^0_R}{R \cdot ln10}\Big(\frac{1}{T_0} - \frac{1}{T}\Big) \tag{3.2}$$

$pK_w(T_0)$ refers here to the logarithm of the water-ion product at temperature $T_0 = 25°$C, $\Delta H^0_R = 55.84$ kJ/mol is the standard reaction enthalpy for the self-dissociation of water and $R = 8.314$ J/(mol·K) is the gas constant [68, 69].

The effect of temperature on the exchange rate constant $k(T)$ is given by the Arrhenius equation, which can be used to determine the activation energy E_A for a reaction [70, 71]:

$$k(T) = A(T)e^{-E_A/RT} \tag{3.3}$$

where A(T) is a pre-exponential factor, called frequency factor or Arrhenius constant. Employing equations 3.2 and 3.3 with A = k(298.5 K) at $T_0 = 25°$C = 298.15 K, the dependence of the exchange rate constant k_{sw} on pH and T can be expressed as follows:

$$\begin{aligned} k_{sw} = {} & k_b(298.15K) \cdot [mol/l] \cdot 10^{pH-14+\frac{E_{A,b}+\Delta H^0_R}{Rln10}\left(\frac{1}{298.15K}-\frac{1}{T}\right)} \\ & + k_s(298.15K) \cdot [mol/l] \cdot 10^{-pH+\frac{E_{A,s}}{Rln10}\left(\frac{1}{298.15K}-\frac{1}{T}\right)} \end{aligned} \tag{3.4}$$

3.1.3 Bloch-McConnell equations (BM)

Chemical exchange processes are governed by the Bloch-McConnell equations, which can be easily derived from the Bloch equations by adding a term that account for a constant exchange rate of spins between different pools [72–74]:

$$\begin{aligned}
\frac{dM_{xw}}{dt} &= -\Delta\omega_w M_{yw} - R_{2w}M_{xw} + k_{sw}M_{xs} - k_{ws}M_{xw} \\
\frac{dM_{yw}}{dt} &= +\Delta\omega_w M_{yw} - R_{2w}M_{yw} - \omega_1 M_{zw} + k_{sw}M_{ys} - k_{ws}M_{yw} \\
\frac{dM_{zw}}{dt} &= -\omega_1 M_{yw} - R_{1w}(M_{zw} - M_{0w}) + k_{sw}M_{zs} - k_{ws}M_{zw} \\
\frac{dM_{xs}}{dt} &= -\Delta\omega_s M_{ys} - R_{2w}M_{xs} - k_{sw}M_{xs} + k_{ws}M_{xw} \\
\frac{dM_{ys}}{dt} &= +\Delta\omega_s M_{ys} - R_{2w}M_{ys} - \omega_1 M_{zs} - k_{sw}M_{ys} + k_{ws}M_{yw} \\
\frac{dM_{zs}}{dt} &= -\omega_1 M_{ys} - R_{1s}(M_{zs} - M_{0,s}) + k_{sw}M_{zs} + k_{ws}M_{zw}
\end{aligned} \tag{3.5}$$

The BM equations describe the dynamics of magnetization in a two-pool chemical exchange model, consisting of a small pool of water-exchangeable solute protons (pool s) and a much larger pool of bulk water protons (pool w), during RF irradiation with the amplitude $B_1 = \omega_1/\gamma$. The shift between the Larmor frequency δ_i of the pool i, and the RF irradiation frequency $\Delta\omega$, is $\Delta\omega_i = \Delta\omega$ - δ_i. The R_{1i} and R_{2i} are the spin-lattice, and spin-spin relaxation rates, respectively. M_{0i} represents the thermal equilibrium magnetizations in a static magnetic field $\vec{B}$. k_{sw} and k_{ws} denote the exchange rate of protons from pool s to pool w ($s \rightarrow w$) and vice versa ($w \rightarrow s$). In equilibrium, the system obeys the following relationship:

$$k_{sw}M_{0s} = k_{ws}M_{0w} \tag{3.6}$$

The ratio of the equilibrium magnetizations $M_{0s}/M_{0w} = f_s$ describes the relative concentration, also known as labile proton ration or fractional concentration.

It is usually difficult to solve the BM equations analytically, even for the simple case of two site exchange. One interesting solution based on the eigenspace approach [75, 76] is presented in the section 3.2.3.

3.2 Chemical exchange saturation transfer (CEST)

The macroscopic magnetization of the spin pool can be manipulated either through RF excitation, as described in the section 2.1.3, or by selective RF saturation, i.e. equalization of the spin populations between two energy levels. Under a long RF irradiation pulse, the protons in the β-spin state absorb the energy, while the protons in the α-spin state are stimulated to give up their energy. If the energy absorbed is sufficient to equilibrate the spin populations, a condition known as saturation occurs and no further absorption will take place. Since there is no residual longitudinal magnetization, only negligible signal will be produced after subsequent excitation of the saturated spin pool [64].

The saturation can be transferred if the protons in the macromolecules or small metabolites (pool s) exchange physically with the water protons (pool w), and vice versa. As a result, the water pool becomes partially saturated and the spin polarization of the water pool is reduced. This chemical exchange saturation transfer (CEST) effect leads to a reduction in water signal, which can be measured using an MRI sequence. Figure 3.2 illustrates the basic principles of CEST.

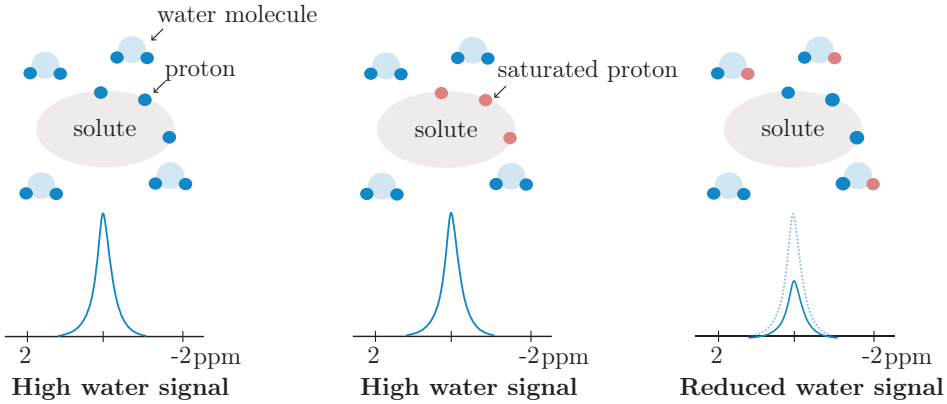

Figure 3.2: Illustration of the CEST principles. Small molecules with exchangeable protons (solute) are surrounded by water molecules. Saturation pulse on solute's proton frequency nulls the MR signal of these protons. Because the saturated protons in the solute pool continually exchange with the unsaturated water pool, the measured water signal becomes lower. Adapted from [77].

3.2.1 Basic CEST experiment

In a basic saturation transfer experiment, the exchanging proton pool is saturated using a long irradiation module with a duration t_{sat} and an amplitude B_1 tuned to a frequency with offset $\Delta\omega$ from the water resonance. Since the continuous wave (CW) irradiation is usually not feasible on clinical scanners due to the hardware and specific absorption (SAR) limitations, the saturation pulse train with N selective pulses of width t_{pd}, separated by delays t_{ipd} must be used instead. Immediately after the saturation period, fast image readout sequence such as a fast spin echo (FSE), a fast low-angle shot (FLASH) or an echo planar imaging (EPI) is performed [78].

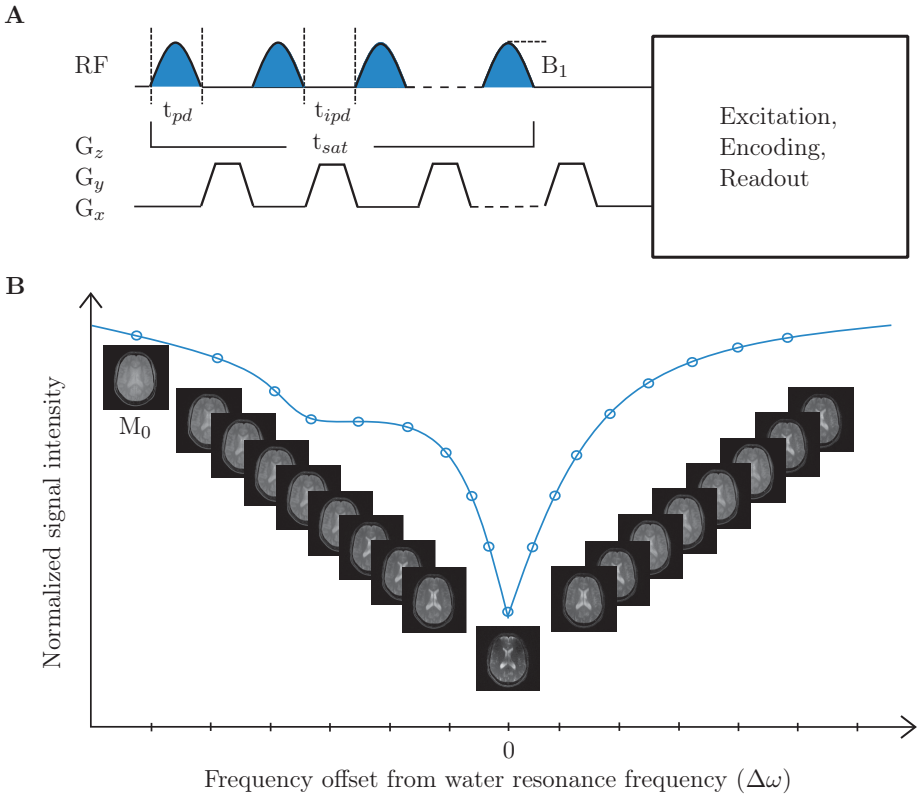

Figure 3.3: A saturation transfer MRI sequence for collecting CEST-weighted image data. A magnetization preparation for CEST imaging is achieved by applying a RF saturation pulse (train) characterized by pulse duration t_{pd} interpulse delay t_{ipd}, and irradiation power B_1. After saturation at a frequency offset $\Delta\omega$, the prepared magnetization is measured using a fast readout sequence (top). Repeating this procedure at different spectral offsets leads to an image for each frequency offset (bottom). Adapted from reference [78].

To measure the prepared CEST effects, the sequence depicted in figure 3.3 is repeated at varying frequency offsets within a specific range. Further, the water signal intensity during saturation (M_{zw}) is normalized to the signal intensity without any saturation (M_w^0), leading to a so-called z-spectrum for each pixel [78]:

$$Z(\Delta\omega) = \frac{M_{zw}(\Delta\omega)}{M_{0w}} \tag{3.7}$$

3.2.2 Features of the in vivo z-spectrum

Since the saturation transfer pathways in tissues are very complex, the interpretation of the in vivo data from saturation experiments is very challenging. Several overlapping effects observed in the in vivo z-spectrum are discussed below [64, 78]:

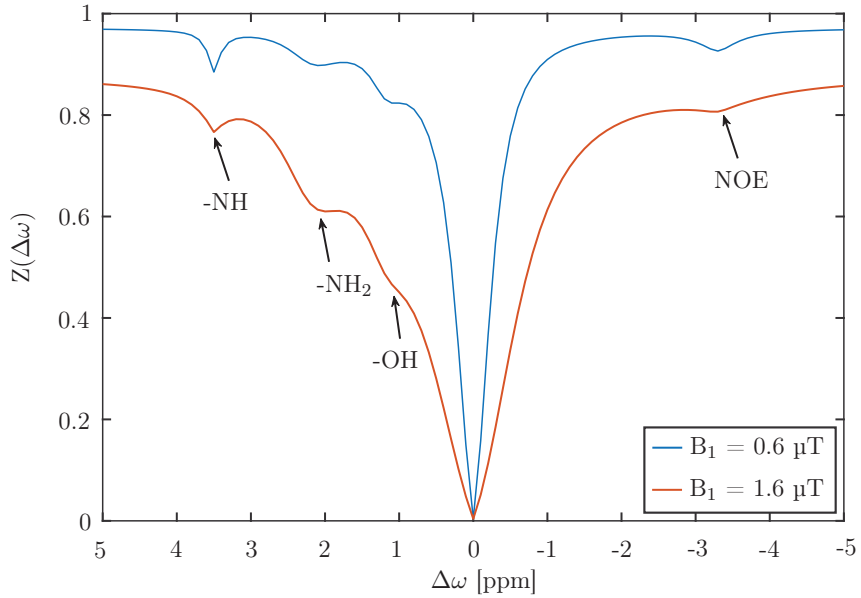

Figure 3.4: Simulated z-spectra at B_0=9.4T. Direct water saturation of the water hydrogen protons leads to a signal collapse around 0 ppm. The non-selective semi-solid macromolecular MT effect is scattered over a wide range of frequency offsets, determining the baseline. The CEST effects from protons in hydroxyl (OH), amine (NH_2), and amide (NH) functional groups are clearly visible at around 1 ppm, 2 ppm and 3.5 ppm, respectively. At about -3.5 ppm upfield from the water resonance, contributions of aliphatic NOE can be observed. The spillover effect, the labeling efficiency and the selectivity of the CEST effects are B_1-dependent.

Direct water saturation (DWS)

The normalized signal M_{zw}/M_{0w} is minimal at the actual water proton frequency (0 ppm) and becomes maximal far off-resonance. The CEST effect can be sometimes masked by the concomitant direct water saturation effect, especially when the solute protons resonate close to the water peak, as in the case of hydroxyl proton groups or when using strong B_1. This impact on the CEST pool resonance is called spillover. In tissue, the effects of the direct water saturation (DWS) increase due to the short T_2 [64].

Semi-solid macromolecular magnetization transfer (MTC)

The semi-solid MT results from the exchange processes between the protons bound to the surface of macromolecules and protons that are unbound in free water pool. Macromolecular MT builds strongly broadened resonances in the proton spectrum (linewidths of several kHz), due to the rapid T_2 relaxation in the microsecond range. Conventionally it is assumed that the semi-solid macromolecular pool line shape is symmetric around the water resonance and can be approximated with a super-Lorentzian line [64, 79].

CEST effect

In the range of frequencies higher than the water proton resonance (i.e. downfield from water), the CEST effects attributable to labile protons of functional groups of e.g. amides, amines and hydroxyl groups are visible. A number of different CEST proton pools have been systematically investigated in several previous studies. Examples of endogenous CEST-active targets and their exchange-related properties are listed in table 3.1. The most widely investigated CEST contrast to date is amide CEST, also known as amide proton transfer (APT). The major contributors to APT are the amides in the backbone of endogenous mobile proteins and peptides that resonate at around 3.5 ppm [80, 81]. Several promising clinical applications of APT-weighted CEST such as non-invasive imaging of ischemic stroke and brain tumors have been demonstrated [82–84]. Another pool includes amine and guanidinium proton groups that can be found in amino acids and peptides with chemical shifts ranging from about 1.8 ppm to 3 ppm [18, 64, 78]. Several metabolites containing exchangeable amine and guanidinium protons have been exploited for CEST, such as glutamate in the brain and creatine in the brain and muscle [23, 24]. The hydroxyl group protons resonate at about 1 ppm from the water resonance [18]. Two important endogenous metabolites containing hydroxyl functional groups are sugars e.g. myo-inositol in the brain, glycogen in liver, and muscle and glycosaminoglycans (GAG) in cartilage. Because the exchangeable proton resonances are relatively wide, the specificity of the CEST method is limited [64]. Thus, an unambiguous assignation of the CEST peaks in the z-spectrum to individual metabolites in vivo is generally not possible. Nevertheless, knowledge of the metabolic contributors in a specific tissue and their quantitative physical parameters such as chemical shift, exchange rate, concentration and relaxation rates enables a correlation between the apparent CEST effects at certain frequencies and predominant metabolites [78].

Exchange-relayed NOE (rNOE)

As described in the section 3.1.1, the polarization transfer can occur not only via chemical exchange, but also through dipolar coupling between the spins that are in close proximity. The most dominant effects are the so-called exchange-relayed NOE (rNOE) and inter- und intra-molecular NOEs [64, 78]. NOEs are observed on the right-hand side of the water peak at approximately -2.0 to -3.5 ppm and -1.6 ppm, corresponding to the frequency offset of aliphatic groups and choline phospholipids, respectively [64, 85]. The rNOE effects on mobile molecules are mostly difficult to detect due to interference from the MTC effect, which is also NOE based [86]. Similar as the CEST effects, rNOE are only visible at saturation amplitudes B_1 smaller than the exchange rate.

Table 3.1: Overview of selected CEST-active compounds with corresponding frequency shifts and exchange rates. The approximated exchange rates strongly depend on microenvironmental parameters such as pH and temperature. Adapted from [87].

Target	Functional group	δ_s [ppm]	k_{sw}[1/s]
Sugars	Hydroxyl protons (-OH)		
Glucose[1]	-OH	1.2, 2.2, 2.8	2000
Glycogen[2]	-OH	1.2, 2.2, 3.0	600
Myo-inositol[2]	-OH	0.8, 0.9, 1.1	600
Amino acids	Amino protons (-NH_2)		
L-Lysine[3]	-NH_2	3.0	4000
Alanine[4]	-NH_2	3.0	3030
Glutamate[2]	-NH_2	3.0	2000
Creatine[5]	Guanidinium protons	1.9	490
Miscellaneous			
Glycosaminoglycans[6]	-OH, -NH	0.9-1.9, 3.5	>1000, 10-30
Proteins[7]	-NH	3.5	30-280

[1]Wiebenga-Sanford et al. [88], [2]Lee et al. [89], [3]Liepinsh et al. [90], [4]Wermter et al. [91], [5]Stabinska et al. [92], [6]Vinogradov et al. [21], [7]Zhou et al. [81]

3.2.3 Analytical solution of the Bloch-McConnell equations

The BM equations can be solved using an eigenspace approach as described by Trott et al. [75, 93] and Zaiss [78]. It has been shown that in the case of an RF irradiation with duration $t_{sat} \gg T_{2w}$ and effective field $\omega_{eff} \gg 1/T_2$, the only significant contribution to the residual water magnetization of the water pool $\vec{M}_w$ is collinear with an eigenvector $\vec{v_1}$, which is oriented along the effective field $\omega_{eff} = (\omega_1, 0, \Delta\omega)$. The effective field is titled by the angle $\theta = tan^{-1}(\omega_1/\Delta\omega)$ off the z-axis of the rotating frame.The smallest eigenvalue in modulus λ_1 of the eigenvector $\vec{v_1}$ is proportional to the k_{ws} and identical with the spin relaxation rate constant in the rotating frame, $R_{1\rho}$:

$$\lambda_1 = R_{1\rho} \tag{3.8}$$

which was described previously by Trott and Palmer [75]. Using this fundamental result, the monoexponetial decay of the z-magnetization and thus the solution for the z-spectrum (equation 3.7) can be described as [76]:

$$Z(\Delta\omega, t_{sat}) = |Z_i cos^2\theta(\Delta\omega) - Z^{ss}(\Delta\omega)|e^{-R_{1\rho}(\Delta\omega)t_{sat}} + Z^{ss}(\Delta\omega) \tag{3.9}$$

The initial magnetization Z_i decays with the longitudinal relaxation rate $R_{1\rho}$ towards *steady-state* given by:

$$Z^{ss}(\Delta\omega) = \frac{R_{1w} cos^2\theta(\Delta\omega)}{R_{1\rho}(\Delta\omega)} \tag{3.10}$$

In the case of a simple two-pool exchanging system $R_{1\rho}$ is given by:

$$R_{1\rho}(\Delta\omega) = R_{eff}(\Delta\omega) + R_{ex}(\Delta\omega) \tag{3.11}$$

where R_{ex} is the exchange-dependent relaxation in the rotating frame. The term R_{eff} arises from the direct water saturation without exchange terms and can by approximated by [75]:

$$R_{eff}(\Delta\omega) = R_{1w}cos^2\theta(\Delta\omega) + R_{2w}sin^2\theta(\Delta\omega) = R_{1w} + (R_{2w} - R_{1w})\frac{\omega_1^2}{\omega_1^2 + \Delta\omega^2} \quad (3.12)$$

The CEST contrast is induced by the exchange-dependent relaxation rate R_{ex}, which is rather a complicated function of various parameters. In the large-shift limit (LS) ($\delta\omega_s \rightarrow \infty$), R_{ex} simplifies to:

$$R_{ex}(\Delta\omega) \approx R_{ex,LS}(\Delta\omega) = R_{ex,LS}^{max}\frac{(\Gamma_s/2)^2}{(\Gamma_s/2)^2 + (\Delta\omega - \delta_s\omega_s)^2} \quad (3.13)$$

thus R_{ex} can be expressed as a Lorentzian function of $\Delta\omega$ centered at $\Delta\omega_s$ with the linewidth:

$$\Gamma_s = 2\sqrt{\frac{R_{2s} + k_{sw}}{k_{sw}}\omega_1^2 + (R_{2s} + k_{sw})^2} \quad (3.14)$$

The maximum value of $R_{ex,LS}$ at $\Delta\omega_s = 0$, is the value of the label scan and is given by:

$$R_{ex,LS}^{max} = f_s k_{sw} \underbrace{\frac{\omega_1^2}{\omega_1^2 + k_{sw}(k_{sw} + R_{2s})}}_{\alpha(\omega_1)} \quad (3.15)$$

with the fractional concentration f_s. The labeling efficiency $\alpha(\omega_1)$ yields a measure of the quality of labeling of pool s, which depends not only on the B_1 amplitude, but also on the exchange rate k_{sw}. In the full saturation limit ($\omega_1 \gg k_{sw} + R_{2s}$ and LS), $\alpha \approx 1$ and thus $R_{ex,LS,FS}$ can be approximated as follows:

$$R_{ex,LS,FS} \approx f_s k_{sw} = k_{ws} \quad (3.16)$$

From equation 3.16 it becomes apparent that for large chemical shifts (LS) and maximal labeling efficiency (FS), the exchange-dependent relaxation rate R_{ex} equals the back exchange rate k_{ws}.

3.2.4 Exchange regimes

Overall, three exchange regimes can be defined by the field strength B_0, the chemical shift $\delta\omega_s$ and the exchange rate k_{sw} [78]:

$$k_{sw} \begin{cases} \gg \delta\omega_s, & fast \\ \approx \omega_s, & intermediate \\ \ll \delta\omega_s, & slow \end{cases}$$

As shown above, the exchange rate between an exchangeable site and water affects the observed CEST signal significantly. Very slow exchange provides little CEST effect as relaxation effects dominate. This means that the saturated protons of pool s will relax

back to the Boltzmann equilibrium before exchange can transfer the saturation to the bulk water pool w [94]. Similarly, the CEST effect is also diminished at very fast rates at which the resonances of the two individual species coalesce into a single broad peak [95]. In order to observe two distinct resonance peaks at water w and solute s pools, the exchange rate must be in the slow to intermediate regime [19]:

$$k_{sw} \leq \Delta\omega \tag{3.17}$$

3.2.5 Pulsed saturation

As already mentioned above, for pulsed-CEST imaging, continous-wave (CW) irradiation is replaced by the repetitive RF pulses of a duration t_{pd} with an inter-pulse delay of t_{ipd}. Assuming that the behavior of the z-component of the magnetization can be described by an $R_{1\rho}$ decay during the saturation pulse and an R_{1w} recovery during the inter-pulse delay, the following formula for the steady-state magnetization Z^{SS} in a pulsed experiment is obtained [78]:

$$Z^{SS}_{pulsed}(\Delta\omega) \approx \frac{R_{1w}(1 - DC + cos\theta \cdot DC)}{R_{1\rho}(\Delta\omega) \cdot DC + R_{1w}(1 - DC)} \tag{3.18}$$

where the duty cycle $(DC) = \frac{t_{pd}}{t_{pd}+t_{ipd}}$. Equation (2.28) is only valid if $t_{pd}, t_{ipd} \gg \frac{1}{R_{1s}+k_{sw}}$.

3.2.6 Z-spectrum analysis

As shown above, the analysis of the in vivo z-spectrum is challenging due to the spillover, concomitant magnetization transfer effects, and residual T_{1w}. In order to isolate the CEST effect of the pool of interest s, the exchange-dependent relaxation rate $R_{ex,s}$ must be separated from the direct water saturation R_{eff}, and residual T_{1w} relaxation of water.

The most widely used CEST quantification metric is the asymmetry analysis of the magnetization transfer ratio [80]. It can be determined by acquiring, in addition to the label z-value $Z_{lab} = Z(\Delta\omega)$ given by equation 3.10, a reference z-value $Z_{ref} = Z(-\Delta\omega)$ at the opposite frequency. The magnetization transfer ratio asymmetry MTR_{asym} can then be obtained as follow:

$$MTR_{asym} = Z^{ss}_{ref} - Z^{ss}_{lab} = \frac{R^{max}_{ex} R_{1w}}{R_{eff}(R_{eff} + R^{max}_{ex})} \tag{3.19}$$

Since the effect of direct water saturation does not appear in the numerator, the MTR_{asym} metric is called spillover correction of zeroth order. To remove the residual R_{eff} term from the denominator, an inverse metric has been proposed by Zaiss et al. [76]:

$$MTR_{Rex} = \frac{1}{Z^{ss}_{lab}} - \frac{1}{Z^{ss}_{ref}} = \frac{R_{ex}}{R_{1w} cos^2\theta} \tag{3.20}$$

A simple multiplication of MTR_{Rex} with the measured R_{1w} allows correction of water relaxation effects and yields the apparent exchange-dependent relaxation rate (AREX) [96]:

$$AREX = MTR_{Rex} \cdot R_{1w} = \frac{R_{ex}}{cos^2\theta} \tag{3.21}$$

For pulsed saturation, the inverse metrics can be easily scaled by the duty cycle (DC) [97]:

$$MTR_{Rex} = DC \cdot \left(\frac{1}{Z^{ss}_{lab}} - \frac{1}{Z^{ss}_{ref}}\right) = DC \cdot \frac{R_{ex}}{R_{1w} cos^2\theta} \tag{3.22}$$

$$AREX = DC \cdot \frac{R_{ex}}{cos^2\theta} \tag{3.23}$$

3.2.7 Quantitative parameter determination

Since the CEST effect varies with the proton exchange rate, labile proton ratio and experimental conditions such as the field strength B_0, irradiation power B_1 and water relaxation properties, there is a need to develop quantitative CEST analysis for determining underlying CEST parameters. The quantification of the back exchange rate k_{ws} is possible using the AREX metric. In the full-saturation (FS) and large shift limit (LS), $R_{ex} = k_{sw} \cdot f_s = k_{ws}$ (equation 3.16) and $cos^2\theta \approx 1$, and hence from 3.23:

$$AREX = R_{ex} \cdot DC = k_{ws} \cdot DC \tag{3.24}$$

Thus, the chemical exchange rate k_{sw} between the solute pool and water can be estimated as follows:

$$k_{sw} = \frac{AREX}{f_s \cdot DC} \tag{3.25}$$

with the proton fraction (or labile proton ratio) f_s given by:

$$f_s = \frac{n_s}{n_w} \cdot \frac{c_s}{c_w} \tag{3.26}$$

where n_i and c_i are the concentration and number of exchangeable protons per molecule of pool i ($i = s, w$), respectively. It is assumed that $c_w = 55$ M and $n_w = 2$.

Several other analytical and numerical methods have been proposed to determine the proton fraction f_s and exchange rate k_{sw}. Two approaches to measure labile proton ratio-weighted exchange rate as a function of saturation time (QUEST) and saturation power (QUESP) have been introduced by McMahon et al. [74]. The chemical exchange rate is determined by fitting changes in the signal intensity after application of different saturation powers (QUESP) or saturation times (QUEST) to the modified Bloch-McConnell equations. Dixon et al. extended the QUESP method and showed that the CEST effect can be represented as a linear function of $1/B_1^2$ (the so-called Ω-plot) and that the proton exchange rate and labile proton ratio can be estimated independently by linear regression of the CEST signal [98]. Nevertheless, their study was limited to paramagnetic CEST agents that exhibit large chemical shifts, and whose (para) CEST effects are therefore not diluted by direct saturation effect. Sun et al. applied the spillover-corrected Ω-plot method to study endogenous CEST agents with small chemical shifts [99]. To adapt this approach for its use on clinical scanners, a new analytical model for the quantitative AREX-based Ω-plot analysis in the case of saturation using trains of Gaussian-shaped RF pulses has been proposed [97]. This model introduces pulse-specific form factors c_1 and

c_2 to extend the theory of CW CEST experiments for Gaussian-shaped pulses. Consequently, the exchange-dependent relaxation $R_{ex,LS}$ (equation 3.15) can be simply modified as follows [97]:

$$R_{ex}^{shaped} = f_s k_{sw} c_1 \frac{\omega_1^2}{\omega_1^2 + k_{sw}(k_{sw} + R_{2s})c_2^2} \tag{3.27}$$

where c_1 and c_2 depend solely on the width σ and length t_{pd} of a Gaussian–shaped pulse and are defined as follows:

$$c_1 = \frac{\sigma\sqrt{2\pi}}{t_{pd}} \tag{3.28}$$

$$c_2 = c_1 \cdot \sqrt{\sqrt{2}} = \frac{\sigma\sqrt{2\pi}}{t_{pd}} \cdot \sqrt{\sqrt{2}} \tag{3.29}$$

Combining equations 3.27 and 3.23, the corrected AREX can be approximated as:

$$AREX^{shaped-pulses} = DC \cdot f_s k_{sw} \cdot c_1 \cdot \frac{\omega_1^2}{\omega_1^2 + k_{sw}(k_{sw} + R_{2s}) \cdot c_2^2} \tag{3.30}$$

As a result, the relaxation-compensated Ω-plot takes the following form [97]:

$$\frac{1}{AREX} = \underbrace{\frac{(k_{sw} + R_{2s}) \cdot c_2^2}{DC \cdot f_s \cdot c_1}}_{m} \cdot \frac{1}{\omega_1^2} + \underbrace{\frac{1}{DC \cdot f_s \cdot k_{sw} \cdot c_1}}_{n} \tag{3.31}$$

Calculation of the slope m and the y-intersection n of the linear function of $1/\omega_1^2$, allows the quantification of f_s and k_{sw} using the following equations:

$$f_s = \frac{1}{c_1 \cdot DC \cdot n \cdot (-\frac{R_{2s}}{2} + \sqrt{\frac{R_{2s}^2}{4} + \frac{m}{n \cdot c_2^2}})} \tag{3.32}$$

$$k_{sw} = -\frac{R_{2s}}{2} + \sqrt{\frac{R_{2s}^2}{4} + \frac{m}{n \cdot c_2^2}} \tag{3.33}$$

3.3 Water-exchange (WEX) NMR spectroscopy

The single-voxel water-exchange (WEX) spectroscopy as described by Mori et al. [53, 100] can be interpreted as an inverse CEST experiment. The WEX sequence consist of selective labeling of bulk water protons followed by a mixing period T_m, during which the labeled water magnetization is transferred via chemical exchange and/or cross-relaxation to the solute pool s. In the subsequent period, the water resonance is suppressed by means of the WATERGATE (WATER suppression by GrAdient Tailored Excitation [101]) technique. The measured WEX signal of pool s depends on T_m and can be written as [71]:

$$S_s(T_m) = \underbrace{\frac{k_{ws} M_{zw}(0)}{k_{sw} + R_{1s} - R_{1w}}}_{C} [e^{-R_{1w} \cdot T_m} - e^{-(k_{sw} + R1s) \cdot T_m}] \tag{3.34}$$

where R_{1w}, R_{1s} are the longitudinal relaxation rates of the water w and solute pool s, respectively; k_{sw} is the chemical exchange rate between the pool s and pool w, whereas k_{ws} is the back-exchange rate; $M_{zw}(0)$ describes the z-magnetization of the water protons at the beginning of the mixing period and C is a constant factor. The $k_{sw} + R_{1s}$ as well as R_{1w} values can be obtained from a fit of the equation 3.34 to the experimentally measured WEX signal. This is exemplified in figure 3.5.

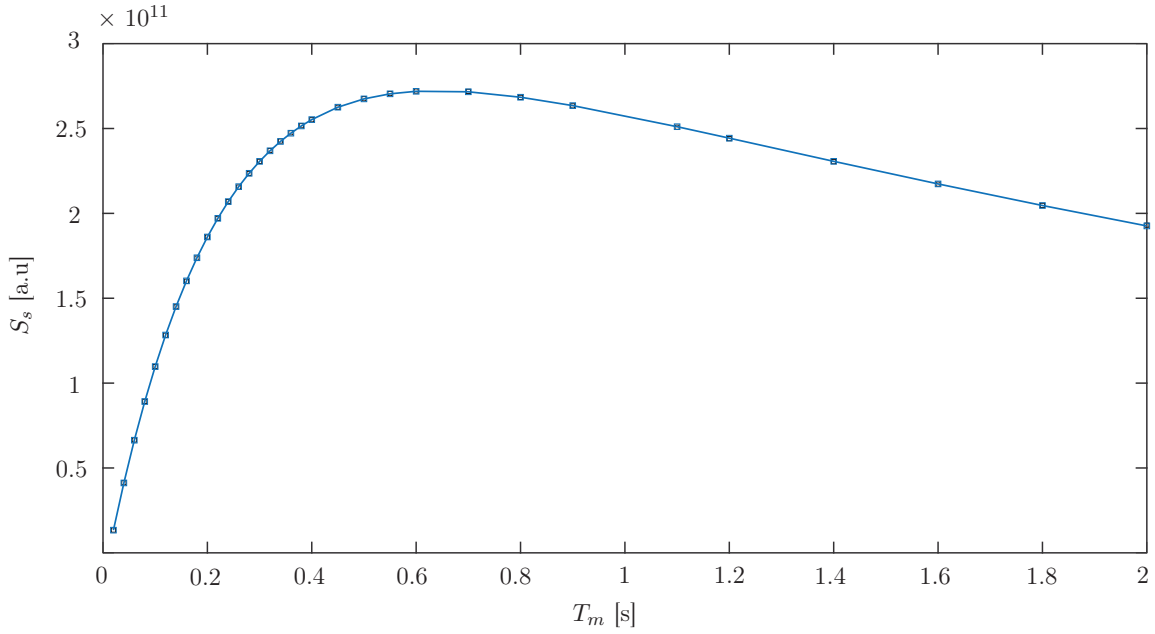

Figure 3.5: The experimentally determined integrated peak areas of the amide protons in urea and the fit function $S_s(T_m)$ at varying mixing times T_m. The plot shows data of the urea solution measured at pH 7 and at $T = 37°C$.

Chapter 4

Human kidney

4.1 Structure and function of the kidney

The kidneys are a pair of bean-shaped organs located on either side of the spine in the retroperitoneal space between the posterior abdominal wall and parietal peritoneum. In adults, each kidney is approximately 10-12 cm long, 6 cm wide and 2.5 cm thick [102]. The kidneys are well protected by the ribs and the muscles of the abdomen and back. Each kidney is surrounded by a capsule of adipose tissue that provides protection against jarring. Renal parenchyma is divided into two major structures, renal cortex and renal medulla, which are composed of individual filtering units known as nephrons. The renal cortex, which is approximately 1 cm in thickness, is the outermost layer. The inner renal medulla contains 8-18 cone-shaped renal pyramids. The base of each pyramid originates at the corticomedullary boundary, and the apex terminates in renal papilla, which lies within a minor calyx. The minor calyces join to form a major calyx, which in turn feed into renal pelvis. The renal pelvis narrows and becomes the ureter, which transports urine to the bladder [103]. Figure 4.1 illustrates the gross anatomy of the human kidney.

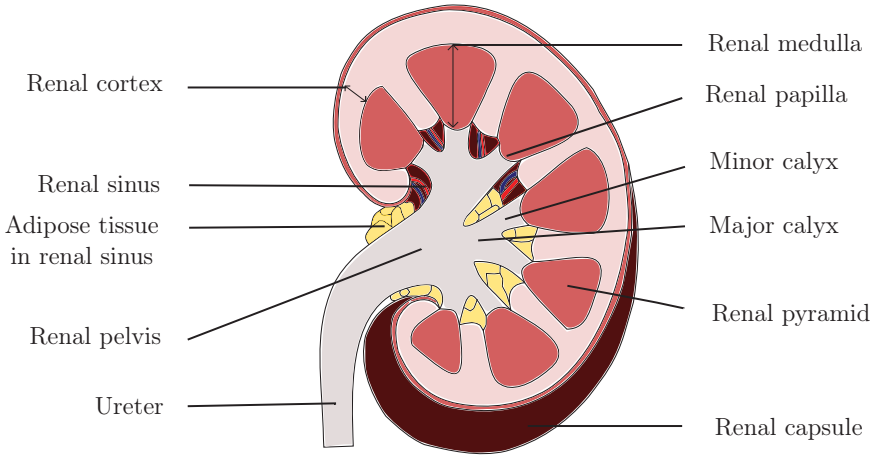

Figure 4.1: Gross anatomy of the human kidney. Kidney parenchyma is divided into two main structures: the inner renal medulla and outer renal cortex. The renal medulla is split up into renal pyramids. Renal papilla empties urine into a minor calyx. Two or three minor calyces converge to form a major calyces through which urine passes into the renal pelvis and ureter to the bladder. Adapted from [103, 104].

Each kidney receives blood from a renal artery, which branches into interlobar arteries, arcuate arteries, interlobular arteries, and then afferent arterioles. The latter diverge later into the capillaries of the glomerulus, which filter blood and produce glomerular filtrate that contains water, glucose, salts, amino acids and urea. The glomerular capillaries join together to form the efferent arteriole, which leads to peritubular capillaries, which in turn supply blood to the cortical nephrons. The venous drainage of the kidney runs parallel to the arterial vessels and forms the interlobular vein, arcuate vein, interlobar vein, and renal vein, which exit the kidney through the renal hilum. The functional unit of the kidney is the nephron, which is composed of a filtering component in the Bowman's capsule, a proximal convoluted tubule, a loop of Henle, a distal convoluted tubule and a collecting duct. Each kidney is made up of over one million nephrons that originate within the middle- or juxtamedullary cortex. The final portion of the nephron is the collecting duct, which concentrates urine from the DCT and then empties it into the renal pelvis and finally the ureter [103, 105]. Figure 4.2 depicts the structure of a nephron.

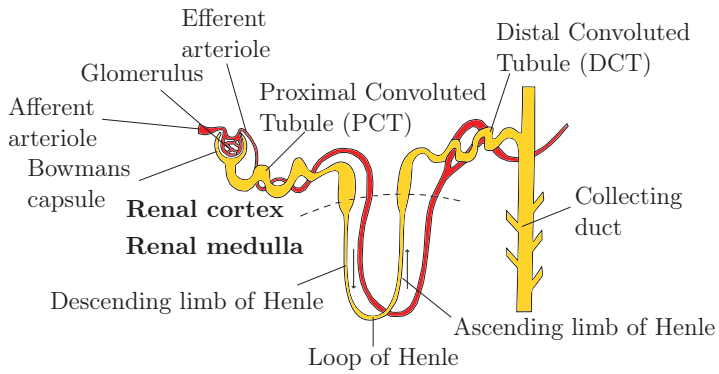

Figure 4.2: Structure of a nephron. Nephron consists of a renal corpuscle, a renal tubule and the associated capillary network. The renal corpuscle is composed of a network of capillaries, known as the glomerulus, and an encompassing Bowman's capsule. The renal corpuscle and the convoluted tubules are located in the cortex of the kidney, whereas the collecting ducts run through the medullary pyramids [103, 105]. Adapted from [103, 106].

In adults, filtrate is formed at the rapid rate of about 120-125 ml/min. This value describes the glomerular filtration rate (GFR). Maintenance of the GFR is essential for homeostasis of the body's extracellular fluids and acid-base balance [105, 107]. The estimated GRF (eGFR) is considered a key indicator of the renal function. Therefore, a persistently reduced or declining GRF is a specific diagnostic criterion for chronic kidney disease (CKD) [107].

Table 4.1: Glomerular Filtration Rate (GFR) in chronical kidney disease (CKD) stage. Adapted from [107].

Stage	GFR [mL/min/1.73 m^3]	Terms
G1	≥90	Normal or high
G2	60-89	Mildly decreased
G3a	45-59	Mildly to moderately decreased
G3b	30-44	Moderately to severely decreased
G4	15-29	Severely decreased
G5	>15	Kidney failure

4.2 Kidney metabolites as biomarkers for monitoring kidney function

The kidneys are active metabolic organs designed to concentrate and filter out water-soluble waste products and toxins while maintaining homeostasis [103]. Changes in serum and urine metabolite concentrations can occur as a result of impaired kidney function and can therefore be used to assess the filtration and to gain new insights into the pathophysiology of renal diseases [108].

According to the Urine Metabolome Database [109], the most abundant non-aqueous constituents of the human urine are urea (22.5 ± 4.4 mM/mM creatinine), creatinine (10.4 ± 2.0 mM), ammonia (2.8 ± 0.9 mM/mM creatinine), hippuric acid (298 ± 276.8 μ M/mM creatinine) and citric acid (280.6 ± 11.5 μ M/mM creatinine) [109]. As shown in a ^{1}H NMR study in rat model, renal tissue also contains high concentrations of lipid metabolites (triglycerides, cholesterol, poly- and monounsaturated fatty acids), carbohydrates (glycogen and glucose), cellular osmolytes (e.g. inositol, betaine, trimethylamine-N-oxide (TMAO), taurine), amino acids (glutamate, glutamine, citrate, aspartate) and the end products of glycolysis (lactate and alanine) [110].

Several previous metabolomics studies identified many small molecule metabolites, which have a potential to become useful biomarkers for monitoring kidney function and detecting renal diseases such as acute kidney injury (AKI), chronic kidney disease (CKD), diabetes nephropathy, chronic kidney allograft dysfunction and glomerulopathies [111,112]. For instance, a significantly increased level of allantoin, which is known marker of oxidative stress, has been measured in rat kidney transplants after ischemia/reperfusion. Similar study performed in human subjects with different degrees of kidney graft function revealed significantly reduced levels of choline, creatine, taurine and threonine in patients with lower GFR levels [113]. Further, the metabolomics analysis of serum samples collected in a large population-based study showed that the metabolites C-mannosyltryptophan and pseudouridine are strongly associated with eGFR and CKD [108].

Chapter 5

Aims

The present dissertation consists of three independent studies, examining the feasibility of CEST MRI to functionally image human kidneys.

Study 1 aimed to evaluate the potential of CEST imaging in 3T environment for quantifying CEST-related parameters such as chemical exchange rate and fractional concentration of exchanging protons. Previous quantitative CEST MRI studies have mostly been performed at higher magnetic field strengths and/or using continuous wave irradiation. Since the CEST analysis is significantly more challenging at lower fields and using pulsed saturation, the systematic evaluation of existing irradiation techniques and quantification methods on clinical MRI systems constitutes an important step towards future routine applications. In this study, the applicability of quantitative AREX-based CEST analysis in combination with two different pulsed saturation schemes was tested using both simulated and experimental data.

Study 2 investigated the proton exchange properties in urea solutions by WEX spectroscopy, and assessed the feasibility of urea-weighted CEST (urCEST) imaging. By determining the exchange rate constants of amide protons in urea as a function of pH and temperature at ultra-high magnetic field strength, reliable reference values for the subsequent quantitative CEST studies performed on a clinical scanner could be obtained. Besides urea, the pH-dependent CEST contrasts produced by other abundant kidney metabolites have been studied in order to: firstly, examine the specificity of urCEST; and secondly to gain a better understanding of the saturation transfer effects observed in the human kidney in vivo.

Study 3 focused on developing technical and methodological tools for CEST MRI in renal transplant recipients in vivo. Since the CEST imaging in the human kidney is affected by the perirenal and renal sinus fat, application of an effective fat removal technique may be crucial for obtaining reliable CEST quantification. In this study, Dixon-based water-fat separation method was utilized to obtain water-only CEST images. This required a development of a fast multi-echo gradient echo CEST pulse sequence, as described in chapter 9, and an adaption of the post-processing pipeline. Finally, the optimized Dixon-based CEST MRI protocol was applied to examine patients with transplanted kidneys.

In summary, the main purpose of the present dissertation was to investigate the potential of using endogenous CEST imaging to probe for chemical compounds and metabolites related to the kidney function, as well as to provide an acquisition and post-processing protocol for in vivo CEST MRI in renal transplant.

Chapter 6

Study 1: Quantitative pulsed CEST MRI at a clinical 3T system

The purpose of **study 1** was to assess the feasibility of performing quantitative CEST imaging at a clinical 3T MRI system. Up to now, quantitative CEST imaging has mostly been applied in non-human preclinical studies or at high field strengths (>7T) using continuous wave saturation pulses [74, 98, 99]. Although higher magnetic field strengths are beneficial to the CEST phenomenon, until recently 3T was the highest clinical field strength available. Moreover, due to the scanner specification and specific absorption rate guidelines only pulse train pre-saturation can be used in a standard clinical setup.

Previously, several analytical and numerical methods have been developed to determine quantitative parameters from the CEST-weighted images. For example, Dixon et al. showed that the CEST effect can be represented as a linear function of $1/B_1^2$ (the Ω-plot method) and that the proton exchange rate and labile proton ratio can be determined independently by a linear regression of the CEST signal [98]. Another approach, the so-called apparent exchange-dependent relaxation rate (AREX) metric was proposed by Zaiss et al. [96]. This method eliminates the spillover and semi-solid magnetization transfer effects and thus, facilitates quantification of the CEST effect on clinical systems. A theoretical model for pulsed-CEST experiments and an optimized saturation scheme was originally introduced by Schmitt et al. [114]. Finally, the analytic description of the spillover corrected Ω-plot method in the case of pulsed CEST was demonstrated by Meissner at al. [97].

In **study 1**, quantitative CEST parameters were evaluated using the AREX approach and the AREX-based Ω-plot method in combination with two different irradiation schemes based on Gaussian-shaped pulse saturation train and pulsed spin-lock preparation. For this purpose, first the Bloch-McConnell equations were solved for a two-pool exchange model as proposed by Murase et al. [115]. In order to validate the simulation results, CEST data gathered in MRI experiments performed on a clinical 3T MRI scanner using a cylindrical phantom filled with model creatine solutions at varying pH values and creatine concentrations were analyzed. The respective study can be found in Appendix A .

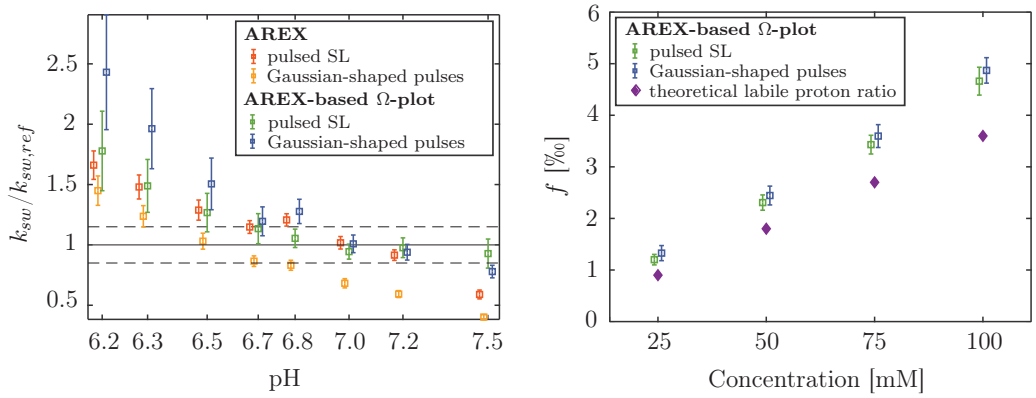

Figure 6.1: Graphical abstract - study 1. The exchange rates k_{sw} estimates determined at varying pH, normalized to the reference value $k_{sw,ref}$ [71] (left), and the labile proton ratio f estimates calculated at varying creatine concentrations (right).

6.1 Materials and methods

6.1.1 Numerical simulations

The Bloch-McConnell equation-based simulations were performed in Matlab (Matlab R2012a, Mathworks, Natick, MA, USA). A two-pool exchange model was assumed with representative $T_{1w} = 2.473$ s and $T_{2w} = 1.676$ s for the bulk water, and $T_{1s} = 0.5$ s and $T_{2s} = 0.015$ s for the labile protons at 1.9 ppm at 3T, respectively [115]. Further, the AREX metric and Ω-plot analysis were applied to the simulated data in order to assess the accuracy of the methods over a wide range of B_1, f and k_{sw} values. The results were normalized to the theoretical values from the Bloch-McConnell simulations k_{sw}^{norm} and the normalized labile proton ratio f^{norm}.

6.1.2 MR experiments

For MR experiments, eleven creatine model solutions dissolved in phosphate buffer were prepared at room temperature. The phantoms consisted either of creatine solutions with varying pH values (6.2, 6.3, 6.5, 6.7, 6.8, 7.0, 7.2, 7.5) at creatine concentration of 50 mM or varying molar concentration (25 mM, 50 mM, 75 mM, 100 mM) at pH 7.0.

All measurements were performed on a clinical 3T MR scanner (Magnetom Prisma, Siemens Healthineers, Erlangen, Germany). A 2D single-shot gradient echo sequence (GRE) was used for CEST image data acquisition [114]. The saturation modul consisted either of 50 Gaussian-shaped pulses, or 50 spin-lock pulses with $t_{pd} = t_{ipd} = 100$ ms and RF pulse amplitudes B_1 of 0.25, 0.5, 1.0, 1.25, 1.65 and 2.1 μT. A single spin lock pulse consists of an rectangular pulse with an amplitude B_1 flanked by two Gaussian-shaped RF pulses with a flip angle θ and an opposite phase, where θ is the angle between the effective field and the z-axis. WAter Saturation Shift Referencing (WASSR) method for

B_0-inhomogeneity correction was used [116]. Additionally, T_1-weighted MR images at different inversion delays (TI) were acquired by a turbo-inversion-recovery sequence and subsequently fitted to obtain the T_1 maps.

6.1.3 Data analysis

All data were processed using Matlab (Matlab R2012a, Mathworks, Natick, MA, USA). The AREX maps were T_1-corrected using the mean T_1 values obtained as an average of the four tubes of each phantom. The relaxation-compensated Ω-plot analysis was then applied to the AREX signal. The form factors of the pulses employed in this work were $c_1 = 0.5672$, $c_2 = 0.6171$ and $c_1 = c_2 = 1$, for the Gaussian-shaped and spin-lock pulses, respectively [97]. To assess the accuracy of the determined chemical exchange rate, the $k_{sw,ref}$ were calculated using an empirical formula obtained from the water-exchange NMR spectroscopy experiments conducted by Goerke et al. [71].

6.2 Results

6.2.1 Simulations

The results of the Bloch-McConnell simulations over a wide range of B_1, f and k_{sw} values revealed substantial differences in accuracy between the examined quantitative CEST methods (AREX and AREX-based Ω-plot). Moreover, it has been shown that the shape of the applied saturation pulse also affects the overall CEST quantification.

Regardless of the irradiation scheme and quantification method, low exchange rates were strongly overestimated in nearly whole considered range of B_1 values (Appendix A, figure 1). In general, however, the Ω-plot method showed larger validity area compared to the simple AREX metric. Furthermore, in contrast to the latter approach, the AREX-based Ω-plot method allows for simultaneous determination of the exchange rate and the fractional concentration. Both these parameters could be estimated accurately over a wide range of k_{sw} from the simulated spin-lock CEST data. Nevertheless, the accuracy of the estimation decreased at larger k_{sw} values, especially as the saturation power increased. The most accurate estimates of fractional concentration were calculated at lower k_{sw} and lower RF power (Appendix A, figure 2).

6.2.2 MR experiments

In general, the results of the in vitro MR experiments were consistent with those obtained from the Bloch-McConnell simulations. Again, the k_{sw} rates at lower pH were substantially overestimated regardless of the applied irradiation scheme and quantification method. The Ω-plot analysis in combination with the spin-lock saturation pulses showed the widest range of applicability for determining exchange rate k_{sw} and fractional concentration f among all considered approaches (Appendix A, figure 3).

Despite being constantly overestimated, the results verified the linear dependence of labile proton ratio on creatine concentration (Appendix A, figure 4). At the same time, the accuracy of the k_{sw} estimation increases with increasing fractional concentration f (Appendix A, figure 5).

6.3 Discussion

Both the Bloch-McConnell simulations and MR experiments in vitro showed that quantitative CEST imaging is generally possible on clinical 3T scanners. Particularly promising results were obtained using the AREX-based Ω-plot method in combination with the spin-lock preparation pulses.

All the considered quantification methods tend to overestimate lower exchange rates. In this regard, it should be noted that the pulsed approach used in **study 1** is based on an assumption that no magnetization transfer takes place during the interpulse delay. In fact, Roeloffs et al. showed that a bi-exponential decay of magnetization during the pause should be considered when modeling magnetization transfer effects [117]. For exchange rates that are comparable with the inverse of the interpulse delay, not taking into account this additional magnetization transfer during the break can result in a substantial overestimation.

The Bloch-McConnell simulations confirmed that the accuracy of the exchange rate determination is dependent on the exchange regime in which the analysis is performed. Using pulsed spin-lock preparation has proved particularly advantageous for estimating higher exchange rates. The results of the AREX-based Ω-plot analysis obtained on a 3T system showed smaller area of validity compared to those reported by Meissner et al. at 7T in the case of using Gaussian-shaped pulses [97]. In order to ensure sufficient specificity of detecting CEST effect from creatine, its specific frequency offset $\delta\omega_b$ should be larger than the exchange rate k_{sw}. Since the frequency shift increases with the magnetic field strength, the large-shift limit assumption ($\delta\omega_b \to \infty$) for creatine protons is easier fulfilled at higher magnetic field strength B_0 and smallerk_{sw} values.

The results of the simulations and the experimental studies revealed slightly different ranges of applicability of the considered quantification methods. This can be explained by systematic effects such as non-ideal form of the rectangular pulse, spatial dependency of the flip angle caused by B_1 inhomogeneity as well as B_0 inhomogeneity.

Study 1 had several limitations worth noting. Firstly, the reference values used here were calculated using the acid- and base- exchange rate constants (k_a and k_b, respectively) of guanidinium protons in creatine obtained by Goerke et al. [69]. In their study, the systematic estimation error of the k_a and k_b values was reported to be above 10% [69, 97]. Secondly, the apparent semi-solid molecular magnetization transfer and nuclear Overhauser effects that occur in vivo were not considered neither in the simulation nor phantom study. Thirdly, in the present work the applicability of the CEST quantification methods at 3T was assessed using only a creatine solution. The study of other endogenous CEST agents and multi-pool CEST systems could be the next step.

Quantitative CEST imaging at 3T has already been evaluated in vivo. For instance, Zaiss et al. applied the AREX method to calculate the exchange rates of labile amide protons in order to obtain absolute pH maps in ischemic rat brain tissue [96]. One limitation of that study was the use of the reported rather than estimated labile proton ratio value [118] for pH quantification. Recently, Zhou et al. applied the Ω-plot method in the intervertebral discs (IVDs) in a porcine model at a 3T MRI system. The determined exchange rates were closely correlated with pH values that were measured using a needle-shaped tissue pH probe. Nevertheless, the acquisition time of 30-40 min for one IVD is not clinically feasible [119]. Hence, new techniques for accelerating MRI acquisition such as compressed sensing or parallel imaging might be of interest for quantitative CEST MRI [120].

6.4 Conclusion

Quantitative CEST analysis allows for determination of exchange rate k_{sw} and labile proton ratio f of exchanging protons and it therefore represents an important step for improving the quality of CEST imaging. **Study 1** showed that the AREX-based Ω-plot analysis paired with the pulsed spin-lock saturation provides particularly promising results for intermediate-exchanging protons with k_{sw} values between 50 and 530 Hz. Nevertheless, further studies are needed to assess the applicability of the CEST imaging for determining quantitative parameters of other small metabolites.

Chapter 7

Study 2: Proton exchange in aqueous urea solutions measured by WEX and CEST

Study 2 aimed, firstly, at characterizing the proton exchange between water and urea protons by WEX spectroscopy and CEST imaging, and, secondly, at investigating other abundant kidney/urine metabolites with exchangeable protons that may provide a measurable CEST effect under physiological conditions.

As a major product of protein metabolism, urea plays a key role in maintaining acid-base homeostasis in mammals [121, 122]. Elevated serum urea level is an indicator of declining kidney function [123]. Since many renal diseases are associated with alterations in pH and urea gradients in kidney, a pH-sensitive imaging technique such as CEST could be a promising tool for clinical use [17, 124].

Two -NH_2 groups with four labile protons and its relatively high abundance in human blood and urine, make urea particularly attractive for endogenous CEST imaging in human applications. Exploring the exchange-related properties of urea is needed in order to achieve a better understanding of the saturation transfer effects measured in the kidney in vivo.

In 1998, Guivel-Sharen et al.reported that urea contributes dominantly to the measured CEST effect at ca. 1 ppm in rabbit kidney and urine [125]. Soon afterwards, Dagher et al. were able to map the urea distribution in a healthy volunteer kidney at a 1.5 T scanner using CEST MRI [126]. Except from a conference abstract in 2015, there were no further studies on urea-weighted CEST (urCEST) available at the time this study was conducted [127].

In **study 2**, WEX-NMR spectroscopy was utilized for determining exchange rate constants and activation energies of proton transfer reactions in aqueous urea solution. Moreover, the feasibility of performing quantitative urea-weighted CEST imaging at a 3T cilinical system was investigated. Further, to examine the specificity of urea-weighted CEST imaging in kidney, the CEST effect of several other important kidney metabolites such as creatinine, ammonia, hippuric acid was also studied. Eventually, the contribution of urea to the total CEST effect in urine was evaluated. The respective study can be found in Appendix B.

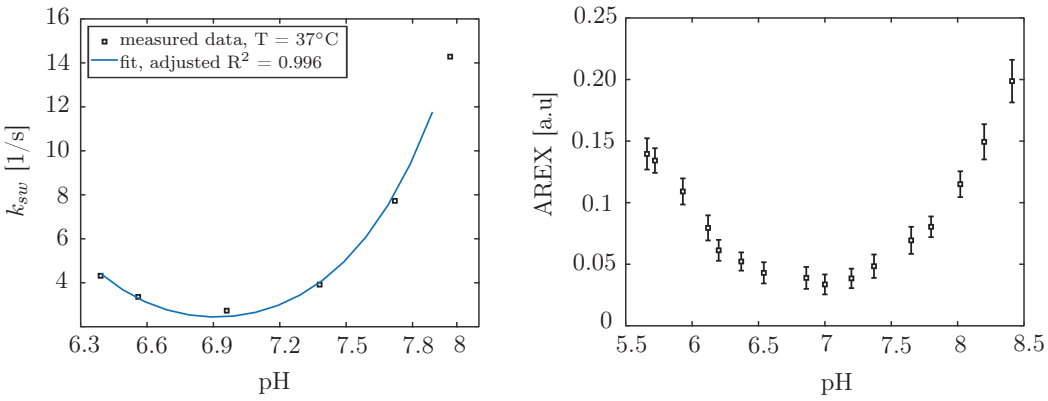

Figure 7.1: Graphical abstract - study 2. The exchange rates k_{sw} determined at varying pH and at T = 37∘C using WEX spectroscopy (left), and the AREX values calculated at varying pH from the CEST data (right).

7.1 Materials and methods

7.1.1 Phantoms

For the WEX study, six samples containing 250 mM urea solutions were prepared using 250 mM urea, 50 mM sodium/potasium phosphate buffer and 5% deuterium oxide were prepared at varying pH = 6.39, 6.56, 6.96, 7.38, 7.72, 7.97 and measured at $T = 37°C$. Two samples with pH = 6.56 and pH = 7.97 were additionally measured at varying temperatures $T = 22.0°C$, 27.0°C, 32.0°C and 37.0°C.

For the CEST study, sixteen model solutions with 250 mM urea were dissolved in 50 mM sodium/potasium phosphate buffer at pH = 5.66, 5.72, 5.93, 6.12, 6.20, 6.37, 6.54, 6.86, 7.00, 7.20, 7.37, 7.65, 7.80, 8.02, 8.20 and 8.41. Furthermore, four samples with varying urea concentrations of 10 mM, 25 mM, 50 mM and 100 mM were prepared at pH 7.60 and measured at $T = 37\pm1°C$

In order to examine the specificity of CEST imaging, several other kidney metabolites including creatinine, ammonia, hippuric acid, citric acid, taurine, creatine, histidine, glucose, glutamine, myo-inositol, alanine, lysine, allantoin, threonine, lactate, sorbitol, glutamic acid, choline and glycogen at pH 6.2, 6.6, 7.0 and 7.4 were also investigated. Additionaly, individual and mixed aqueous solutions of urea, creatinine and creatine at their normal concentrations in urine were made. Further, an urine sample from a healthy volunteer was collected.

7.1.2 WEX and CEST experiments

The WEX spectra were acquired on a Bruker Avance III HD 600 MHz NMR spectrometer (Bruker, Ettlingen, Germany) located at the Jülich-Düsseldorf Biomolecular NMR Center, using a modified WEX II pulse sequence with 33 different mixing times T_m ranging from 20 ms to 2000 ms (Appendix B, figure 1).

The CEST spectra were collected on 3T whole body MR clinical scanners (Magnetom Trio and Magnetom Prisma, Siemens Healthineers, Erlangen, Germany). The CEST saturation mode consisted of 50 Gaussian-shaped pulses with low RF irradiation amplitude B_1 = 1.0 μT and pulse/interpulse duration $t_{pd} = t_{ipd}$ = 100 ms. The B_0-maps were acquired using a WASSR protocol [116], while the T_1-maps were obtained from the T_1-weighted MR images collected at different inversion delays by a turbo-inversion-recovery sequence.

7.1.3 Data analysis

Analysis of the CEST data was performed using in-house written programs in Matlab (Matlab R2012a, Mathworks, Natick, MA, USA). The WEX spectra were processed using NMRPipe and NMRDraw [128]. The exchange rates of urea from the WEX data were calculated as described in section 3.3. For the exchange rate quantification using CEST, an extended AREX metric was used [96, 117].

7.2 Results

7.2.1 Exchange rates and activation energies of urea

Study 2 verified the assumption of bi-exponential dependence of urea exchange rate on pH (Appendix B, figure 4a and figure 5a). Nevertheless, the acid-catalyzed rate constant $k_a = (9.95 \pm 1.11) \times 10^6$ l/(mol·s) was much faster than the base-catalyzed rate constant $k_b = (6.21 \pm 0.21) \times 10^6$ l/(mol·s), as measured in the WEX experiment. Moreover, the Arrhenius plot showed that the data followed a linear behavior as expected for a thermally activated process (Appendix B, figure 4b). Using these results it was possible to estimate the activation energies for the base- and acid-catalyzed proton exchange: $E_{A,a} \approx (19 \pm 4)$ kcal/mol and $E_{A,b} \approx (10 \pm 2)$ kcal/mol.

In general, the chemical exchange rates of urea derived from CEST and WEX experiments were in good agreement (Appendix B, table 2). Although urea protons undergo slow exchange with water protons, it was possible to estimate its exchange rate at pH values below 6.2 and above 7.4 at a temperature of $T = 37°$C from the CEST experiments. The bi-exponential dependence of the AREX values confirmed that the proton exchange in urea solutions is both acid- and base-catalyzed (Appendix B, figure 5a). Moreover, the AREX metric was linearly proportional to the urea concentration (Appendix B, figure 5b).

7.2.2 CEST effect of other kidney metabolites

Based on the results form animal [110] and human [113] studies on kidney tissues as well as the Urine Metabolome Database [109], major kidney metabolites, which may provide an experimentally measurable CEST effect under physiological conditions, were identified (Appendix B, Table 3).

While all of the examined metabolites possess exchangeable protons, not all of them generated a detectable CEST contrast at 3T in the pH range of 6.2 - 7.4 and at a temperature of $T = 37°C$. The highest CEST effect under physiological conditions showed creatinine, creatine, glutamine, alanine, allantoin and glutamate (Appendix B, Figure 6).

7.2.3 Specificity of urea-weighted CEST imaging

The z-spectrum and the MTR_{asym} curve of the mixed phantom consisted of urea, creatinine and creatine at their normal urine concentration and at pH 5.97 were similar to those obtained in the urine sample at pH 5.90. Both CEST spectra revealed a dominant peak at ca. 1 ppm, which could be assigned to the exchanging amide protons of urea (Appendix B, Figure 7).

7.3 Discussion

In general, the exchange rate constants determined experimentally using the WEX spectroscopy are in good agreement with previous studies [67, 129, 130]. Direct comparison is, however, difficult due to differences in the experimental conditions, such as the buffer concentration and temperature. Interestingly, the acid-catalyzed rate constant of urea is much larger compared to rate constants for acid-catalyzed protolysis of most amides. This fact suggests higher probability of a collision of H_3O^+ with nitrogen than with oxygen, resulting in an observable proton transfer [66, 129]. The estimated activation energies for base- and acid-catalyzed proton exchange in urea solution are in good agreement with the apparent heat of activation for amide hydrogen [131, 132].

The water exchange (WEX) filter sequence has been previously shown to be useful for measuring exchange rates of slowly exchanging species [53,132,133]. In **study 2**, the WEX II sequence was applied to amide exchange in aqueous urea solutions. However, due to the large width of thee urea peak and its nearness to the water peak, the excitation sculpting instead of WATERGATE technique was used for water suppression [134]. Although the WEX spectroscopy provides valuable information about magnetization transfer exchange and relaxation properties of metabolites, the overall low sensitivity and lengthy acquisition limit its applicability in vivo.

CEST imaging has potential to overcome these challenges. As a matter of fact, the exchange rates of urea derived from CEST experiments were in good agreement with those obtained from the WEX spectra. Nevertheless, it was not possible to determine the k_{sw} values of urea in the physiologically relevant pH range. In the neutral solutions, the CEST effect was minimal and thus the signal to noise ratio (SNR) was insufficient for a proper

quantification. Moreover, because of the high noise level and small B_1 dispersion at low k_{sw}, the Ω-plot method that enables an independent determination of exchange rate and proton fraction was not applicable [69, 92].

In **study 2**, a number of most abundant kidney/urine metabolites with labile protons that may produce a CEST contrast were investigated. However, only few of them showed a measurable CEST effect under physiological conditions at 3T. These might potentially overlap with the urea CEST signal in the kidney and thus, the absolute urea quantification might be considerably hampered. In the case of the hydroxyl and amine protons, their exchange rates usually do not fulfill the condition of slow to intermediate exchange on the NMR time scale at lower magnetic field strengths, and therefore showed no or only modest CEST effect. Moreover, the resonance peaks of hydroxyl protons of e.g. glucose, glycogen and myo-inostiol were too close to water to be detected. Hence, it is unlikely that any of these compounds contribute to the total CEST contrast at ca. 1 ppm in kidney/urine at 3T.

The pH values measured in healthy mice kidneys using an exogenous CEST agent has been shown to vary between 5.4 and 7.4 [135]. Because of the very slow exchange rate of urea in this pH range, it might be challenging to obtain the pH maps by applying only the quantitative urea-weighted CEST imaging.

7.4 Conclusion

Study 2 presents a successful application of the WEX spectroscopy for determining exchange rate constants and activation energies of urea, and proves the feasibility of quantitative urea-weighted CEST imaging on a clinical 3T MRI system. This study confirmed that urea protons undergo a slow proton exchange with water protons. Moreover, both the WEX and CEST experiments showed that the chemical exchange in urea solutions is acid- and base-catalyzed. Besides urea, several other small kidney metabolites that may contribute to the total CEST signal observed in the kidney were identified.

Chapter 8

Study 3: Dixon-based CEST MRI in renal transplant recipients

In **study 3** the feasibility of performing CEST imaging in renal transplant patients on a clinical 3T MRI system was investigated. The primary focus was to develop and optimize an acquisition and a post-processing protocol for renal transplant CEST imaging, which remains technically challenging and volatile due to the presence of fat in and around kidneys and large magnetic field inhomogeneities [136].

Kidney transplantation has become the preferred renal replacement therapy in patients with end stage renal disease (ESRD) [137]. Routine postoperative monitoring of allograft renal function rely on the measurement of biochemical markers, biopsies and imaging modalities including MRI [138]. Recent preclinial study suggest that CEST MRI can provide new molecular insights into renal diseases, and therefore usefully complement the existing techniques [40–44].

In **study 3**, the CEST acquisition protocol and post-processing pipeline for in vivo kidney transplant imaging on a clinical 3T MRI system has been developed and validated in an egg phantom and in renal graft recipients. A particular focus was placed on suppressing strong lipid signal upfield from the water resonance, which may lead to an erroneous amide proton transfer (APT), as shown in several previous studies [139–141]. In the present work, effective fat separation was achieved by applying the modified two-point Dixon method (2pt Dixon) [142]. Using the optimized CEST protocol, it was possible to quantify the cortical and medullary CEST effects in three frequency ranges centered at 1 ppm, 2 ppm, and 3.5 ppm, corresponding to the frequency offsets of hydroxyl, amine and amide protons, respectively. The respective study can be found in Appendix C.

8.1 Materials and methods

8.1.1 Phantom and subjects

Fresh hen egg was imaged at 3T to verify the effectiveness of the bipolar Dixon method for the water-fat separation in CEST data. Whereas the egg white consist mainly of water and proteins (about 11%), the egg yolk contains in addition to proteins (about 16%) also high amount of fat (about 37%) [143]. In fact, the egg phantoms have often been used to analyze the origin of the APT signal in tissue [144, 145].

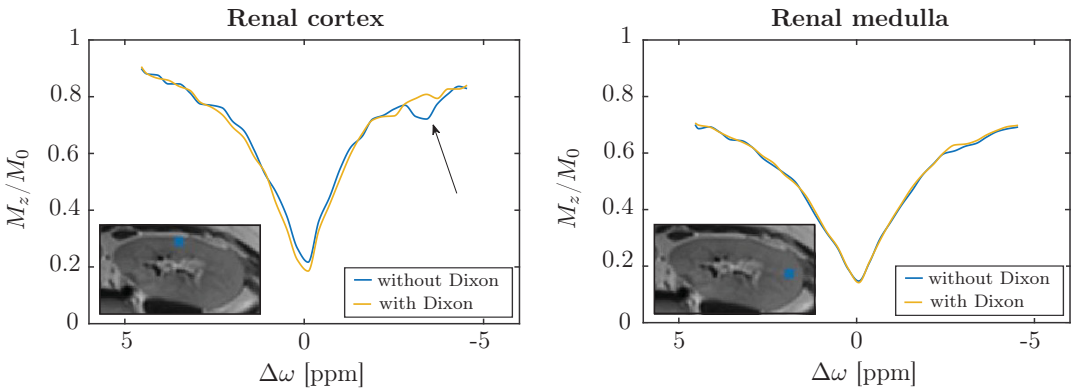

Figure 8.1: Graphical abstract - study 3. Exemplary z-spectra from individual pixels measured with and without Dixon in the renal cortex/capsule (left) and renal medulla (right). In the lipid-abundant renal capsule, the signal at about -3.5 ppm was effectively suppressed in the Dixon-based z-spectrum. At the same time, in the renal medulla which is essentially free of fat influence, negligible difference between the z-spectra obtained from the water-only and conventional CEST images can be observed

The study cohort included 14 renal transplant recipients (5 females and 9 males; age range: 23-78 years; mean age: 51 ± 16.8). The in vivo MR experiments were approved by the local ethics committee, and the written informed consent was obtained from all participants. All MR images were obtained without any restriction on fluid or food intake prior to MRI [146].

8.1.2 MRI experiments

All experiments were conducted on a 3T MAGNETOM Prisma MRI system (Siemens Healthcare, Erlangen, Germany). The MR protocol consisted of a half-Fourier single-shot turbo spin echo (HASTE) sequence for high-resolution anatomical scan, a self-developed multi-echo CEST sequence (see chapter 9) and a WASSR experiment. CEST experiments were performed using 15 Gaussian-shaped RF pulses with a single pulse duration t_{pd} = 100 ms, an interpulse duration t_{ipd} = 100 ms and B_1 = 1.2 μT, followed by a dual-echo gradient echo imaging. The CEST images were acquired at 41 frequency offsets from -6 ppm to 6 ppm. The imaging parameters were: transversal field-of-view (FOV) = 380 × 380 mm^2 and voxel size = 1 × 1 mm^2 for human data, and coronal FOV = 240 × 240 mm^2 and voxel size = 0.9 × 0.9 mm^2 for phantom data, slice thickness = 5 mm, TR/TE$_1$/TE$_2$ = 4.2/1.5/2.5 msec, number of averages = 2. The WASSR z-spectra were obtained at 34 equidistant frequency offsets between ±1 ppm.

8.1.3 Data analysis

The CEST data were processed in Matlab (Matlab R2018a, Mathworks, Natick, MA, USA). For each frequency offset, 1) the water-only image, 2) fat-only image, 3) in-phase image (IP) and 4) out-of-phase (OP) image were generated using the 2-pt Dixon method [142]. The B_0 map has been calculated from the WASSR data. To assess the feasibility of the Dixon method for effective water-fat separation, z-spectra obtained from the phantom data acquired with and without Dixon were compared.

For the in vivo evaluation, cortical-medullary regions of interest (ROIs) were manually segmented on the anatomical images by an experienced radiologist using image segmentation toolbox ITK-SNAP [147]. Further, region-of-interest (ROI)-averaged MTR_{asym} values were calculated in three frequency ranges (i) 0.8-1.2 ppm (ii) 1.8-2.2 ppm, and (iii) 3.3-3.7 ppm, corresponding to respectively hydroxyl, amine, and amide frequency offsets. The cortical and medullary MTR_{asym} values measured using the conventional and Dixon-based CEST method were then statistically compared using multiple paired t-test with Bonferroni correction using SpecVis (https://github.com/hezoe100/SpecVis).

8.2 Results

8.2.1 In vitro MR experiments

In the z-spectra obtained in the egg yolk from the IP-CEST data a large fat dip at about - 3.5 ppm can be observed. This peak was effectively suppresed after applying Dixon method (Appendix C, figure 1B). Moreover, higher suppression level around the water resonance was obtained in the water-only data. This is consistent with the literature [141]. At the same time, the z-spectra calculated in the egg white with and without Dixon were similar, indicating that the CEST effect at 3.5 ppm is not affected by the Dixon water-fat decomposition (Appendix C, figure 1A).

8.2.2 In vivo MR experiments

Two datasets had to be excluded due to severe motion artifacts. The overall quality of the remaining MR data, and the corresponding water-only images obtained by Dixon was good (Appendix C, figure 2), and allowed the subsequent CEST analysis.

The ROI-based CEST analysis in the three frequency ranges revealed that the overall MTR_{asym} values decreased with increasing frequency offset. The highest CEST effect was measured at about 1 ppm, indicating urea as a major contributor to the total CEST signal measured in the human kidney. This is in line with previous literature [87,126]. In the lipid-abundant renal capsule, the fat peak at about -3.5 ppm was effectively suppressed after applying Dixon method (Appendix C, figure 3B). In the renal medulla that is essentially free of fat influence, only a negligible difference between the z-spectra obtained from the water-only and conventional CEST images could be observed (Appendix C, figure 3A).

The MTR_{asym} values obtained at 3.5 ppm from the water-only images (-0.06 ± 0.62% for cortex, 0.32 ± 0.62% for medulla) were significantly higher than those obtained from the IP-CEST data (-1.0 ± 1.0% for cortex, -0.12 ±0.78% for medulla) at a significance level of $P < 0.05$. At the same time, there were no significant differences in the hydroxyl and amine MTR_{asym} values between the IP-, OP-, and Dixon-based CEST quantification. The OP-CEST data (0.8 ± 1.4% for cortex, 0.8 ± 0.9% for medulla) led to significantly higher cortical and medullary amide MTR_{asym} values compared to the IP non-Dixon data at a significance level of $P < 0.05$, due to signal interferences and normalization [140] (Appendix C, Table 1). Besides the effective water-fat separation, Dixon-based CEST analysis led to an overall lower range of variability of the datasets (Appendix C, Figure 4).

8.3 Discussion

In the present study, an optimized CEST acquisition and post-processing protocol tailored to the renal graft applications was optimized for the application in the human renal transplant, which is considered challenging due to the severe field inhomogeneity and presence of the perirenal and renal sinus fat.

To improve the reliability of the in vivo CEST MRI quantification in lipid-abundant regions, the fat contribution should be effectively eliminated as shown in several previous studies [141, 148]. Here, the utility of a two-point Dixon-based water-fat separation for removing lipid artifacts in CEST imaging was confirmed in phantom and in vivo experiments. The lipid peak at -3.5 ppm was effectively suppressed in the water-only images, leading to significantly higher cortical amide MTR_{asym} values compared with those measured from the IP-CEST data. At the same time, the Dixon water-fat separation did not introduce any additional asymmetries to the CEST spectrum, and therefore the hydroxyl and amine CEST effects were not affected by the Dixon post-processing. Moreover, the variability of the Dixon-MTR_{asym} values was slightly reduced compared with the non-Dixon values. One possible explanation for this could be the fact that a single water-only image is generated using two CEST images, resulting in higher signal-to-noise ratio (SNR).

Despite all the above-mentioned advantages of using the Dixon method in combination with the CEST acquisition, there are still some issues that should be considered when analyzing the results of the present study. Firstly, the assumption of nonsaturated water and fat peak, which is usually made in the Dixon-based separation model, is clearly violated when performing CEST imaging. Furthermore, only a single-peak fat model, which accounts for about 70% of the total fat protons, was assumed in the current study. Nevertheless, there are two other fat peaks at about -3.8 ppm and 0.6 ppm that may affect the amide and hydroxyl CEST contrast, respectively [149, 150].

This study is the first to quantify in vivo CEST effects in the renal graft tissue on a clinical MRI system. In line with prior research, the highest MTR_{asym} values was obtained at approximately 1 ppm [126, 127], indicating urea as a major contributor to the total CEST effect in the kidney. However, several other kidney metabolites with exchangeable protons including creatinine, creatine, glutamine, glutamate, allanine and allantoin produce measurable CEST effects as well, and might partially conceal the urea

CEST contrast, as shown in the **study 2** [87]. Moreover, strong pH- and concentration-dependence of the CEST effects from these compounds resulted in relatively high standard deviations of the MTR_{asym} values measured here.

Study 3 has several limitations, which are worth-noting. Firstly, the cohort of patients with transplanted kidneys was small and there was no control group. Secondly, although the multi-point Dixon acquisition can provide an embebded B_0 map, an additional WASSR scan was needed to obtain a robust field map in the presence of large B_0-inhomogneity in the lower abdomen. Furthermore, diet and fluid intake of patients were not controlled in the present study, which might be one of the reasons for the high MTR_{asym} variability.

Besides the mutli-point Dixon technique, a new promising method that uses a residual signal at the frequency offset of the direct water saturation to reduce the fat signal-induces artifacts in the in vivo CEST data, has lately been proposed and evaluated in the human breast [148]. However, its potential utility for the application in the human kidney requires evaluation in future studies. Another interesting CEST quantification approach, multi-pool Lorentzian fitting, does not require any fat suppression because it isolates the individual CEST effects originating from different types of functional groups (e.g. OH, NH_2, NH and NOE).

8.4 Conclusion

In **study 3**, an optimized CEST acquisition protocol was combined with a Dixon-based post-processing in order to eliminate the confounding fat signal contribution in the CEST signal. Furthermore, the hydroxyl, amine and amide CEST effects in the renal tissue were quantified by the asymmetry of the magnetization transfer ratio (MTR_{asym}) metric. In line with prior research, the highest renal MTR_{asym} values were measured at about 1 ppm, corresponding to the resonace frequency of urea. At the same time, an overall very low amide CEST effect was observed. Nevertheless, by correcting the fat-induced artifacts using the two-point Dixon-based CEST the specificity of the amide proton transfer (APT) MRI contrast could be slightly enhanced in the renal cortex.

Chapter 9

Technical development: CEST MRI sequence with multi-echo readout

9.1 CEST pulse sequence design

The MRI pulse sequence for CEST imaging has been developed on Siemens 3T MR clinical systems (Magnetom Trio and Magnetom Prisma, Siemens Healthineers, Erlangen, Germany). The Integrated Development Environment for Applications (IDEA) version VB17 and VE11C were used for the the implementation. The C++-based IDEA framework was provided by Siemens [151].

As described in the section 3.2.1, the conventional CEST imaging sequence is composed of a frequency selective saturation module followed by a fast image acquisition sequence. In the following, the implementation of the CEST pulse sequence is outlined.

9.1.1 Saturation module

The saturation section includes a series of Gaussian-shaped or rectangular RF pulses, each followed by a crusher gradient to spoil the residual transverse magnetization. This interleaved approach is required due to limited pulse width and duty-cycle, as well as SAR guidelines in clinical MR scanners [114]. The implemented CEST saturation block can be specified by the parameters given in table 9.1.

Generally, each dynamic measurement corresponds to one offset within a specified range of frequencies from -$\Delta\omega$ to +$\Delta\omega$. For normalization, an unsaturated reference image is acquired at -300 ppm.

9.1.2 Image acquisition

In the current implementation, CEST images are obtained using a fast FLASH readout, as described in the section 2.3. However, several sequence improvements have been made in order to: (i) maximize the CEST contrasts, (ii) increase the acquisition speed, and (iii) enable the multi-echo data collection.

Table 9.1: CEST saturation module parameters.

Parameter	Description
Pulse type	form of a saturation pulse, e.g. Gaussian-shaped, rectangular or spin-lock
No. of pulses, N	number of RF pulses applied during each saturation period
Pulse duration, t_{pd}	duration of a single saturation pulse
Inter-pulse delay, t_{ipd}	delay between two adjacent saturation pulses
RF pulse amplitude, B_1	mean RF amplitude of a saturation pulse
Maximum offset, $\Delta\omega$	positive and negative offset maximum
Sampling strategy	sampling pattern of the offset points, e.g. regular, alternating, from a file, single offset
Recovery time, t_{rec}	delay between the readout and the saturation block

Multi-echo readout

A multi-echo fast FLASH readout permits acquiring a closely-spaced echo train after a single excitation pulse by sequential gradient reversals. In particular, the in-phase and out-of-phase images can be collected at two different TE's in order to enable further Dixon-based analysis. A simplified diagram of a multi-echo FLASH readout is shown in figure 9.1

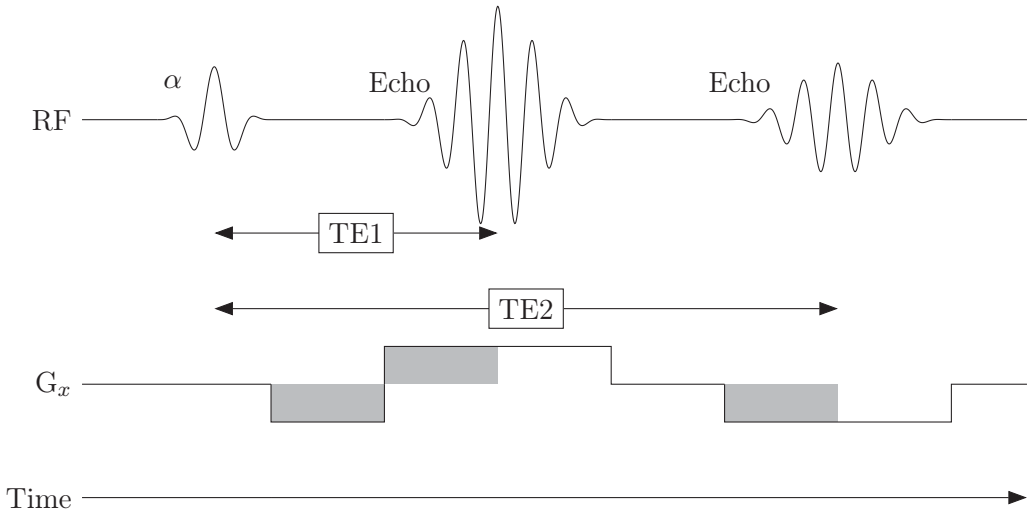

Figure 9.1: Simplified diagram of a FLASH sequence with a multi-echo readout. Multiple gradient echos can be generated after a single RF pulse until the complete transverse magnetization is lost due to T_2^* relaxation.

Centric reordering

To maximize the saturation contrast at the beginning of the readout period, centric k-space reordering can be chosen in phase encoding direction. The center lines of the k-space are then sampled first, and have the lowest signal reduction due to T_2 signal relaxation. The main advantage of the centric approach over the conventional sequential approach is a higher SNR and an improved CEST image contrast owing to the dominant signal in the k-space center [152].

Phase-conjugate symmetry (Partial Fourier)

Phase-conjugate symmetry uses data from the upper half of the sampled k-space to predict the data in the lower half of the k-space. A large benefit of this method is the reduction of the phase-encoding steps, and thus scanning time while preserving spatial resolution [151].

Read-conjugate symmetry (Asymmetric echo)

The so-called fractional echo imaging uses collected data from the right half k-space to estimate the data in the left half. Since only the right half of each echo need to be sampled, shorter TE can be achieved and there are no interferences between the FID generated by the RF pulse and echo signals. The missing section of the echo is reconstructed using a read-conjugate symmetry [153].

Parallel imaging (iPAT)

Integrated Parallel Acquisition Techniques (iPAT) reduce the total scanning time while maintaining the image quality by partially replacing the gradient-encoding steps with spatial information derived from the sensitivity patterns of RF receiver coils [151]. The undersampled k-space raw data were reconstructed using GeneRAlized Partially Parallel Acquisition (GRAPPA) algorithm [154], which is a part of the standard Image Calculation Environment (ICE) provided by Siemens.

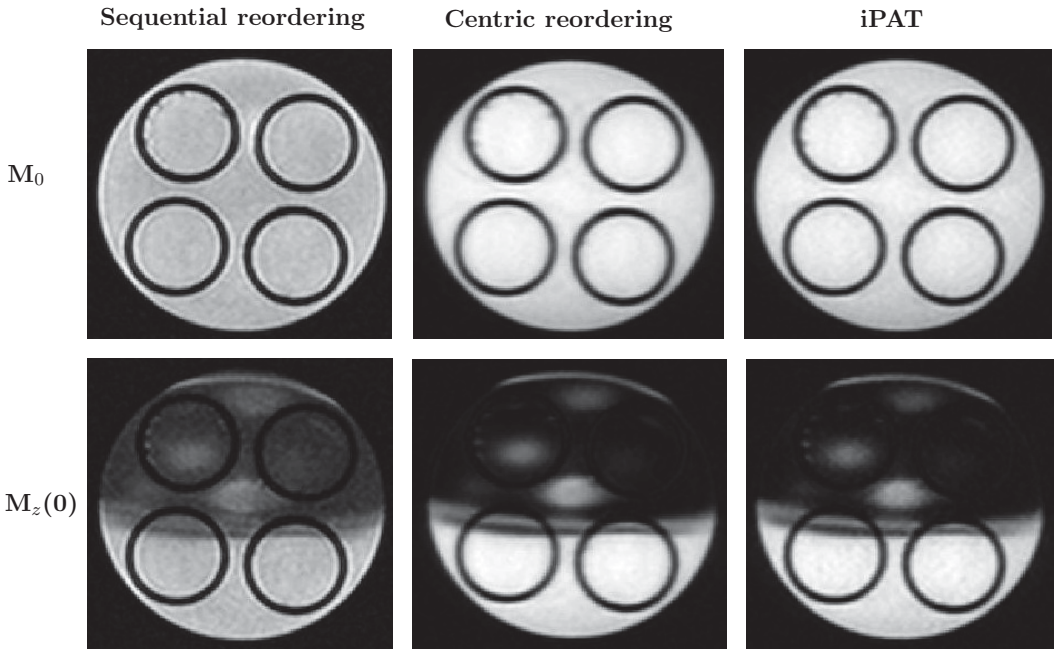

Figure 9.2: The unsaturated M_0 images and $M_z(\Delta\omega)$ images obtained at water resonance frequency in a water phantom using the developed CEST imaging sequence. The use of the centric k-space reordering led to a higher SNR and an improved saturation efficiency compared with the sequential reordering. The application of the iPAT reduced the scan time while maintaining the CEST image quality.

Figure 9.2 displays the unsaturated M_0 and M_z images obtained at water resonance frequency in a water phantom using the developed CEST MRI sequence. The use of centric k-space reordering led to a higher SNR (SNR(M_0) = 49) compared with the conventional sequential reordering (SNR(M_0) = 24). Moreover, an improved saturation efficiency was achieved by acquiring the center lines of the k-space first before collecting the outlying k-space data. The application of the iPAT technique reduced the scan time (from 3 min 14 sec to 3 min 7 sec) while maintaining the quality of the collected CEST images (SNR (M_0, iPAT) = 49).

Chapter 10

General discussion

This PhD thesis aimed at establishing the utility of endogenous chemical exchange saturation transfer MR technique for renal molecular imaging. To achieve a better understanding of the contrast measured by CEST in the kidney, extensive phantom experiments and an in vivo study in patients with renal transplants were conducted. The first study evaluated the applicability of different pulsed irradiation schemes and quantification methods for measuring quantitative CEST parameters on a clinical 3T MRI system. The objective of the second study was to characterize the exchange-related properties of urea amide protons. Moreover, the CEST contrast of several other abundant kidney metabolites and its dependence on pH have been investigated. The third study focused on implementing technical and methodological tools for in vivo CEST imaging in kidney graft recipients.

The simulations and phantom experiments conducted in **study 1** implied that it is generally possible to estimate the quantitative CEST-related parameters on clinical scanners. Nevertheless, the range of validity of different CEST quantification approaches at 3T is narrower than at 7T [97]. This can be explained by the fact that in addition to increased SNR and CEST effects, the chemical shift separation is larger at higher magnetic fields strengths. In fact, the exchange rate must be smaller than the chemical shift difference to water for successful CEST [18]. This might also hamper the detection of compounds containing hydroxyl and amine functional groups with intermediate or fast exchanging protons resonating close to water. Besides the large shift assumption, the derivation of the pulsed z-spectrum model used for the quantification is valid if the following conditions are fulfilled: (i) small CEST pool ($f < 1\%$), (ii) sufficiently long saturation times ($t_{sat} > T_{2w}$), (iii) exchange dynamic is faster than the pulse dynamic ($k_{sw} > 1/t_{pd}$), (iv) exchange dynamic in the inter-pulse delay can be neglected ($k_{sw} < 1/t_{ipd}$), (v) analytical integral of $R_{1\rho}$ over the pulse shape is valid ($\Delta\omega > \omega_1$), and (vi) the width of the irradiation pulse is small with respect to its length ($\sigma\ /t_{pd}$) [97]. On clinical systems these restrictions are met only for the intermediate exchanging protons, e.g guanidinium protons of creatine. However, as shown in a recent study performed in the intervertebral discs (IVDs) in a porcine model, the Ω-plot method can also be applied for determining the exchange rate and labile proton ratio of hydroxyl protons of glycosaminoglycans (GAGs) under physiological conditions at 3T [119]. Indeed, the estimated exchange rates were closely correlated with pH values measured using a tissue pH probe. Nevertheless, the scanning time of 30-40 min for one IVD is not clinically feasible. This long measurement time results from the required multi-B_1 steady-state z-spectral data for the Ω-plot analysis, and the image readout. To accelerate the quantitative CEST (qCEST) data collection, several more advanced acquisition techniques such as echo-planar readout [155], balanced steady-state

free precession (bSSFP) sequences [156], parallel transmission [157], parallel imaging [158] or compressed sensing [159, 160] could be utilized. If the measurement time needs to be reduced even more, the application of the recently revised QUEST/QUESP or Ω-plot methods for the case of nonequilibrium initial magnetization and weak labeling conditions ($\gamma B_1 < k_{sw}$) should be considered [161]. The CEST data analysis using the extended QUEST/QUESP model allows not only a quicker but also a more accurate quantification, especially when estimating faster exchange rates. Nevertheless, the initial magnetization measured before the saturation module needs to be known and taken into account in the analytic solution [161]. Another interesting qCEST approach that enables simultaneous quantification of the exchange rate and volume fraction in a short scan time is based on a novel MRI technique, called magnetic resonance fingerprinting (MRF) method. In the MRF experiments, fingerprints are collected using pseudorandomized acquisition parameters and subsequently matched to a large database of signal trajectories obtained from the Bloch-McConnell simulations for different combinations of quantitative tissue parameters (k_{sw}, f, T_{1w}, T_{2w}) [162–165].

In **study 2** proton exchange-related properties of slow exchanging amide protons of urea have been characterized. Since none of the above mentioned qCEST imaging methods is suitable for accurately quantifying slow chemical exchange, the WEX spectroscopy at ultra-high magnetic field was employed to determine the exchange rate constants and activation energies for the acid- and base-catalyzed proton exchange in urea solution. As a matter of fact, the WEX filter has already been used for studying slow exchange species [53, 69, 132]. In this study, the original WEX II pulse sequence has been slightly modified by replacing the WATERGATE water suppression by the excitation sculpting method. Because of the large width of the urea peak and its nearness to the water resonant frequency, the WATERGATE technique was expected to negatively impact the urea signal due to the lack of selectivity [134]. Although very promising for in vitro applications, the use of the WEX spectroscopy for in vivo studies has been limited owing to its relatively low sensitivity, which makes a detection of low level metabolites difficult. This common limitation of the spectroscopy (MRS)-based methods can be practically overcome by CEST MRI. Even though the amide protons of urea produce a measurable pH- and concentration-dependent CEST effect, determination of its extremely slow exchange rate using CEST is challenging. In the current study, it was possible to estimate the urea exchange rates in a relatively broad range of pH values using the extended steady-state AREX method, which takes into account the magnetization transfer during the inter-pulse delay [117]. Indeed, modeling the bi-exponential dynamics of the water magnetization during the pause between two subsequent saturation pulses is crucial especially if the exchange rate between the solute and water pool is small with respect to the inter-pulse delay, as it is in the case of urea solution. Nevertheless, in the physiologically relevant pH and urea concentration range the urea CEST signal measured at 3T seems to be very low, which limits its potential use for pH imaging in the kidney. As shown in a recent study performed in a mice model at 7T, the urea CEST contrast can be slightly increased by intravenous/intraperitorenal urea injections. Furthermore, the same study showed that it might actually be possible to monitor renal function by measuring the spatially varying urea concentrating capacity of the kidney [166]. While in the inner medulla and papilla an increased urea CEST contrast following an urea infusion was measured, no significant dif-

ferences in urea CEST obtained before and after urea administration were observed in the renal cortex and outer medulla. These findings reflect the urea-handling pattern reported in previous studies [34, 167]. Although the intravenous urea injection might genrally lead to greatly amplified CEST sensitivity, translation of the urea CEST imaging to clinical field strengths remains challenging because of its limited specificity. As shown in **study 2**, there are several others important small kidney metabolites such as creatinine, creatine, glutamine, alanine, allantoin and glutamate that might potentially overlap with the urea CEST signal in vivo, and therefore considerably hamper the absolute urea quantification. In order to better isolate the urea CEST contrast from other metabolites that contribute to the total CEST effect at ca. 1 ppm in the kidney, novel approaches such as variable delay multipulse CEST-MRI (VDMP-CEST), $T_{1\rho}$ imaging or T_2-exchange technique could be employed [166, 168, 169]. Alternatively, the use of a multiple Lorentzian fitting method that allows a characterization of the overlaying effects observed in the in vivo Z-spectrum (see section 3.2.2) should be considered [170]. Despite all the above mentioned limiting factors, urea appears to be promising as an exogenous CEST contrast agent because of its non-toxicity and the kidney's innate ability to concentrate and remove urea from blood.

In order to enable in vivo CEST experiments in the renal tissue, specific methodological and technical tools have been developed in **study 3**. As a result, a clinically applicable CEST framework was created and validated in renal transplant recipients. One of the major challenges for CEST MRI in the kidney is the presence of surrounding adipose tissue, including perirenal and renal sinus fat. As shown in previous CEST studies performed in the human breast, the strong lipid signals lead to the incorrect z-spectrum normalization, and thus to erroneous CEST values measured in the amide frequency range [141, 148]. It has also been shown that z-spectra are strongly dependent on the TE and fat fraction, resulting from the complex interplay between water and fat signals [140]. Hence, for a reliable CEST quantification the fat contribution need to be eliminated from the total MR signal without affecting the water signal. Although there is a number of different fat suppression methods available, e.g. spectral pre-saturation with inversion recovery (SPIR), spectral fat saturation, and short tau inversion recovery (STIR), their potential application with CEST in renal graft is limited. Specifically, the spectral- and excitation selectivity of the preparation pulses can be severely deteriorated by the B_1 inhomogeneity. Furthermore, a combination of the fat-selective- and/or inversion RF pulses with the CEST saturation train pulse may lead to the pulse instability and higher total SAR [141]. To overcome these limitations, the utility of Dixon-based water fat separation for CEST applications has been previously explored [136, 141]. The findings of the present thesis seem to confirm the fat suppression capability of Dixon technique on renal CEST imaging. Alternatively, a novel CEST normalization method which utilizes the residual signal at the spectral position of the direct water saturation, or multiple Lorentzian fitting could be used to correct for fat signal-induced artifacts [148, 170].

In addition to providing an optimized CEST acquisition and post-processing protocol tailored to renal graft applications, **study 3** also quantified CEST effects measured in vivo in the human renal tissue. It can be generally stated that the CEST signals observed in the kidney are mainly produced by metabolites in three tissue components: (i) blood, (ii) cellular and interstitial components, and (iii) urine. In line with a previous study in

mice conducted at 7T, the total CEST effects observed in the kidney were small, broad and coalesced [40]. The highest MTR_{asym} values were obtained in the frequency range between 0.8 and 1.2 ppm. On the basis of findings from **study 1**, it can be speculated that this CEST contrast originates primarily from the amide protons of urea. As suggested in the study cited above, the CEST effect observed at ca. 1.2 ppm might also correspond to the glucose/glycogen hydroxyl groups. However, as shown in **study 2**, their CEST peaks are possibly within the linewidth of the water resonance and their exchange rates are in the fast exchange regime at 3T. Therefore, it is unlikely that these two metabolites contribute to the total CEST effect at about 1 ppm. An important CEST agent, which might actually generate a substantial CEST contrast in the kidney, is blood. A recent study performed on a clinical scanner demonstrated that the MTR_{asym} analysis of blood is a combined result of the hydroxyl, amine, and amide CEST effects as well as upfield asymmetric NOE signals [171]. This observation again underlines one of the major challenges of the endogenous CEST imaging, namely low specificity due to overlapping CEST effects from multiple chemical compounds. A number of recent works have addressed this problem by developing and employing nonradioactive contrast agents as CEST MRI pH sensors [35, 172, 173]. In particular, several animal studies showed that iopamidol can be an useful pH probe for detection of acute kidney injury (AKI) and monitoring chronic kidney disease (CKD) [45, 47, 135]. The promising results obtained in animal models, and the fact that the iopamidol is a FDA-approved contrast agent for use in computed tomography (CT), should facilitate the translation of the iopamidol CEST MRI to patients with a range of renal disorders [47].

Chapter 11

Conclusion

The present dissertation contributes to further development of molecular MRI of the human kidney using CEST imaging. Several most abudnant kidney metabolites containing functional groups with exchangeable protons such as hydroxyl, amine, guanidinium groups has been shown to produce a measurable pH-dependent CEST effect at 3T in the physiological pH range and at in vivo temperature of 37°C. Besides urea, high CEST contrast was obtained in creatinine, creatine, glutamine, alanine, allantoin and glutamate solutions. These results indicate that the quantitative CEST analysis, although possible at 3T, might be hampered by its limited specificity. To further investigate the competing magnetization transfer effects in the renal tissue, an optimized pulsed-CEST imaging sequence combined with a Dixon-based post-processing pipeline for water-fat separation was developed. Using this protocol, the hydroxyl, amine and amide CEST effects could be quantified in vivo by the asymmetry of the magnetization transfer ratio.

The relevance of the findings presented here concerns three aspects. Firstly, the quantitative CEST analysis using pulsed saturation scheme has been proven feasible on a clinical 3T MR scanner. In particular, Ω-plot method combined with a pulsed spin-lock irradiation scheme provided promising results for slow- and intermediate-exchanging amine protons with k_{sw} values between 50 and 530 Hz. Since the exchange rates of labile protons and thus their CEST effects are pH and concentration dependent, the quantitative CEST analysis could theoretically be applied to create spatial maps of extracellular pH and proton volume fractions. Since the body's pH balance is impaired in several renal or pulmonary pathologies, quantitative CEST MRI could be an useful tool to assess the pathological alterations in pH with high spatiotemporal resolution. Nevertheless, the low specificity, relatively long acquisition time and constraints of the pulsed Ω-plot method set limits to the applicability of the qCEST analysis in vivo.

Secondly, to investigate the specificity of the CEST imaging in renal tissue, several major kidney metabolites have been examined in the present work. In particular, the proton exchange-related properties of urea, which is the most abundant urinary solute, have been studied extensively. The in vitro experiments revealed the concentration and pH-dependent CEST contrast of urea, which is both acid- and base- catalyzed. Because urea protons undergo an extremely slow exchange with water protons in neutral solutions, the urea CEST effect was barely measurable even at high urea concentrations. Thus, the applicability of the urCEST for the renal pH mapping is rather limited. On the other hand, it might be possible to monitor renal function by measuring spatially varying urea concentration in the kidney, following urea administration.

Thirdly, methodological and technical tools that enable a straightforward application of endogenous CEST imaging in patients with kidney transplant have been developed. Using the optimized acquisition and post-processing CEST protocol, it was possible to (i) reduce the fat-signal induced artifacts from the z-spectrum, and to (ii) quantify hydroxyl, amine and amide CEST effects in the renal tissue at 3T. The highest CEST contrast was measured at the frequency offset of about 1 ppm, indicating that urea may be the main contributor to the CEST signal in the kidney. In addition to glomerular filtration rate, blood levels of urea and creatinine are considered strong indicators of kidney function as well. The CEST processing framework developed in this thesis could be potentially used to investigate links between these clinical parameters and the CEST MRI contrast in kidney grafts with normal and impaired function. Nevertheless, to gain a better understanding of the functional and molecular processes underlying various renal (graft) diseases, further extensive phantom and animal CEST studies should be performed.

Bibliography

[1] F. Bloch, "Nuclear induction," *Phys. Rev.*, vol. 70, pp. 460–474, 1946.

[2] E. M. Purcell, H. C. Torrey, and R. V. Pound, "Resonance absorption by nuclear magnetic moments in a solid," *Phys. Rev.*, vol. 69, pp. 37–38, 1946.

[3] R. Damadian, M. Goldsmith, and L. Minkoff, "NMR in cancer: XVI. FONAR image of the live human body," *Physiol. Chem. Phys.*, vol. 9, pp. 97–100, 1977.

[4] W. G. Proctor and F. C. Yu, "The dependence of a nuclear magnetic resonance frequency upon chemical compound," *Phys. Rev.*, vol. 77, pp. 717–717, 1950.

[5] J. T. Arnold, S. S. Dharmatti, and M. E. Packard, "Chemical effects on nuclear induction signals from organic compounds," *The Journal of Chemical Physics*, vol. 19, no. 4, pp. 507–507, 1951.

[6] R. Damadian, K. Zaner, D. Hor, T. DiMaio, L. Minkoff, and M. Goldsmith, "Nuclear magnetic resonance as a new tool in cancer research: Human tumors by NMR," *Annals of the New York Academy of Sciences*, vol. 222, no. 1, pp. 1048–1076, 1973.

[7] P. C. Lauterbur, "Image formation by induced local interactions: Examples employing nuclear magnetic resonance," *The Journal of Chemical Physics*, vol. 242, p. 190, 1973.

[8] P. Mansfield and P. K. Grannell, "NMR 'diffraction' in solids?" *Journal of Physics C: Solid State Physics*, vol. 6, no. 22, p. L422, 1973.

[9] P. Mansfield, "Multi-planar image formation using NMR spin echoes," *Journal of Physics C: Solid State Physics*, vol. 10, no. 3, p. L55, 1977.

[10] NobelPrize.org. (2003) The nobel prize in physiology or medicine 2003. Nobel Media AB 2020.

[11] M. E. Moseley, Y. Cohen, J. Mintorovitch, L. Chileuitt, H. Shimizu, J. Kucharczyk, M. F. Wendland, and P. R. Weinstein, "Early detection of regional cerebral ischemia in cats: Comparison of diffusion- and T2-weighted MRI and spectroscopy," *Magnetic Resonance in Medicine*, vol. 14, no. 2, pp. 330–346, 1990.

[12] S. Mori and P. B. Barker, "Diffusion magnetic resonance imaging: Its principle and applications," *The Anatomical Record*, vol. 257, no. 3, pp. 102–109, 1999.

[13] Y. K. Mariappan, K. J. Glaser, and R. L. Ehman, "Magnetic resonance elastography: A review," *Clinical Anatomy*, vol. 23, no. 5, pp. 497–511, 2010.

[14] D. C. Alsop and J. A. Detre, "Multisection cerebral blood flow MR imaging with continuous arterial spin labeling." *Radiology*, vol. 208, no. 2, pp. 410–416, 1998.

[15] N. K. Logothetis and J. Pfeuffer, "On the nature of the BOLD fMRI contrast mechanism," *Magnetic Resonance Imaging*, vol. 22, no. 10, pp. 1517 – 1531, 2004.

[16] S. Lang, N. Duncan, and G. Northoff, "Resting-state functional magnetic resonance imaging:review of neurosurgical applications," *Neurosurgery*, vol. 74, no. 5, pp. 453–465, 2014.

[17] K. Ward, A. Aletras, and R. Balaban, "A new class of contrast agents for MRI based on proton chemical exchange dependent saturation transfer (CEST)," *Journal of Magnetic Resonance*, vol. 143, no. 1, pp. 79 – 87, 2000.

[18] B. Wu, G. Warnock, M. Zaiss, C. Lin, M. Chen, Z. Zhou, L. Mu, D. Nanz, R. Tuura, and G. Delso, "An overview of CEST MRI for non-MR physicists," *EJNMMI Physics*, vol. 3, no. 1, p. 19, 2016.

[19] P. C. M. van Zijl and N. N. Yadav, "Chemical exchange saturation transfer (CEST): What is in a name and what isn't?" *Magnetic Resonance in Medicine*, vol. 65, no. 4, pp. 927–948, 2011.

[20] G. Liu, X. Song, K. W. Y. Chan, and M. T. McMahon, "Nuts and bolts of chemical exchange saturation transfer MRI," *NMR in Biomedicine*, vol. 26, no. 7, pp. 810–828, 2013.

[21] E. Vinogradov, A. D. Sherry, and R. E. Lenkinski, "CEST: From basic principles to applications, challenges and opportunities," *Journal of Magnetic Resonance*, vol. 229, pp. 155 – 172, 2013.

[22] M. Haris, R. P. R. Nanga, A. Singh, K. Cai, F. Kogan, H. Hariharan, and R. Reddy, "Exchange rates of creatine kinase metabolites: feasibility of imaging creatine by chemical exchange saturation transfer MRI," *NMR in Biomedicine*, vol. 25, no. 11, pp. 1305–1309, 2012.

[23] F. Kogan, M. Haris, C. Debrosse, A. Singh, R. P. Nanga, K. Cai, H. Hariharan, and R. Reddy, "In vivo chemical exchange saturation transfer imaging of creatine (CrCEST) in skeletal muscle at 3T," *Journal of Magnetic Resonance Imaging*, vol. 40, no. 3, pp. 596–602, 2014.

[24] K. Cai, A. Singh, H. Poptani, W. Li, S. Yang, Y. Lu, H. Hariharan, X. J. Zhou, and R. Reddy, "CEST signal at 2 ppm from Z-spectral fitting correlates with creatine distribution in brain tumor," *NMR in Biomedicine*, vol. 28, no. 1, pp. 1–8, 2015.

[25] Z. Zu, J. Spear, H. Li, J. Xu, and J. C. Gore, "Measurement of regional cerebral glucose uptake by magnetic resonance spin-lock imaging," *Magnetic Resonance Imaging*, vol. 32, no. 9, pp. 1078 – 1084, 2014.

[26] F. A. Nasrallah, G. Pagés, P. W. Kuchel, X. Golay, and K.-H. Chuang, "Imaging brain deoxyglucose uptake and metabolism by glucoCEST MRI," *Journal of Cerebral Blood Flow & Metabolism*, vol. 33, no. 8, pp. 1270–1278, 2013.

[27] A. A. Sehgal, Y. Li, B. Lal, N. N. Yadav, X. Xu, J. Xu, J. Laterra, and P. C. van Zijl, "CEST MRI of 3-O-methyl-D-glucose uptake and accumulation in brain tumors," *Magnetic Resonance in Medicine*, vol. 81, no. 3, pp. 1993–2000, 2019.

[28] K. Cai, A. Singh, D. R. Roalf, R. P. R. Nanga, M. Haris, H. Hariharan, R. Gur, and R. Reddy, "Mapping glutamate in subcortical brain structures using high-resolution GluCEST MRI," *NMR in Biomedicine*, vol. 26, no. 10, pp. 1278–1284, 2013.

[29] F. Kogan, A. Singh, C. Debrosse, M. Haris, K. Cai, R. P. Nanga, M. Elliott, H. Hariharan, and R. Reddy, "Imaging of glutamate in the spinal cord using GluCEST," *NeuroImage*, vol. 77, pp. 262 – 267, 2013.

[30] J. Pepin, L. Francelle, M.-A. C. de Sauvage, L. de Longprez, P. Gipchtein, K. Cambon, J. Valette, E. Brouillet, and J. Flament, "In vivo imaging of brain glutamate defects in a knock-in mouse model of Huntington's disease," *NeuroImage*, vol. 139, pp. 53 – 64, 2016.

[31] M. Deng, S.-Z. Chen, J. Yuan, Q. Chan, J. Zhou, and Y.-X. J. Wáng, "Chemical exchange saturation transfer (CEST) MR technique for liver imaging at 3.0 tesla: an evaluation of different offset number and an after-meal and over-night-fast comparison," *Molecular Imaging and Biology*, vol. 18, no. 2, pp. 274–282, 2016.

[32] M. Haris, K. Cai, A. Singh, H. Hariharan, and R. Reddy, "In vivo mapping of brain myo-inositol," *NeuroImage*, vol. 54, no. 3, pp. 2079 – 2085, 2011.

[33] V. Guivel-Scharen, T. Sinnwell, S. Wolff, and R. Balaban, "Detection of proton chemical exchange between metabolites and water in biological tissues," *Journal of Magnetic Resonance*, vol. 133, no. 1, pp. 36 – 45, 1998.

[34] A. P. Dagher, A. Aletras, P. Choyke, and R. S. Balaban, "Imaging of urea using chemical exchange-dependent saturation transfer at 1.5T," *Journal of Magnetic Resonance Imaging*, vol. 12, no. 5, pp. 745–748, 2000.

[35] D. Delli Castelli, E. Terreno, and S. Aime, "YbIII-HPDO3A: A dual pH- and temperature-responsive CEST agent," *Angewandte Chemie International Edition*, vol. 50, no. 8, pp. 1798–1800, 2011.

[36] J. M. Goldenberg and M. D. Pagel, "Assessments of tumor metabolism with CEST MRI," *NMR in Biomedicine*, vol. 32, no. 10, 2018.

[37] D. L. Longo, A. Bartoli, L. Consolino, P. Bardini, F. Arena, M. Schwaiger, and S. Aime, "In vivo imaging of tumor metabolism and acidosis by combining PET and MRI-CEST pH imaging," *Cancer Research*, vol. 76, no. 22, pp. 6463–6470, 2016.

[38] M. Wang, X. Hong, C.-F. Chang, Q. Li, B. Ma, H. Zhang, S. Xiang, H.-Y. Heo, Y. Zhang, D.-H. Lee, S. Jiang, R. Leigh, R. C. Koehler, P. C. M. van Zijl, J. Wang, and J. Zhou, "Simultaneous detection and separation of hyperacute intracerebral hemorrhage and cerebral ischemia using amide proton transfer MRI," *Magnetic Resonance in Medicine*, vol. 74, no. 1, pp. 42–50, 2015.

[39] W. Ling, R. R. Regatte, G. Navon, and A. Jerschow, "Assessment of glycosaminoglycan concentration in vivo by chemical exchange-dependent saturation transfer (gagCEST)," *Proceedings of the National Academy of Sciences*, vol. 105, no. 7, pp. 2266–2270, 2008.

[40] F. Wang, D. Kopylov, Z. Zu, K. Takahashi, S. Wang, C. C. Quarles, J. C. Gore, R. C. Harris, and T. Takahashi, "Mapping murine diabetic kidney disease using chemical exchange saturation transfer MRI," *Magnetic Resonance in Medicine*, vol. 76, no. 5, pp. 1531–1541, 2016.

[41] F. Wang, K. Takahashi, H. Li, Z. Zu, K. Li, J. Xu, R. C. Harris, T. Takahashi, and J. C. Gore, "Assessment of unilateral ureter obstruction with multi-parametric MRI," *Magnetic Resonance in Medicine*, vol. 79, no. 4, pp. 2216–2227, 2018.

[42] A. Li, C. Xu, P. Liang, Y. Hu, Y. Shen, D. Hu, Z. Li, and I. R. Kamel, "Role of chemical exchange saturation transfer and magnetization transfer MRI in detecting metabolic and structural changes of renal fibrosis in an animal model at 3T," *Korean J Radiol*, vol. 21, no. 5, pp. 588–597, 2020.

[43] J. Liu, Z. Han, G. Chen, Y. Li, J. Zhang, J. Xu, P. C. van Zijl, S. Zhang, and G. Liu, "CEST MRI of sepsis-induced acute kidney injury," *NMR in Biomedicine*, vol. 31, no. 8, p. e3942, 2018.

[44] D. Kentrup, P. Bovenkamp, A. Busch, K. Schuette-Nuetgen, H. Pawelski, H. Pavenstädt, E. Schlatter, K.-H. Herrmann, J. R. Reichenbach, B. Löffler, B. Heitplatz, V. V. Marck, N. N. Yadav, G. Liu, P. C. van Zijl, S. Reuter, and V. Hoerr, "GlucoCEST magnetic resonance imaging in vivo may be diagnostic of acute renal allograft rejection," *Kidney International*, vol. 92, no. 3, pp. 757 – 764, 2017.

[45] D. L. Longo, A. Busato, S. Lanzardo, F. Antico, and S. Aime, "Imaging the pH evolution of an acute kidney injury model by means of iopamidol, a MRI-CEST pH-responsive contrast agent," *Magnetic Resonance in Medicine*, vol. 70, no. 3, pp. 859–864, 2013.

[46] D. L. Longo, J. C. Cutrin, F. Michelotti, P. Irrera, and S. Aime, "Noninvasive evaluation of renal pH homeostasis after ischemia reperfusion injury by CEST-MRI," *NMR in Biomedicine*, vol. 30, no. 7, p. e3720, 2017.

[47] K. Pavuluri, I. Manoli, A. Pass, Y. Li, H. J. Vernon, C. P. Venditti, and M. T. McMahon, "Noninvasive monitoring of chronic kidney disease using pH and perfusion imaging," *Science Advances*, vol. 5, no. 8, 2019.

[48] G. J. Becker and T. D. Hewitson, "Animal models of chronic kidney disease: useful but not perfect," *Nephrology Dialysis Transplantation*, vol. 28, no. 10, pp. 2432–2438, 2013.

[49] Y. Tee, A. Khrapitchev, N. Sibson, S. Payne, and M. Chappell, "Evaluating the use of a continuous approximation for model-based quantification of pulsed chemical exchange saturation transfer (CEST)," *Journal of Magnetic Resonance*, vol. 222, pp. 88 – 95, 2012.

[50] P. Z. Sun, T. Benner, A. Kumar, and A. G. Sorensen, "Investigation of optimizing and translating pH-sensitive pulsed-chemical exchange saturation transfer (CEST) imaging to a 3T clinical scanner," *Magnetic Resonance in Medicine*, vol. 60, no. 4, pp. 834–841, 2008.

[51] W. Laskey, P. Aspelin, C. Davidson, M. Rudnick, P. Aubry, S. Kumar, F. Gietzen, and M. Wiemer, "Nephrotoxicity of iodixanol versus iopamidol in patients with chronic kidney disease and diabetes mellitus undergoing coronary angiographic procedures," *American Heart Journal*, vol. 158, no. 5, pp. 822 – 828.e3, 2009.

[52] B. J. Barrett, R. W. Katzberg, H. S. Thomsen, N. Chen, D. Sahani, G. Soulez, J. P. Heiken, L. Lepanto, Z.-h. Ni, and R. Nelson, "Contrast-induced nephropathy in patients with chronic kidney disease undergoing computed tomography: A double-blind comparison of iodixanol and iopamidol," *Investigative Radiology*, vol. 41, no. 11, pp. 815–821, 2006.

[53] S. Mori, C. Abeygunawardana, P. Van Zijl, and J. Berg, "Water exchange filter with improved sensitivity (WEX II) to study solvent-exchangeable protons. application to the consensus zinc finger peptide CP-1," *Journal of Magnetic Resonance - Series B*, vol. 110, no. 1, pp. 96–101, 1996.

[54] R. A. de Graaf, *In Vivo NMR Spectroscopy: Principles and Techniques*, 2nd ed. Wiley-Interscience, 2007.

[55] C. P. Slichter, *Principles of Magnetic Resonance*, 3rd ed. Springer, 1990.

[56] D. Canet, *Nuclear Magnetic Resonance: Concepts and Methods*, 1st ed. John Wiley & Sons, 1996.

[57] R. Kimmich, *NMR-Tomographie, Diffusometry, Relaxometry*, 1st ed. Springer, 1997.

[58] G. J. Stanisz, E. E. Odrobina, J. Pun, M. Escaravage, S. J. Graham, M. J. Bronskill, and R. M. Henkelman, "T1, T2 relaxation and magnetization transfer in tissue at 3T," *Magnetic Resonance in Medicine*, vol. 54, no. 3, pp. 507–512, 2005.

[59] V. I. Chiznik, Y. S. Chernyshev, A. V. Donets, V. V. Frolov, A. V. Komolkin, and M. G. Shelyapina, *Magentic Resonance and Its Applications*. Springer, 2014.

[60] M. A. Brown and R. C. Semelka, *MRI: Basic Principles and Applications*, 4th ed. John Wiley & Sons, 2010.

[61] A. Haase, J. Frahm, D. Matthaei, W. Hanicke, and K.-D. Merboldt, "FLASH imaging. rapid NMR imaging using low flip-angle pulses," *Journal of Magnetic Resonance (1969)*, vol. 67, no. 2, pp. 258–266, 1986.

[62] E. J. Walsh, "Biochemistry (Garrett, Reginald H.; Grisham, Charles M.)," *Journal of Chemical Education*, vol. 74, no. 2, p. 189, 1997.

[63] W. T. Dixon, "Simple proton spectroscopic imaging." *Radiology*, vol. 153, no. 1, pp. 189–194, 1984.

[64] P. C. van Zijl, W. W. Lam, J. Xu, L. Knutsson, and G. J. Stanisz, "Magnetization transfer contrast and chemical exchange saturation transfer MRI. features and analysis of the field-dependent saturation spectrum," *NeuroImage*, vol. 168, pp. 222 – 241, 2018.

[65] I. Solomon, "Relaxation processes in a system of two spins," *Phys. Rev.*, vol. 99, pp. 559–565, 1955.

[66] A. Berger, A. Loewenstein, and S. Meiboom, "Nuclear Magnetic Resonance Study of the Protolysis and Ionization of N-Methylacetamide1," *Journal of the American Chemical Society*, vol. 81, no. 1, pp. 62–67, 1959.

[67] I. M. Klotz and D. L. Hunston, "Proton exchange in aqueous urea solutions," *The Journal of Physical Chemistry*, vol. 75, no. 14, pp. 2123–2127, 1971.

[68] H. W. Foote, "Elements of Physical Chemistry," *Science*, 1907.

[69] S. Goerke, M. Zaiss, and P. Bachert, "Characterization of creatine guanidinium proton exchange by water-exchange (WEX) spectroscopy for absolute-pH CEST imaging in vitro," *NMR in Biomedicine*, vol. 27, no. 5, pp. 507–518, 2014.

[70] Y. Bai, J. S. Milne, L. Mayne, and S. W. Englander, "Primary structure effects on peptide group hydrogen exchange," *Proteins: Structure, Function, and Bioinformatics*, vol. 17, no. 1, pp. 75–86, 1993.

[71] S. Goerke, M. Zaiss, and P. Bachert, "Characterization of creatine guanidinium proton exchange by water-exchange (WEX) spectroscopy for absolute-pH CEST imaging in vitro," *NMR in Biomedicine*, vol. 27, no. 5, pp. 507–518, 2014.

[72] S. Forsén and R. A. Hoffman, "Study of moderately rapid chemical exchange reactions by means of nuclear magnetic double resonance," *The Journal of Chemical Physics*, vol. 39, no. 11, pp. 2892–2901, 1963.

[73] R. M. Henkelman, X. Huang, Q.-S. Xiang, G. J. Stanisz, S. D. Swanson, and M. J. Bronskill, "Quantitative interpretation of magnetization transfer," *Magnetic Resonance in Medicine*, vol. 29, no. 6, pp. 759–766, 1993.

[74] M. T. McMahon, A. A. Gilad, J. Zhou, P. Z. Sun, J. W. M. Bulte, and P. C. M. van Zijl, "Quantifying exchange rates in chemical exchange saturation transfer agents using the saturation time and saturation power dependencies of the magnetization transfer effect on the magnetic resonance imaging signal (QUEST and QUESP): pH calibration for poly-l-lysine and a starburst dendrimer," *Magnetic Resonance in Medicine*, vol. 55, no. 4, pp. 836–847, 2006.

[75] O. Trott and A. G. Palmer, "R1ρ relaxation outside of the fast-exchange limit," *Journal of Magnetic Resonance*, vol. 154, no. 1, pp. 157 – 160, 2002.

[76] M. Zaiss and P. Bachert, "Exchange-dependent relaxation in the rotating frame for slow and intermediate exchange – modeling off-resonant spin-lock and chemical exchange saturation transfer," *NMR in Biomedicine*, vol. 26, no. 5, pp. 507–518, 2013.

[77] Philips.com. (2019) Philips APT scheme.

[78] M. Zaiss and P. Bachert, "Chemical exchange saturation transfer (CEST) and MRZ-spectroscopyin vivo: a review of theoretical approaches and methods," *Physics in Medicine and Biology*, vol. 58, no. 22, pp. R221–R269, 2013.

[79] C. Morrison, G. Stanisz, and R. Henkelman, "Modeling magnetization transfer for biological-like systems using a semi-solid pool with a super-lorentzian lineshape and dipolar reservoir," *Journal of Magnetic Resonance, Series B*, vol. 108, no. 2, pp. 103 – 113, 1995.

[80] J. Zhou, J.-F. Payen, D. A. Wilson, R. J. Traystman, and P. C. M. van Zijl, "Using the amide proton signals of intracellular proteins and peptides to detect pH effects in MRI," *Nature Medicine*, vol. 9, pp. 1085 EP –, 2003.

[81] J. Zhou, E. Tryggestad, Z. Wen, B. Lal, T. Zhou, R. Grossman, S. Wang, K. Yan, D.-X. Fu, E. Ford, B. Tyler, J. Blakeley, J. Laterra, and P. C. M. van Zijl, "Differentiation between glioma and radiation necrosis using molecular magnetic resonance imaging of endogenous proteins and peptides," *Nature Medicine*, vol. 17, pp. 130 EP –, 2010.

[82] J. Zhou, E. Tryggestad, Z. Wen, B. Lal, T. Zhou, R. Grossman, S. Wang, K. Yan, D.-X. Fu, E. Ford, B. Tyler, J. Blakeley, J. Laterra, and P. C. M. van Zijl, "Differentiation between glioma and radiation necrosis using molecular magnetic resonance imaging of endogenous proteins and peptides," *Nat Med*, vol. 17, no. 1, pp. 130–134, 2011.

[83] X. Zhao, Z. Wen, G. Zhang, F. Huang, S. Lu, X. Wang, S. Hu, M. Chen, and J. Zhou, "Three-dimensional turbo-spin-echo amide proton transfer mr imaging at 3-tesla and its application to high-grade human brain tumors," *Mol Imaging Biol*, vol. 15, no. 1, pp. 114–122, 2013.

[84] O. Togao, T. Yoshiura, J. Keupp, A. Hiwatashi, K. Yamashita, K. Kikuchi, Y. Suzuki, S. O. Suzuki, T. Iwaki, N. Hata, M. Mizoguchi, K. Yoshimoto, K. Sagiyama, M. Takahashi, and H. Honda, "Amide proton transfer imaging of adult diffuse gliomas: correlation with histopathological grades," *Neuro Oncol*, vol. 16, no. 3, pp. 441–448, 2014.

[85] X.-Y. Zhang, F. Wang, A. Afzal, J. Xu, J. C. Gore, D. F. Gochberg, and Z. Zu, "A new noe-mediated mt signal at around -1.6ppm for detecting ischemic stroke in rat brain," *Magnetic Resonance Imaging*, vol. 34, no. 8, pp. 1100 – 1106, 2016.

[86] P. A. Bottomley and J. R. Griffiths, *Handbook of Magnetic Resonance Spectroscopy In Vivo: MRS Theory, Practice and Applications*. Wiley, 2016.

[87] J. Stabinska, P. Neudecker, A. Ljimani, H.-J. Wittsack, R. S. Lanzman, and A. Müller-Lutz, "Proton exchange in aqueous urea solutions measured by water-exchange (WEX) NMR spectroscopy and chemical exchange saturation transfer (CEST) imaging in vitro," *Magnetic Resonance in Medicine*, vol. 82, no. 3, pp. 935–947, 2019.

[88] B. P. Wiebenga-Sanford, J. DiVerdi, C. D. Rithner, and N. E. Levinger, "Nanoconfinement's dramatic impact on proton exchange between glucose and water," *The Journal of Physical Chemistry Letters*, vol. 7, no. 22, pp. 4597–4601, 2016.

[89] J.-S. Lee, D. Xia, A. Jerschow, and R. R. Regatte, "In vitro study of endogenous CEST agents at 3T and 7T," *Contrast Media & Molecular Imaging*, vol. 11, no. 1, pp. 4–14, 2015.

[90] E. Liepinsh and G. Otting, "Proton exchange rates from amino acid side chains—implications for image contrast," *Magnetic Resonance in Medicine*, vol. 35, no. 1, pp. 30–42, 2018.

[91] F. C. Wermter, C. Bock, and W. Dreher, "Investigating GluCEST and its specificity for pH mapping at low temperatures," *NMR in Biomedicine*, vol. 28, no. 11, pp. 1507–1517, 2015.

[92] J. Stabinska, T. Cronenberg, H.-J. Wittsack, R. S. Lanzman, and A. Müller-Lutz, "Quantitative pulsed CEST-MRI at a clinical 3T MRI system," *Magnetic Resonance Materials in Physics, Biology and Medicine*, vol. 30, no. 5, pp. 505–516, 2017.

[93] O. Trott and A. G. Palmer III, "Theoretical study of R1ρ rotating-frame and R2 free-precession relaxation in the presence of n-site chemical exchange," *Journal of Magnetic Resonance*, vol. 170, no. 1, pp. 104 – 112, 2004.

[94] M. Woods, D. E. Woessner, and A. D. Sherry, "Paramagnetic lanthanide complexes as paraCEST agents for medical imaging," *Chem Soc Rev*, vol. 35, no. 6, pp. 500–511, 2006.

[95] M. Basharat, N. M. deSouza, H. G. Parkes, and G. S. Payne, "Determining the chemical exchange saturation transfer (CEST) behavior of citrate and spermine under in vivo conditions," *Magn Reson Med*, vol. 76, no. 3, pp. 742–746, 2016.

[96] M. Zaiss, J. Xu, S. Goerke, I. S. Khan, R. J. Singer, J. C. Gore, D. F. Gochberg, and P. Bachert, "Inverse Z-spectrum analysis for spillover-, MT-, and T1-corrected steady-state pulsed CEST-MRI – application to pH-weighted MRI of acute stroke," *NMR in Biomedicine*, vol. 27, no. 3, pp. 240–252, 2014.

[97] J.-E. Meissner, S. Goerke, E. Rerich, K. D. Klika, A. Radbruch, M. E. Ladd, P. Bachert, and M. Zaiss, "Quantitative pulsed CEST-MRI using Ω-plots," *NMR in Biomedicine*, vol. 28, no. 10, pp. 1196–1208, 2015.

[98] W. T. Dixon, J. Ren, A. J. M. Lubag, J. Ratnakar, E. Vinogradov, I. Hancu, R. E. Lenkinski, and A. D. Sherry, "A concentration-independent method to measure exchange rates in paraCEST agents," *Magnetic Resonance in Medicine*, vol. 63, no. 3, pp. 625–632, 2010.

[99] P. Z. Sun, "Simplified quantification of labile proton concentration-weighted chemical exchange rate (k(ws)) with RF saturation time dependent ratiometric analysis (QUESTRA): normalization of relaxation and RF irradiation spillover effects for

improved quantitative chemical exchange saturation transfer (CEST) MRI," *Magn Reson Med*, vol. 67, no. 4, pp. 936–942, 2012.

[100] S. Mori, M. O. Johnson, J. M. Berg, and P. C. M. van Zijl, "Water exchange filter (WEX filter) for nuclear magnetic resonance studies of macromolecules," *Journal of the American Chemical Society*, vol. 116, no. 26, pp. 11 982–11 984, 1994.

[101] M. Piotto, V. Saudek, and V. Sklenář, "Gradient-tailored excitation for single-quantum NMR spectroscopy of aqueous solutions," *Journal of Biomolecular NMR*, vol. 2, no. 6, pp. 661–665, 1992.

[102] C. Porth and G. Matfin, *Pathophysiology: Concepts of Altered Health States*. Wolters Kluwer Health/Lippincott Williams & Wilkins, 2009.

[103] B. M. Koeppen and B. A. Stanton, *Renal Physiology*, 5th ed. Mosby, 2013.

[104] R. Droual. (2007) Frontal section of left kidney.

[105] E. C. Amerman, *Human Anatomy & Physiology*, 1st ed. Pearson, 2015.

[106] Ivyrose.co.uk. (2007) Simple diagram of a kidney nephron.

[107] Renal.org. (2020) About eGFR.

[108] P. Sekula, O.-N. Goek, L. Quaye, C. Barrios, A. S. Levey, W. Römisch-Margl, C. Menni, I. Yet, C. Gieger, L. A. Inker, J. Adamski, W. Gronwald, T. Illig, K. Dettmer, J. Krumsiek, P. J. Oefner, A. M. Valdes, C. Meisinger, J. Coresh, T. D. Spector, R. P. Mohney, K. Suhre, G. Kastenmüller, and A. Köttgen, "A metabolome-wide association study of kidney function and disease in the general population," *Journal of the American Society of Nephrology*, vol. 27, no. 4, pp. 1175–1188, 2016.

[109] S. Bouatra, F. Aziat, R. Mandal, A. C. Guo, M. R. Wilson, C. Knox, T. C. Bjorndahl, R. Krishnamurthy, F. Saleem, P. Liu, Z. T. Dame, J. Poelzer, J. Huynh, F. S. Yallou, N. Psychogios, E. Dong, R. Bogumil, C. Roehring, and D. S. Wishart, "The Human Urine Metabolome," *PLoS ONE*, vol. 8, no. 9, p. e73076, 2013.

[110] N. Serkova, T. Florian Fuller, J. Klawitter, C. E. Freise, and C. U. Niemann, "1H-NMR–based metabolic signatures of mild and severe ischemia/reperfusion injury in rat kidney transplants," *Kidney International*, vol. 67, no. 3, pp. 1142–1151, 2005.

[111] V. Thongboonkerd, *Proteomics in Nephrology - Towards Clinical Applications*. Karger, S, 2008.

[112] C. Barrios, T. D. Spector, and C. Menni, "Blood, urine and faecal metabolite profiles in the study of adult renal disease," *Archives of Biochemistry and Biophysics*, vol. 589, pp. 81 – 92, 2016.

[113] R. Bassi, M. A. Niewczas, L. Biancone, S. Bussolino, S. Merugumala, S. Tezza, F. D'Addio, M. Ben Nasr, A. Valderrama-Vasquez, V. Usuelli, V. De Zan, B. El Essawy, M. Venturini, A. Secchi, F. De Cobelli, A. Lin, A. Chandraker, and P. Fiorina, "Metabolomic profiling in individuals with a failing kidney allograft," *PloS one*, vol. 12, no. 1, pp. e0 169 077–e0 169 077, 2017.

[114] B. Schmitt, M. Zaiß, J. Zhou, and P. Bachert, "Optimization of pulse train presaturation for CEST imaging in clinical scanners," *Magnetic Resonance in Medicine*, vol. 65, no. 6, pp. 1620–1629, 2011.

[115] K. Murase and N. Tanki, "Numerical solutions to the time-dependent bloch equations revisited," *Magnetic Resonance Imaging*, vol. 29, no. 1, pp. 126 – 131, 2011.

[116] M. Kim, J. Gillen, B. A. Landman, J. Zhou, and P. C. van Zijl, "Water saturation shift referencing (WASSR) for chemical exchange saturation transfer (CEST) experiments," *Magnetic Resonance in Medicine*, vol. 61, no. 6, pp. 1441–1450, 2009.

[117] V. Roeloffs, C. Meyer, P. Bachert, and M. Zaiss, "Towards quantification of pulsed spinlock and CEST at clinical MR scanners: an analytical interleaved saturation–relaxation (ISAR) approach," *NMR in Biomedicine*, vol. 28, no. 1, pp. 40–53, 2014.

[118] P. Z. Sun, E. Wang, and J. S. Cheung, "Imaging acute ischemic tissue acidosis with pH-sensitive endogenous amide proton transfer (APT) MRI–correction of tissue relaxation and concomitant RF irradiation effects toward mapping quantitative cerebral tissue pH," *NeuroImage*, vol. 60, no. 1, pp. 1–6, 2012.

[119] Z. Zhou, M. Bez, W. Tawackoli, J. Giaconi, D. Sheyn, S. de Mel, M. M. Maya, B. D. Pressman, Z. Gazit, G. Pelled, D. Gazit, and D. Li, "Quantitative chemical exchange saturation transfer MRI of intervertebral disc in a porcine model," *Magnetic Resonance in Medicine*, vol. 76, no. 6, pp. 1677–1683, 2016.

[120] H.-Y. Heo, Y. Zhang, D.-H. Lee, S. Jiang, X. Zhao, and J. Zhou, "Accelerating chemical exchange saturation transfer (CEST) MRI by combining compressed sensing and sensitivity encoding techniques," *Magnetic resonance in Medicine*, vol. 77, no. 2, pp. 779–786, 2017.

[121] B. J. Bennion and V. Daggett, "The molecular basis for the chemical denaturation of proteins by urea." *Proceedings of the National Academy of Sciences of the United States of America*, vol. 100, no. 9, pp. 5142–7, 2003.

[122] D. E. Atkinson and E. Bourke, "The role of ureagenesis in pH homeostasis," *Trends in Biochemical Sciences*, vol. 9, no. 7, pp. 297–300, 1984.

[123] N. Baum, C. C. Dichoso, and C. Carlton, "Blood urea nitrogen and serum creatinine: Physiology and interpretations," *Urology*, vol. 5, no. 5, pp. 583–588, 1975.

[124] J. Kim, Y. Wu, Y. Guo, H. Zheng, and P. Z. Sun, "A review of optimization and quantification techniques for chemical exchange saturation transfer MRI toward sensitive in vivo imaging," *Contrast Media & Molecular Imaging*, vol. 10, no. 3, pp. 163–178, 2015.

[125] V. Guivel-Scharen, T. Sinnwell, S. Wolff, and R. Balaban, "Detection of Proton Chemical Exchange between Metabolites and Water in Biological Tissues," *Journal of Magnetic Resonance*, vol. 133, no. 1, pp. 36–45, 1998.

[126] A. P. Dagher, A. Aletras, P. Choyke, and R. S. Balaban, "Imaging of urea using chemical exchange-dependent saturation transfer at 1.5T," *Journal of Magnetic Resonance Imaging*, vol. 12, no. 5, pp. 745–748, 2000.

[127] E. Vinogradov, Z. Liu, A. Madhuranthakarn, A. Hajibeigi, A. Jump, I. Pedrosa, O. W. Moe, and R. E. Lenkinski, "Endogenous urea CEST (urCEST) for MRI monitoring of kidney function," in *Proceedings of the International Society for Magnetic Resonance in Medicine*, 2015.

[128] F. Delaglio, S. Grzesiek, G. Vuister, G. Zhu, J. Pfeifer, and A. Bax, "NMRPipe: A multidimensional spectral processing system based on UNIX pipes," *Journal of Biomolecular NMR*, vol. 6, pp. 277–293, 1995.

[129] R. L. Vold, E. S. Daniel, and S. O. Chan, "Magnetic resonance measurements of proton exchange in aqueous urea," *Journal of the American Chemical Society*, vol. 92, no. 23, pp. 6771–6776, 1970.

[130] I. Yavari and J. D. Roberts, "Nitrogen-15 nuclear magnetic resonance spectroscopy. NH proton exchange reactions of urea and substituted ureas," *Organic Magnetic Resonance*, vol. 13, no. 1, pp. 68–71, 1980.

[131] S. W. Englander, N. W. Downer, and H. Teitelbaum, "Hydrogen exchange," *Annual Review of Biochemistry*, vol. 41, no. 1, pp. 903–924, 1972.

[132] O. Bodet, S. Goerke, N. G. R. Behl, V. Roeloffs, M. Zaiss, and P. Bachert, "Amide proton transfer of carnosine in aqueous solution studied in vitro by WEX and CEST experiments," *NMR in Biomedicine*, vol. 28, no. 9, pp. 1097–1103, 2015.

[133] T. L. Hwang and A. J. Shaka, "Water suppression that works. Excitation sculpting using arbitrary wave-forms and pulsed-field gradients," *Journal of Magnetic Resonance, Series A*, vol. 112, no. 2, pp. 275–279, 1995.

[134] L. Liu, H. Mo, S. Wei, and D. Raftery, "Quantitative analysis of urea in human urine and serum by 1H nuclear magnetic resonance," *Analyst*, vol. 137, no. 3, pp. 595–600, 2012.

[135] D. L. Longo, W. Dastru, G. Digilio, J. Keupp, S. Langereis, S. Lanzardo, S. Prestigio, O. Steinbach, E. Terreno, F. Uggeri, and S. Aime, "Iopamidol as a responsive MRI-chemical exchange saturation transfer contrast agent for pH mapping of kidneys: In vivo studies in mice at 7T," *Magnetic Resonance in Medicine*, vol. 65, no. 1, pp. 202–211, 2011.

[136] S. Zhang, B. Li, J. Greer, A. J. Madhuranthakam, J. Keupp, I. E. Dimitrov, R. E. Lenkinski, I. Pedrosa, and E. Vinogradov, "Toward CEST MRI of renal masses: protocol optimization and first preliminary data," in *Proc. 27th Joint Annual Meeting & Exhibition ISMRM-ESMRMB, Paris, France*, 2018.

[137] M. Abecassis, S. T. Bartlett, A. J. Collins, C. L. Davis, F. L. Delmonico, J. J. Friedewald, R. Hays, A. Howard, E. Jones, A. B. Leichtman, R. M. Merion, R. A.

Metzger, F. Pradel, E. J. Schweitzer, R. L. Velez, and R. S. Gaston, "Kidney Transplantation as Primary Therapy for End-Stage Renal Disease: A National Kidney Foundation/Kidney Disease Outcomes Quality Initiative (NKF/KDOQI™) Conference," *Clinical Journal of the American Society of Nephrology*, vol. 3, no. 2, pp. 471 LP – 480, 2008.

[138] Y.-T. Wang, Y.-C. Li, L.-L. Yin, H. Pu, and J.-Y. Chen, "Functional assessment of transplanted kidneys with magnetic resonance imaging," *World journal of radiology*, vol. 7, no. 10, pp. 343–349, 2015.

[139] J. Lu, J. Zhou, C. Cai, S. Cai, and Z. Chen, "Observation of true and pseudo NOE signals using CEST-MRI and CEST-MRS sequences with and without lipid suppression," *Magnetic Resonance in Medicine*, vol. 73, no. 4, pp. 1615–1622, 2015.

[140] S. Zhang, J. Keupp, X. Wang, I. Dimitrov, A. J. Madhuranthakam, R. E. Lenkinski, and E. Vinogradov, "Z-spectrum appearance and interpretation in the presence of fat: Influence of acquisition parameters," *Magnetic Resonance in Medicine*, vol. 79, no. 5, pp. 2731–2737, 2018.

[141] S. Zhang, S. Seiler, X. Wang, A. J. Madhuranthakam, J. Keupp, E. E. Knippa, R. E. Lenkinski, and E. Vinogradov, "CEST-Dixon for human breast lesion characterization at 3 T: A preliminary study," *Magnetic Resonance in Medicine*, vol. 80, no. 3, pp. 895–903, 2018.

[142] J. Liu, D. C. Peters, and M. Drangova, "Method of B0 mapping with magnitude-based correction for bipolar two-point Dixon cardiac MRI," *Magnetic Resonance in Medicine*, vol. 78, no. 5, pp. 1862–1869, 2017.

[143] T. Kaewmanee, S. Benjakul, and W. Visessanguan, "Changes in chemical composition, physical properties and microstructure of duck egg as influenced by salting," *Food Chemistry*, vol. 112, no. 3, pp. 560–569, 2009.

[144] R. Jayasundar, S. Ayyar, and P. Raghunathan, "Proton resonance imaging and relaxation in raw and cooked hen eggs," *Magnetic Resonance Imaging*, vol. 15, no. 6, pp. 709–717, 1997.

[145] J. Zhou, K. Yan, and H. Zhu, "A simple model for understanding the origin of the amide proton transfer MRI signal in tissue," *Applied Magnetic Resonance*, vol. 42, no. 3, pp. 393–402, 2012.

[146] A. Ljimani, A. Caroli, C. Laustsen, S. Francis, I. A. Mendichovszky, O. Bane, F. Nery, K. Sharma, A. Pohlmann, I. A. Dekkers, J.-P. Vallee, K. Derlin, M. Notohamiprodjo, R. P. Lim, S. Palmucci, S. D. Serai, J. Periquito, Z. J. Wang, M. Froeling, H. C. Thoeny, P. Prasad, M. Schneider, T. Niendorf, P. Pullens, S. Sourbron, and E. E. Sigmund, "Consensus-based technical recommendations for clinical translation of renal diffusion-weighted MRI," *Magnetic Resonance Materials in Physics, Biology and Medicine*, vol. 33, no. 1, pp. 177–195, 2019.

[147] P. A. Yushkevich, J. Piven, H. C. Hazlett, R. G. Smith, S. Ho, J. C. Gee, and G. Gerig, "User-guided 3D active contour segmentation of anatomical structures: Significantly improved efficiency and reliability," *NeuroImage*, vol. 31, no. 3, pp. 1116–1128, 2006.

[148] F. Zimmermann, A. Korzowski, J. Breitling, J. E. Meissner, P. Schuenke, L. Loi, M. Zaiss, S. Bickelhaupt, S. Schott, H. P. Schlemmer, D. Paech, M. E. Ladd, P. Bachert, and S. Goerke, "A novel normalization for amide proton transfer CEST MRI to correct for fat signal–induced artifacts: application to human breast cancer imaging," *Magnetic Resonance in Medicine*, pp. 1–15, 2019.

[149] G. Hamilton, T. Yokoo, M. Bydder, I. Cruite, M. E. Schroeder, C. B. Sirlin, and M. S. Middleton, "In vivo characterization of the liver fat 1H MR spectrum," *NMR in Biomedicine*, vol. 24, no. 7, pp. 784–790, 2011.

[150] X. Wang, D. Hernando, and S. B. Reeder, "Sensitivity of chemical shift-encoded fat quantification to calibration of fat MR spectrum," *Magnetic resonance in Medicine*, vol. 75, no. 2, pp. 845–851, 2016.

[151] *IDEA User's Guide*, Siemens Healthcare.

[152] M. Zaiss, P. Ehses, and K. Scheffler, "Snapshot-CEST: Optimizing spiral-centric-reordered gradient echo acquisition for fast and robust 3D CEST MRI at 9.4 T," *NMR in Biomedicine*, vol. 31, no. 4, p. e3879, 2018.

[153] D. B. Richardson, J. R. MacFall, H. D. Sostman, and C. E. Spritzer, "Asymmetric-echo, short TE, retrospectively gated MR imaging of the heart and pulmonary vessels," *Journal of Magnetic Resonance Imaging*, vol. 4, no. 2, pp. 131–137, 1994.

[154] M. A. Griswold, P. M. Jakob, R. M. Heidemann, M. Nittka, V. Jellus, J. Wang, B. Kiefer, and A. Haase, "Generalized autocalibrating partially parallel acquisitions (GRAPPA)," *Magnetic Resonance in Medicine*, vol. 47, no. 6, pp. 1202–1210, 2002.

[155] W. Jiang, I. Y. Zhou, L. Wen, X. Zhou, and P. Z. Sun, "A theoretical analysis of chemical exchange saturation transfer echo planar imaging (CEST-EPI) steady state solution and the CEST sensitivity efficiency-based optimization approach," *Contrast Media & Molecular Imaging*, vol. 11, no. 5, pp. 415–423, 2016.

[156] S. Zhang, Z. Liu, A. Grant, J. Keupp, R. E. Lenkinski, and E. Vinogradov, "Balanced steady-state free precession (bSSFP) from an effective field perspective: Application to the detection of chemical exchange (bSSFPX)," *Journal of Magnetic Resonance*, vol. 275, pp. 55–67, 2017.

[157] D. H. Tse, N. A. da Silva, B. A. Poser, and N. J. Shah, "Inhomogeneity mitigation in CEST using parallel transmission," *Magnetic Resonance in Medicine*, vol. 78, no. 6, pp. 2216–2225, 2017.

[158] Y. Zhang, H.-Y. Heo, D.-H. Lee, S. Jiang, X. Zhao, P. A. Bottomley, and J. Zhou, "Chemical exchange saturation transfer (CEST) imaging with fast variably-accelerated sensitivity encoding (vSENSE)," *Magnetic Resonance in Medicine*, vol. 77, no. 6, pp. 2225–2238, 2017.

[159] H.-Y. Heo, Y. Zhang, D.-H. Lee, S. Jiang, X. Zhao, and J. Zhou, "Accelerating chemical exchange saturation transfer (CEST) MRI by combining compressed sensing and sensitivity encoding techniques," *Magnetic Resonance in Medicine*, vol. 77, no. 2, pp. 779–786, 2017.

[160] H. She, J. S. Greer, S. Zhang, B. Li, J. Keupp, A. J. Madhuranthakam, I. E. Dimitrov, R. E. Lenkinski, and E. Vinogradov, "Accelerating chemical exchange saturation transfer MRI with parallel blind compressed sensing," *Magnetic Resonance in Medicine*, vol. 81, no. 1, pp. 504–513, 2019.

[161] M. Zaiss, G. Angelovski, E. Demetriou, M. T. McMahon, X. Golay, and K. Scheffler, "QUESP and QUEST revisited - fast and accurate quantitative CEST experiments," *Magnetic Resonance in Medicine*, vol. 79, no. 3, pp. 1708–1721, 2017.

[162] O. Cohen, S. Huang, M. T. McMahon, M. S. Rosen, and C. T. Farrar, "Rapid and quantitative chemical exchange saturation transfer (CEST) imaging with magnetic resonance fingerprinting (MRF)," *Magnetic resonance in Medicine*, vol. 80, no. 6, pp. 2449–2463, 2018.

[163] M. Zaiss, A. Deshmane, M. Schuppert, K. Herz, F. Glang, P. Ehses, T. Lindig, B. Bender, U. Ernemann, and K. Scheffler, "DeepCEST: 9.4 T chemical exchange saturation transfer MRI contrast predicted from 3 T data – a proof of concept study," *Magnetic Resonance in Medicine*, vol. 81, no. 6, pp. 3901–3914, 2019.

[164] F. Glang, A. Deshmane, S. Prokudin, F. Martin, K. Herz, T. Lindig, B. Bender, K. Scheffler, and M. Zaiss, "DeepCEST 3T: Robust MRI parameter determination and uncertainty quantification with neural networks—application to CEST imaging of the human brain at 3T," *Magnetic Resonance in Medicine*, vol. 84, no. 1, pp. 450–466, 2020.

[165] B. Kim, M. Schär, H. Park, and H.-Y. Heo, "A deep learning approach for magnetization transfer contrast mr fingerprinting and chemical exchange saturation transfer imaging," *NeuroImage*, p. 117165, 2020.

[166] S. H. Shin, M. F. Wendland, B. Zhang, A. Tran, A. Tang, and M. H. Vandsburger, "Noninvasive imaging of renal urea handling by CEST-MRI," *Magnetic Resonance in Medicine*, no. August, pp. 1–11, 2019.

[167] E. Vinogradov, Z. Liu, A. Madhuranthakarn, A. Hajibeigi, A. Jump, I. Pedrosa, O. W. Moe, and R. E. Lenkinski, "Endogenous urea CEST (urCEST) for MRI monitoring of kidney function," in *Proc. 23th Annual Meeting & Exhibition ISMRM, Toronto, Canada*, 2015.

[168] J. Xu, N. N. Yadav, A. Bar-Shir, C. K. Jones, K. W. Y. Chan, J. Zhang, P. Walczak, M. T. McMahon, and P. C. M. van Zijl, "Variable delay multi-pulse train for fast chemical exchange saturation transfer and relayed-nuclear overhauser enhancement MRI," *Magnetic Resonance in Medicine*, vol. 71, no. 5, pp. 1798–1812, 2013.

[169] L. Chen, X. Xu, H. Zeng, K. W. Chan, N. Yadav, S. Cai, K. J. Schunke, N. Faraday, P. C. van Zijl, and J. Xu, "Separating fast and slow exchange transfer and magnetization transfer using off-resonance variable-delay multiple-pulse (VDMP) MRI," *Magnetic Resonance in Medicine*, vol. 80, no. 4, pp. 1568–1576, 2018.

[170] K. L. Desmond, F. Moosvi, and G. J. Stanisz, "Mapping of amide, amine, and aliphatic peaks in the CEST spectra of murine xenografts at 7T," *Magnetic Resonance in Medicine*, vol. 71, no. 5, pp. 1841–1853, 2013.

[171] S. Zheng, I. M. J. van der Bom, Z. Zu, G. Lin, Y. Zhao, and M. J. Gounis, "Chemical exchange saturation transfer effect in blood," *Magnetic Resonance in Medicine*, vol. 71, no. 3, pp. 1082–1092, 2013.

[172] Y. Wu, S. Zhang, T. C. Soesbe, J. Yu, E. Vinogradov, R. E. Lenkinski, and A. D. Sherry, "pH imaging of mouse kidneys in vivo using a frequency-dependent paracest agent," *Magnetic resonance in Medicine*, vol. 75, no. 6, pp. 2432–2441, 2016.

[173] X. Yang, X. Song, S. Ray Banerjee, Y. Li, Y. Byun, G. Liu, Z. M. Bhujwalla, M. G. Pomper, and M. T. McMahon, "Developing imidazoles as CEST MRI pH sensors," *Contrast Media & Molecular Imaging*, vol. 11, no. 4, pp. 304–312, 2016.

Appendix A

Publication 1

The results of **study 1** have been published in:

Stabinska J*, Cronenberg T*, Wittsack HJ, Lanzman RS, Müller-Lutz A. Quantitative pulsed CEST-MRI at a clinical 3T MRI system. Magn Reson Mater Phy. 2017; 30:505–516. doi: 10.1007/s10334-017-0625-0.

Impact factor (2017): 1.832

Personal contribution: 40% (data analysis, data interpretation, manuscript writing, manuscript revision)

* These authors contributed equally to this work.

Magn Reson Mater Phy (2017) 30:505–516
DOI 10.1007/s10334-017-0625-0

RESEARCH ARTICLE

Quantitative pulsed CEST-MRI at a clinical 3T MRI system

Julia Stabinska[1] · Tom Cronenberg[1] · Hans-Jörg Wittsack[1] · Rotem Shlomo Lanzman[1] · Anja Müller-Lutz[1]

Received: 16 January 2017 / Revised: 28 April 2017 / Accepted: 12 May 2017 / Published online: 31 May 2017

Abstract
Objectives The goal of this study was to quantify CEST related parameters such as chemical exchange rate and fractional concentration of exchanging protons at a clinical 3T scanner. For this purpose, two CEST quantification approaches—the AREX metric (for 'apparent exchange dependent relaxation'), and the AREX-based Ω-plot method were used. In addition, two different pulsed RF irradiation schemes, using Gaussian-shaped and spin-lock pulses, were compared.
Materials and methods Numerical simulations as well as MRI measurements in phantoms were performed. For simulations, the Bloch–McConnell equations were solved using a two-pool exchange model. MR experiments were performed on a clinical 3T MRI scanner using a cylindrical phantom filled with creatine solution at different pH values and different concentrations.
Results The validity of the Ω-plot method and the AREX approach using spin-lock preparation for determination of the quantitative CEST parameters was demonstrated. Especially promising results were achieved for the Ω-plot method when the spin-lock preparation was employed.
Conclusion Pulsed CEST at 3T could be used to quantify parameters such as exchange rate constants and concentrations of protons exchanging with free water. In the future this technique might be used to estimate the exchange rates and concentrations of biochemical substances in human tissues in vivo.

Keywords Chemical exchange saturation transfer (CEST) · Magnetic resonance imaging (MRI) · Creatine

Introduction

Chemical exchange saturation transfer (CEST) represents a new molecular MRI technique that enables indirect detection of labile solute protons through bulk water signal changes following selective saturation of exchangeable protons at different frequencies [1–3]. Several CEST MRI approaches have been shown capable of measuring dilute CEST agents and microenvironmental properties such as pH and temperature [4–6].

Since the CEST effect varies with labile proton ratio, exchange rate, and experimental conditions such as field strength and radiofrequency (RF) irradiation scheme, there is a need to develop quantitative CEST analysis for defining underlying CEST parameters [7, 8]. Several analytical and numerical methods have been established to determine labile proton concentration and exchange rate from the CEST-weighted data [9–12]. Two approaches to measure the labile proton ratio-weighted exchange rate as a function of saturation time (QUEST) and saturation power (QUESP) have been proposed by McMahon et al. [10]. The exchange rates are determined by fitting the changes in the intensity of the water signal after application of different saturation powers (QUESP) or saturation times (QUEST) to the modified Bloch–McConnell equations. Dixon et al. extended the QUESP method and showed that the CEST effect can be represented as a linear function of $1/B_1^2$ (the so-called Ω-plot) and that the proton exchange

Julia Stabinska and Tom Cronenberg contributed equally to this work.

✉ Julia Stabinska
Julia.Stabinska@med.uni-duesseldorf.de

[1] Department of Diagnostic and Interventional Radiology, Medical Faculty, University Dusseldorf, Moorenstr. 5, 40225 Düsseldorf, Germany

rate and labile proton ratio can be determined independently by linear regression of the CEST effect [11]. However, this method is limited to paramagnetic CEST agents (PARACEST) that exhibit large chemical shifts. As a result, the selective RF pulse is applied far from the free water resonance frequency, which reduces direct water saturation (spillover) and magnetization transfer effects [3]. The QUEST ratiometric analysis (QUESTRA) has been shown to correct the influence of confounding factors, such as relaxation and spillover effects [12]. Nevertheless, it provides only the labile proton ratio-weighted exchange rate. More recently, it has been presented that the spillover factor is not sensitive to the labile proton ratio and exchange rate, and therefore can be estimated and efficiently corrected by the inverse metric [13, 14]. Sun et al. demonstrated that the RF spillover-factor Ω-plot method provides good quantification in the case of endogenous CEST agents with small chemical shifts [7, 15]. However, they performed their experiments using continuous-wave (CW) saturation, which is usually not feasible on clinical scanners due to the hardware and specific absorption rate (SAR) limitations. Thus, the pulsed train pre-saturation scheme must be used instead [16, 17]. Sun et al. compared pulsed- and continuous wave—RF irradiation schemes for CEST and showed that the maximal pulsed-CEST contrast is approximately 95% of CW-CEST and that their optimal saturation RF power is approximately equal [18]. A theoretical model for pulsed-CEST experiments and optimized saturation scheme was defined by Schmitt et al. [16]. To translate quantitative CEST to clinical MRI systems, the pulsed quantitative CEST approaches such as AREX ('apparent exchange dependent relaxation') and AREX-based Ω-plots method have been proposed [19, 20]. Zaiss et al. introduced a novel metrics, MTR_{Rex}, which eliminates spillover and semi-solid MT effects and then extended it to the AREX, a T_1 relaxation-compensated metric, which in turn facilitates quantification of the CEST effect [21]. The analytic description of the spillover corrected Ω-plot method in the case of pulsed CEST was proposed by Meissner et al. [20]. However, they performed the CEST MRI experiments at high field strength (7T). Although higher magnetic field strengths are beneficial to the CEST phenomenon, the commonly used field strengths on clinical MR usually do not surpass 3T.

Recently, spin-lock (SL) saturation preparation for pulsed chemical exchange MR imaging has been introduced [22, 23]. Pulsed SL may provide several advantages over the conventional pulsed CEST: (1) higher signal-to-noise ratio (SNR) by restoring magnetization along the longitudinal axis of the rotating frame [22, 24]; (2) less direct water saturation because of the suppression of the magnetization rotations in the transversal plane [22]; and (3) increase of the saturation efficiency compared with the conventional CEST [23]. Chemical exchange imaging with spin-lock technique has also been shown to better characterize the chemical exchange processes when the resonant frequency offsets are small (e.g., <2 ppm) and the exchange is in the intermediate to fast regime compared with the CEST in the case of saturation by a train of Gaussian-shaped RF pulses [25, 26].

The aim of this study was (1) to evaluate quantitative CEST parameters using the AREX metric and the AREX-based Ω-plot method and (2) to compare two different saturation schemes at a clinical 3T MRI system.

Materials and methods

Quantitative parameter determination

Zaiss et al. proposed a novel magnetization transfer ratio, which eliminates spillover and semi-solid macromolecular magnetization transfer (MT) [21]:

$$\mathrm{MTR_{Rex}} = \frac{1}{Z_{\mathrm{lab}}} - \frac{1}{Z_{\mathrm{ref}}} = \frac{R_{\mathrm{ex}} \cdot \mathrm{DC}}{R_{1\mathrm{w}}}, \quad (1)$$

where $Z_{\mathrm{lab}} = Z(+\Delta\omega)$ is the label scan around the resonance of the CEST pool (s) and $Z_{\mathrm{ref}} = Z(-\Delta\omega)$, the reference scan at the opposite frequency with respect to water; R_{ex} is the exchange-dependent relaxation in the rotating frame; DC is the duty cycle and $R_{1\mathrm{w}}$ is the relaxation rate of the water pool (w). The $\mathrm{MTR_{Rex}}$ metric could be extended to an apparent exchange dependent relaxation metric—AREX [21]:

$$\mathrm{AREX} = \mathrm{MTR_{Rex}} R_{1\mathrm{w}}. \quad (2)$$

In the full saturation limit (1) $\omega_1 \quad R_{2\mathrm{s}} + k_{\mathrm{sw}}$ and in the large-shift limit (2) $\delta\omega_{\mathrm{s}} \quad \omega_1$, when applying RF pulse at the CEST pool resonance, $R_{\mathrm{ex}} = f \cdot k_{\mathrm{ws}}$ and, hence:

$$\mathrm{AREX} = k_{\mathrm{ws}} \cdot \mathrm{DC}, \quad (3)$$

where ω_I is the RF irradiation amplitude; $R_{2\mathrm{s}}$ the relaxation rate of the pool s; $\delta\omega_{\mathrm{s}}$ is the chemical shift of the pool s; k_{sw} and k_{ws} are the exchange rate between pool s and w and back exchange rate, respectively, and f is the labile proton ratio.

Assuming the f is known, we can calculate the chemical exchange rate k_{sw}:

$$k_{\mathrm{sw}} = \frac{\mathrm{AREX}}{\mathrm{DC} \cdot f}. \quad (4)$$

The relaxation-compensated Ω-plot analysis can be applied to the AREX signal. For this purpose, a stack of the AREX maps for different RF amplitudes B_1 is created and then fitted with the equation [20]:

$$\frac{1}{\mathrm{AREX}}\left(\frac{1}{\omega^2}\right) = p_0 + p_1 \cdot \frac{1}{\omega^2}, \tag{5}$$

where p_0 is an intersection p_1, the slope of the linear function.

For shaped pulses (e.g., Gaussian), a time dependent $\omega_1(t)$ has to be taken into account. Meissner et al. calculated the average longitudinal relaxation rate in the rotating frame $R_{1\rho}$ as a function of the pulse shape [20]. This method allows the calculation of form factors for the modified CEST signals and the B_1 dispersion of the CEST effect in the case of using a pulsed saturation scheme. For the Gaussian-shaped pulse, the form factors are defined as follows [20]:

$$c_1 = \frac{\sqrt{2\pi}\sigma}{t_p} \tag{6}$$

$$c_2 = c_1 \cdot \sqrt{\sqrt{2}}. \tag{7}$$

For the experiment with spin-lock pulses: $c_1 = c_2 = 1$.

The exchange-dependent relaxation R_{ex} in the case of pulsed pre-saturation can be approximated as:

$$R_{\mathrm{ex}}^{\mathrm{shaped}} = f k_{\mathrm{sw}} c_1 \frac{\omega_1^2}{\omega_1^2 + k_{\mathrm{sw}}(k_{\mathrm{sw}} + R_{2\mathrm{s}})c_2^2}. \tag{8}$$

Using Eqs. (1), (2) and (8) as well as p_1 and p_0 values determined from the linear Eq. (5) enables quantification of k_{sw} and f with the following equations:

$$k_{\mathrm{sw}} = -\frac{R_{2\mathrm{s}}}{2} + \sqrt{\frac{(R_{2\mathrm{s}})^2}{4} + \frac{p_1}{p_0 \cdot c_2^2}}. \tag{9}$$

$$f = \frac{1}{c_1 \cdot \mathrm{DC} \cdot p_0 \cdot \left(-\frac{R_{2\mathrm{s}}}{2} + \sqrt{\frac{(R_{2\mathrm{s}})^2}{4} + \frac{p_1}{p_0 \cdot c_2^2}}\right)}. \tag{10}$$

Both considered methods use a Z-spectrum model in the pulsed CEST experiment given by Zaiss et al. [21]. This model is valid if several key conditions defined by Meissner et al. are met [20]: (1) small CEST pool ($f < 1\%$), (2) sufficiently long saturation times ($t_{\mathrm{sat}} > T_{2\mathrm{w}}$), (3) exchange dynamic is faster than the pulse dynamic ($k_{\mathrm{sw}} > 1/t_p$), (4) exchange dynamic in the interpulse delay can be neglected ($k_{\mathrm{sw}} < 1/t_d$), (5) analytical integral of $R_{1\rho}$ is valid ($\Delta\omega > \omega_1$), (6) the approximation of the analytical derived form factors of a Gaussian-shaped pulse is satisfactory ($\sigma/t_p < 0.5$), where σ is the width of the pulse. In contrast to the original Ω-plot method proposed by Dixon et al., there are two other limitations for the AREX-based Ω-plot method; (7) $R_{1\rho}t_p$ 1 and $R_{1\mathrm{w}}t_d$ 1 and (8) $\omega_1^2 < 0.5 \cdot k_{\mathrm{sw}}.(k_{\mathrm{sw}} + R_{2\mathrm{s}})$. Last but not least, the steady-state condition as for the AREX method has to be fulfilled (9) $t_{\mathrm{sat}} \geq 5 \cdot T_{1\mathrm{w}}$.

Numerical simulations

For simulations, the Bloch–McConnell (BM) equations were solved using Matlab (Matlab R2012a, Mathworks, Natick, MA, USA) by a two-pool exchange model as proposed by Murase et al. [27], assuming representative $T_{1\mathrm{w}} = 2.473$ s and $T_{2\mathrm{w}} = 1.676$ s for the bulk water, and $T_{1\mathrm{s}} = 0.5$ s and $T_{2\mathrm{s}} = 0.015$ s for labile protons at 1.9 ppm at 3T, respectively [21]. The saturation scheme consisted either of 50 Gaussian-shaped, or 50 spin-lock pulses with pulse duration and inter-pulse delay $t_p = t_d = 100$ ms. The spin-lock magnetization preparation pulse was obtained by using the rotation matrix:

$$M(\alpha) = \begin{pmatrix} 1 & 0 & 0 \\ 0 & \cos\alpha & -\sin\alpha \\ 0 & \sin\alpha & \cos\alpha \end{pmatrix}, \tag{11}$$

where $\alpha = \Theta$ or $-\Theta$.

The quantitative CEST analysis was applied to the simulated data, to assess the accuracy of the methods over a wide range of B_1, f and k_{sw} values. The results were then normalized to the theoretical values from the BM simulations, giving the normalized exchange rate $k_{\mathrm{sw}}^{\mathrm{norm}}$ and the normalized labile proton ratio f^{norm} maps.

General simulation parameters are listed in Table 2 in the "Appendix".

Phantom

For MR experiments, three sets of phantoms were employed, each containing four 60 mL tubes (Table 1). Eleven samples, using phosphate buffer and creatine solution (Creatine anhydrous, Alfa Aesar GmbH & Co KGm Karlsruhe, Germany), were prepared at room temperature. Three phantoms either consisting of creatine solutions with varying pH values (Phantom 1&2) or varying molar concentration (Phantom 3) were obtained. The labile proton ratio f was calculated using the equation: $N \cdot [\mathrm{Cr}]/2 \cdot [\mathrm{H_2O}]$, where N is the number of labile protons per creatine molecule, and $[\mathrm{H_2O}]$ and [Cr] are water and creatine molar concentration, respectively. The number of exchangeable protons per creatine molecule was assumed to be four [19, 28]. To assess the accuracy of the determined chemical exchange rate from labile protons s to bulk water w, the reference k_{sw} value for creatine was calculated from the empirical equation [28]:

Table 1 Phantoms employed with the reference $k_{sw,ref}$ value obtained from the empirical relation given in Eq. (12), reference labile proton ratio f_{ref} and k_{sw} and f values determined using quantitative CEST analysis

					AREX method			Ω-plot method			
					Pulsed SL	Gaussian-shaped pulses		Pulsed SL		Gaussian-shaped pulses	
Phantom	pH	c (Mm)	$k_{sw,ref}$ (Hz)	f_{ref} (‰)	k_{sw} (Hz)	k_{sw} (Hz)		k_{sw} (Hz)	f (‰)	k_{sw} (Hz)	f (‰)
1	6.15	50	23.17	1.8	38.48 ± 2.73	33.58 ± 2.82		41.21 ± 7.63	1.8 ± 0.34	56.32 ± 11.02	1.9 ± 0.39
1	6.31	50	33.50	1.8	49.58 ± 3.33	41.44 ± 2.95		49.88 ± 7.34	1.9 ± 0.27	65.76 ± 11.11	2.0 ± 0.32
1	6.52	50	54.32	1.8	69.99 ± 4.53	56.00 ± 3.59		68.86 ± 8.66	2.0 ± 0.2	81.78 ± 11.62	2.2 ± 0.26
1	6.70	50	82.22	1.8	94.41 ± 4.36	71.14 ± 3.60		93.28 ± 10.24	2.0 ± 0.17	98.28 ± 9.84	2.3 ± 0.21
2	6.83	50	110.91	1.8	133.87 ± 5.68	92.2 ± 4.61		116.94 ± 8.46	2.3 ± 0.17	141.68 ± 11.16	2.2 ± 0.17
2&3	7.02	50	171.78	1.8	174.81 ± 8.90	117.15 ± 6.56		162.18 ± 10.67	2.3 ± 0.14	173.30 ± 12.55	2.3 ± 0.17
2	7.21	50	266.06	1.8	243.54 ± 11.62	157.67 ± 7.62		259.83 ± 21.72	2.3 ± 0.12	249.92 ± 17.29	2.3 ± 0.14
2	7.51	50	530.86	1.8	312.88 ± 19.47	213.57 ± 10.29		492.72 ± 63.89	2.3 ± 0.16	413.60 ± 27.65	2.2 ± 0.11
3	7.02	25	171.78	0.9	182.04 ± 9.43	124.67 ± 7.08		185.35 ± 46.10	1.2 ± 0.10	160.73 ± 22.29	1.3 ± 0.14
3	7.02	75	171.78	2.7	172.30 ± 7.77	118.76 ± 5.70		163.76 ± 17.20	3.4 ± 0.18	167.91 ± 12.12	3.6 ± 0.22
3	7.02	100	171.78	3.6	174.38 ± 9.70	119.02 ± 5.36		161.20 ± 12.52	4.7 ± 0.27	267.20 ± 8.68	4.9 ± 0.25

$$k_{sw}(298.15\text{K}) \approx k_{b,eff}(298.15\text{K}) \cdot \frac{\text{mol}}{\text{L}} \cdot 10^{\text{pH}-14+\frac{E_{A,b,eff}+\Delta H_R^0}{R\cdot\ln 10}\left(\frac{1}{298.15\text{K}}-\frac{1}{T}\right)}, \quad (12)$$

where $k_{b,eff}$ (298.15 K) = 3.009 × 10^9 Hz L mol^{-1}, $E_{A,b,eff}$ = 32.27 kJ mol^{-1}, ΔH_R^0 = 55.84 kJ mol^{-1} and R = 8.314 $mol^{-1}K^{-1}$. Recently, the effective base-catalyzed rate constant $k_{b,eff}$ and the effective activation energy $E_{A,b,eff}$ were estimated by Goerke et al. [28] by means of water-exchange (WEX)-filtered 1H NMR spectroscopy. Thus, this method served us as a reference method for measuring the exchange rate of creatine. The k_{sw} values derived from Eq. (12) formed our 'ground truth' and are listed in Table 1.

MRI experiments

All measurements were performed on a clinical 3T MR scanner (Magentom Trio A Tim System, Siemens Healthcare, Erlangen, Germany) with a 12-channel birdcage coil. A 2-D single-shot gradient echo sequence (GRE) as described in [16] was used for CEST image data acquisition. The following parameters were chosen: field of view FOV = 130 mm × 130 mm, image matrix = 64 × 64, slice thickness = 8 mm, repetition time T_R = 7.3 ms, echo time T_E = 3.41 ms, and flip angle = 10°. Sampling was performed equidistantly at 41 various frequency offsets between −3.5 and 3.5 ppm. An additional scan at frequency offset −300 ppm was acquired for normalization. The saturation module consisted either of 50 Gaussian-shaped, or 50 spin lock pulses with $t_p = t_d$ = 100 ms and RF pulse amplitudes B_1 of 0.25, 0.5, 1.0, 1.25, 1.65, and 2.1 μT. Each of the spin lock pulses is flanked by two Gaussian-shaped RF pulses with the flip angle θ and opposite phase, where θ is the angle between the effective field and the z-axis. A simplified schematic CEST pulse sequence diagram (Fig. 1) is included in the appendix. The water saturation shift referencing (WASSR) method for B_0 inhomogeneity correction was used [29]. Here, a single Gaussian pulse with t_{pd} = 56 ms and RF amplitude B_1 = 0.1 μT was employed. Additionally, T1-weighted MR images were acquired by a turbo-inversion-recovery sequence. Altogether, 13 contrasts at different inversion delays (TI) ranging from 25 ms to 3.2 s were fitted to obtain T1 maps.

Data processing

All data were processed using Matlab. The T_1 maps were obtained by least-squares fitting of the IR measurements data as a function of the inversion delay (TI): S (TI) ∝ S_0 (1–2·exp(−TI/T_1)), where S_0 is the equilibrium signal. To reduce noise, a 5 × 5 Gaussian filter was applied to each CEST and WASSR image. Based on the WASSR images, an offset map were calculated using the WASSR maximum

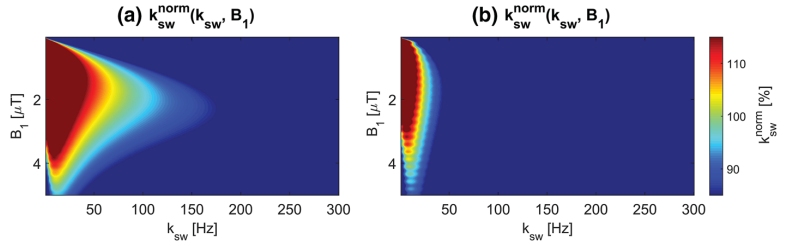

Fig. 1 Normalized exchange rate k_{sw}^{norm} maps with a *color-coded* error range of 15% for the AREX method with (**a**) pulsed SL (**b**) trains of Gaussian-shaped pulses used for saturation. The k_{sw} values obtained from the quantitative CEST analysis were normalized to the theoretical values from the BM simulations

symmetry algorithm introduced by Kim et al. [29, 30]. The CEST data were normalized to the signal from the first acquisition at frequency offset −300 ppm. The offset map was used to correct the Z-spectrum on a pixel-basis. The inverse asymmetry MTR_{Rex} maps were generated at 1.9 ppm. Next, the AREX maps was calculated using average T_1 times, which were obtained as an average of the four tubes of each phantom. Finally, the relaxation-compensated Ω-plot analysis was then applied to the AREX signal. The form factors for the Gaussian-shaped pulses employed in this work were $c_1 = 0.5672$ and $c_2 = 0.6171$. In the case of spin-lock pulses, the form factors were $c_1 = c_2 = 1$. It was also assumed that $R_{2s} = 66.67$ Hz [31].

The measured data in the studied ROIs were tested for normal distribution using the Kolmogorov–Smirnov Test (KS Test) with $\alpha = 0.05$. Since the results deviated significantly from the normal distribution, the non-parametric Wilcoxon–Mann–Whitney test with a level of significance (p value) $\alpha = 0.05$ was used.

Results

Simulations

The Bloch–McConnell simulations over a wide range of B_1, f and k_{sw} values revealed significant differences in accuracy and feasibility between the examined CEST quantification methods and between two considered saturation pulse shapes. To demonstrate the general applicability of the methods, we calculated a normalized exchange rate k_{sw}^{norm} map and a normalized labile proton ratio f^{norm} map (only for the Ω-plot method) with a color-coded error range of ±15%. Note that independently of the irradiation scheme and quantification method, the lower exchange rates tend to be strongly overestimated in nearly the whole range of B_1 values. The AREX approach generates sufficiently accurate results in the k_{sw} range of 100 ± 50 Hz when applying the pulsed SL and B_1 between 1 and 3 μT (Fig. 1a), and in the k_{sw} range of about 30 ± 15 Hz using Gaussian-shaped RF pulses (Fig. 1b).

An advantage of the AREX-based Ω-plot method is the possibility of simultaneous determination of exchange rate and the labile proton ratio. Applying spin-lock pulses, both parameters can be estimated with very good accuracy over a wide range of k_{sw}, although the accuracy decreases at larger k_{sw} rates. This decreased accuracy at faster k_{sw} is amplified as the saturation power increases (Fig. 2a, c). This method can produce accurate estimates of fractional concentration for k_{sw} smaller than about 400 Hz at lower RF power (Fig. 2c, d). The results of the Ω-plot method for the Gaussian-shaped pulses show its decreased range of applicability in comparison to results obtained with the pulsed SL. The accuracy of the estimation of k_{sw} is strongly overestimated for slower k_{sw} rates (<100 Hz), but also significantly underestimated for faster k_{sw} rates. These accuracies are also nearly independent of the saturation power (Fig. 2e) and labile proton ratio (Fig. 2f).

In vitro MR experiments

To validate the simulations, we performed phantom MR measurements (Table 1). First, we determined the exchange rates as a function of pH (phantom 1 and phantom 2, Table 1) (Fig. 3b). For the graphic presentation, we normalized the results to the reference k_{sw} values obtained from the Eq. (12) (Table 1). At lower pH the k_{sw} rates are substantially overestimated. This is consistent with simulation findings. Interestingly, the AREX metric shows smaller error intervals than the Ω-plot method, regardless of pH value. Due to its small error and a good agreement with the corresponding reference value, the AREX method when using pulsed SL could be applicable for exchange rates between about 80–270 Hz (please see Table 1). It is worth noting, that the results of the Ω-plot method are in very good agreement with the reference values in the k_{sw} range

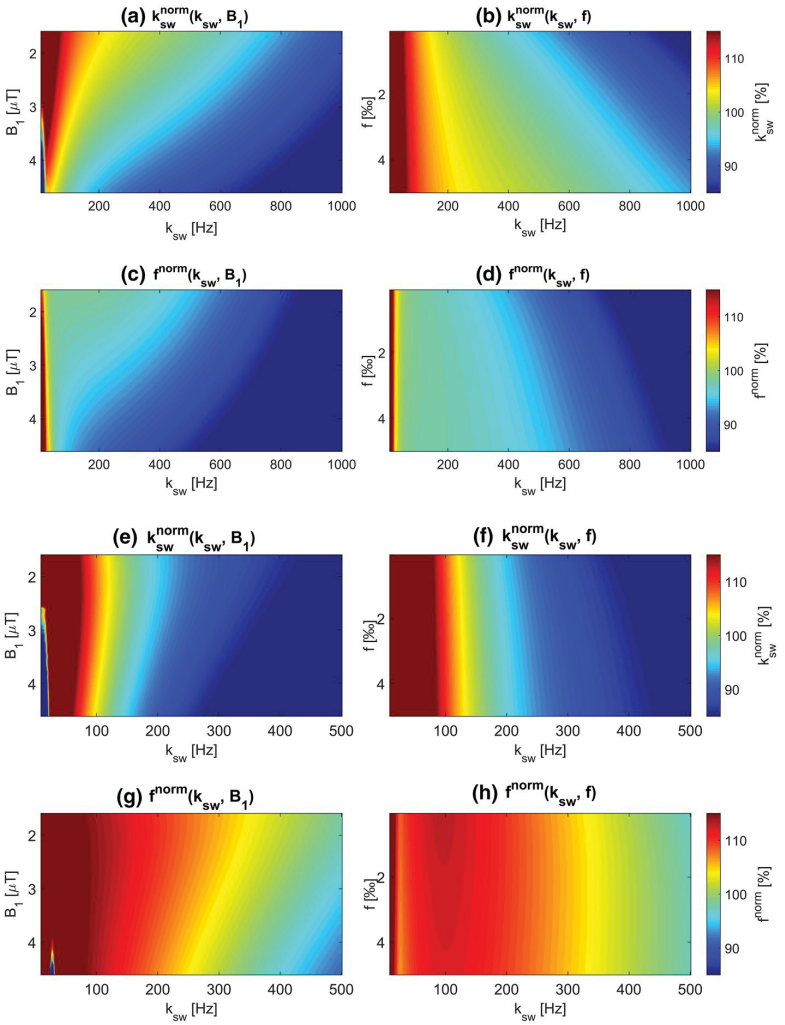

Fig. 2 Parameter maps with *color-coded* error range of 15% for the Ω-plot method with (**a**–**d**) pulsed SL and (**e**–**h**) trains of Gaussian-shaped pulses used for saturation. **a**, **d** The normalized exchange rate map k_{sw}^{norm} as a function of k_{sw} and B_1 **b**, **f** the normalized exchange rate map k_{sw}^{norm} as a function of k_{sw} and f, **c**, **g** the normalized labile proton ratio f^{norm} map as a function of k_{sw} and B_1, **d**, **h** the normalized labile proton ratio f^{norm} map as a function of k_{sw} and f. The k_{sw} and f values obtained from the quantitative CEST analysis were normalized to the theoretical values from the BM simulations

between 50 and 530 Hz if the spin-lock saturation preparation was applied. In the case of using Gaussian-shaped RF pulses, the Ω-plot method estimates the exchange rates between 170 and 530 Hz within the ±15% error range. Except for the AREX method and pulsed SL saturation scheme at pH 6.52 and 6.70 ($p = 0.925$), pH 6.52 and 6.83 ($p = 0.7031$), pH 6.70 and 6.83 ($p = 0.7631$), results of all other pairs were significantly different.

To further evaluate the Ω-plot methods when applying different pulsed pre-saturation schemes, we determined the labile proton ratios as a function of creatine molar concentration (phantom 3, Table 1) (Fig. 4). The number of labile protons per creatine molecule was assumed to be four [19, 28]. Our results verified the linear dependence of the labile proton ratio on creatine concentration. For both irradiation schemes, the results appear to be constantly overestimated, which is more substantial in the case of Gaussian-shaped RF pulse trains. All results were significantly different.

Next, we obtained the normalized exchange rate for different creatine concentrations (phantom 3, Table 1) at pH 7.0. In particular, the exchange rates estimated by means of the AREX method and pulsed SL, are in good agreement with the expected value. The variations of the results for the Ω-plot method also remain within the ±15% error range for creatine concentrations above 25 mM. In comparison to the

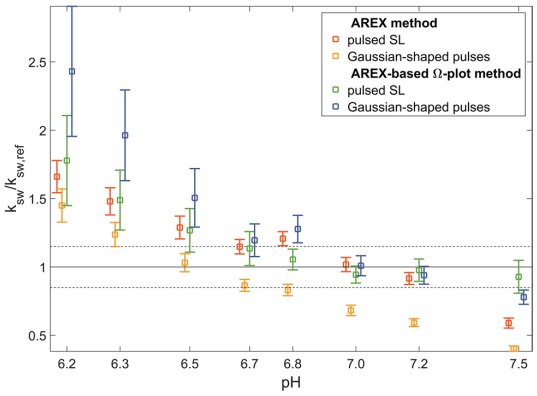

Fig. 3 Exchange rates k_{sw} estimates determined at varying pH values, normalized to the reference value $k_{sw,ref}$ obtained from the empirical relation given in Eq. (12) (Table 1). *Dashed lines* represent the 15% error tolerances

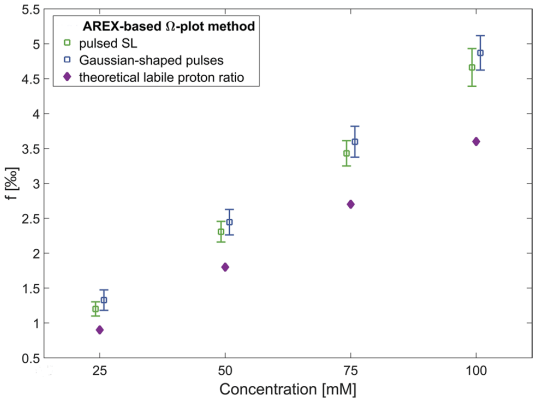

Fig. 4 Labile proton ratio f estimates determined at different creatine concentrations (25, 50, 75 and 100 mM) using the AREX-based Ω-plot method and two different RF saturation schemes—pulsed SL (*green square*) and Gaussian-shaped RF pulses (*blue square*). *Purple diamonds* represent theoretical labile proton ratio values

results obtained using the spin-lock saturation scheme, the k_{sw} rates determined with the AREX method when using Gaussian-shaped RF pulses are strongly underestimated. The deviation from the reference value is about 30% (Fig. 5).

Discussion

In the present study we compared two CEST quantification methods and two different saturation schemes based

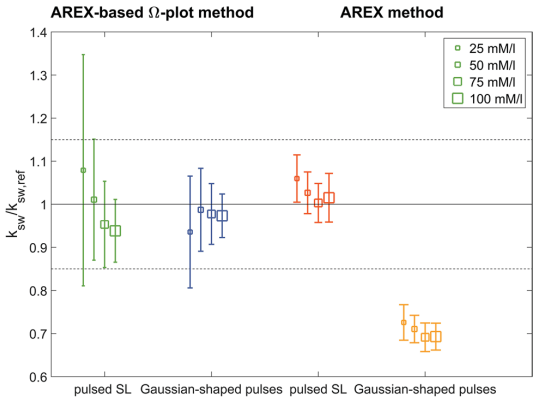

Fig. 5 Exchange rates k_{sw} estimates determined using Ω-plot analysis (*green* and *blue squares*) and the AREX method (*red* and *orange squares*) at different creatine concentrations (25, 50, 75, 100 mM) at pH 7, normalized to the reference value $k_{sw,ref}$ obtained from the empirical relation given in Eq. (12) (Table 1). *Dashed lines* represent the 15% error tolerances

on Gaussian-shaped RF pulse train and pulsed spin-lock preparation. Moreover, we performed our experiments at a clinical 3T MRI system.

The CEST methods evaluated in this study are based on several conditions. Our simulations revealed that all considered quantitative CEST methods tend to overestimate lower exchange rates. It is worth noting that the pulsed approach, used here, is based on the assumption that during the saturation pulse the water magnetization is "locked" in the direction of ω_{eff} and decays with the rate $R_{1\rho}$ and recovers during the interpulse delay t_d with the rate R_{1w} [22]. However, Roeloffs et al. showed that a biexponential decay of magnetization during the break should be taken into account. For exchange rates that are comparable with the inverse of the interpulse delay, this additional magnetization transfer may lead to a significant overestimation of the exchange rates. Our simulations confirmed that each saturation technique shows different accuracy in the exchange rate determination that is dependent on the exchange regime in which the analysis is performed. Using pulsed SL, the AREX method is applicable for higher exchange rates than in the case of Gaussian-shaped saturation pulses. For the SL technique, faster exchange between the water and metabolite pool boost signal dephasing that may be reduced with sufficient locking field ω_1. Therefore, the larger this dephasing effect is, the higher contrast enhancement may be obtained. This contrast was reported to decrease dramatically at higher and lower locking fields [23, 25]. Only around the maximum contrast, the signal-to-noise ratio is

sufficient for the MTR_{Rex} metric to reconstruct the ideal signal from the residual signal [19]. Thus, the accuracy of the AREX metric for pulsed SL is not a monotonic function of k_{sw}. It can increase or decrease with the k_{sw} depending on the RF saturation power. Also, the full-saturation limit k_{sw} ω_1 has to be taken into account [19].

Since the amplitude of the saturation is not constant for Gaussian-shaped pulses, the form factors should be considered, which compensate decreased saturation efficiency of the shaped pulses compared to the rectangular pulses [19]. The form factors defined for the Ω-plot method cannot be simply transferred to the AREX metric, which contributes to the poor results of the approach when using Gaussian-shaped pulses. In this study we used the numerical derived form factors for the Gaussian-shaped pulse, which improved the estimation of k_{sw} and f_c by the Ω-plot method compared with the results obtained with the analytical derived form factors (data not shown). The results of the simulations for the Ω-plot method using the pin-locking technique showed the great potential of this method. The increasing uncertainty in the determination of the exchange rate for small labile proton ratios is consistent with limitations of the method defined by Meissner et al. [20]. However, our simulations of the Ω-plot method at the 3T system presented a smaller area of validity compared to the results obtained by Meissner et al. at 7T in the case of using Gaussian-shaped pulses [20]. The specific frequency offset $\Delta\omega$ from water should be larger than the chemical exchange rate k_{sw} in order to better identify the CEST effect from creatine (large-shift limit) [3]. Since the frequency shift increases with the magnetic field strength, this assumption is better fulfilled for a higher magnetic field strength B_0 and smaller exchange rates.

The results of our in vitro studies clearly show that quantitative CEST imaging is possible at a clinical 3T scanner. The Ω-plot qCEST method provided particularly promising results if a train of spin-lock pulses was applied. Nevertheless, further investigations are needed to validate these results in vivo.

The overestimated exchange rate for the low pH tubes confirmed the trend that became apparent in the simulations. Smaller variations of the results at higher pH values are caused by the fact that the signal-to noise ratio (SNR) increases with increasing exchange rate. At high k_{sw} values, the exchange rates estimated using spin-lock pulses and Ω-plot method are in better agreement with the reference value than in the case of Gaussian-shaped RF pulses. It should be noted that the reference values used here are based on the formula introduced by Goerke et al. [28]. They assumed a constant estimation error of 10%. However, in the more recent work of the same research group, the actual error was reported to be greater [20]. To assess the determined quantitative parameters more accurately, it might be necessary to compare the results with other reference methods, such as the fitting of CEST data to the Bloch–McConnell equations in order to estimate the exchange rates [10]. However, these methods were mainly evaluated for continuous-wave (CW) RF irradiation. When using pulsed saturation schemes, the simulations become computationally more expensive. Thus, the reasonable computing time is a great advantage of analytical, quantitative CEST methods such as AREX, Ω-plot, QUEST, QUESP, QUESTP and QUESTRA [10–12, 19, 32]. The Water Exchange (WEX) spectroscopy might be also a useful reference method for exchange rate determination [28, 33].

The simulations and experimental results showed slightly different ranges of applicability of the methods for the determination of exchange rate and the labile proton ratio. This can be explained as a result of systematic effects. Firstly, the simulated spin-lock pulse had an ideal rectangular form, which is never the case in reality. Besides, the simulated preparation pulses were realized through a simple rotation of the magnetization. In practice, a flip angle of these RF pulses is spatially dependent on, for instance, tissue attenuation. Secondly, a slight change of the saturation field strength, caused by the B_1 field inhomogeneities, leads to the varying saturation efficiency between pixels. Also, the B_0 inhomogeneities may cause non-negligible errors in quantitative CEST imaging [31]. In general, the Gaussian-shaped pulse irradiation scheme is considered to be more robust against field inhomogeneities than the spin-lock pre-saturation technique [24]. Further elements of uncertainty in the comparison of the experimental and simulated results are the longitudinal relaxation time T_{1s} and transversal relaxation time T_{2s} of the solute pool, used for simulations. Because of very short T_{2s}, a short echo-time spectroscopy is required in order to determine these parameters experimentally. Due to this technical limitation, we used values reported in the literature [31]. The influence of the T_{1s} time is relatively small. However, for extremely low exchange rates, a longer T_{1s} leads to more accurate results [15]. Moreover, simulation results presented by Sun et al. revealed that a variation of the T_{2s} plays only a subordinate role, as long as it can be reasonably estimated [15].

The results obtained for phantom 3 showed a linear dependency of the fractional concentration and the creatine concentration in solutions. A similar trend was reported by other groups [7, 20]. The comparison of the calculated labile proton ratios for phantom 3 showed a

systematic and partially significant overestimation of the results. In the case of Gaussian-shaped saturation pulses, it is consistent with the simulation findings. For the pulsed SL saturation, however, a slightly underestimated result was expected. The surprisingly overestimated values of the fractional concentration could be explained as a result of the underestimation of the exchange rates.

In the present work we assessed the applicability of the methods using creatine solution. Quantitative CEST analysis of other endogenous CEST agents or even multi-pool CEST systems could be the next step. Since exchange rates increase with increasing temperature, the pulsed SL saturation technique could be of particular relevance for imaging of slow and intermediate-exchanging protons at 3T. Another factor, which should be taken into account, is the signal-to noise ratio (SNR) of the MRI data. The Rician noise, which introduces a bias into MRI experiments, may be crucial to the quantitative CEST analysis, especially for in vivo applications [34, 35]. The apparent semi-solid molecular magnetization transfer (MT) and nuclear overhauser (NOE) effects also have to be considered [36, 37].

As an alternative to the pulsed saturation scheme, a method based on a continuous RF saturation scheme using a parallel RF transmission technique has been developed, that allows the use of arbitrarily long RF saturation pulses via amplifier alternation within the SAR and RF duty-cycle limits [38, 39].

Although the first in vivo applications of AREX metrics and the Ω-plot method at 3T scanner have been already reported, further development and tissue-oriented optimization is still necessary. Zaiss et al. applied AREX of APT (amide proton transfer) to calculate the absolute pH map of a rat brain with a stroke lesion. One limitation of this method is that the labile proton ratio has to be known in order to determine k_{sw} and, thus, the pH map [19]. In contrast, the Ω-plot method allows simultaneous measurements of the exchange rate and the labile proton ratio. Therefore, Zhou et al. performed in vivo quantitative CEST imaging using the Ω-plot method in the intervertebral discs (IVDs) in a porcine model on a 3T clinical scanner. The exchange rates determined from the quantitative analysis were closely correlated with the pH value in the IVDs, which was measured using a needle-shaped tissue pH probe. The most important limitation of the study was the acquisition time (30–40 min for one IVD) [40]. The quantitative CEST analysis requires long saturation times to achieve the steady-state and multiple CEST experiments with varying B_1 in the case of using the Ω-plot method. Thus, the new fast imaging techniques such as compressed sensing or parallel imaging are necessary to accelerate CEST acquisitions [41]. In addition to brain and cartilage, it might be also possible to quantify the CEST effects from small metabolites and their by-products in other human tissues such as kidney, liver or muscles.

Conclusion

A quantitative CEST data evaluation approach, enabling the determination of the labile proton ratio f of exchanging protons and their exchange rate k_{sw} is an important step in improving the quality of the CEST imaging. Up to now, quantitative CEST imaging was mostly performed at a high field strength (7T) using continuous wave (CW) saturation pulses. Although higher magnetic field strengths are beneficial to the CEST phenomenon, the commonly used field strengths on clinical MR usually do not surpass 3T. Furthermore, due to scanner specifications and specific absorption rate guidelines, only pulse train pre-saturation should be considered for the CEST imaging in clinical routine. The Ω-plot method for pulsed SL saturation has proved to be particularly promising for imaging of intermediate-exchanging protons with exchange rates between 50 and 530 Hz. In summary, our studies showed that quantitative pulsed-CEST MRI is capable of producing reasonable results at clinically available MR systems and remains promising for clinical translation.

Acknowledgements We thank M. Zaiss (German Cancer Research Center, Heidelberg, Germany) for providing CEST MRI pulse sequence used in this study.

Author contributions Stabinska: Protocol/project development, data management, data analysis. Cronenberg: Protocol/project development, data collection, data analysis. Wittsack: Protocol/project development. Lanzman: Protocol/project development. Müller-Lutz: Protocol/project development.

Compliance with ethical standards

Conflict of interest The authors declare that they have no conflict of interest.

Ethical approval This article does not contain any studies with human participants or animals performed by any of the authors.

Funding This study was supported by a Grant from the Forschungskommission of the Faculty of Medicine, Heinrich-Heine-University, Düsseldorf (Grant No: 13/2015).

Appendix 1

See Figs. 6 and 7 and Table 2.

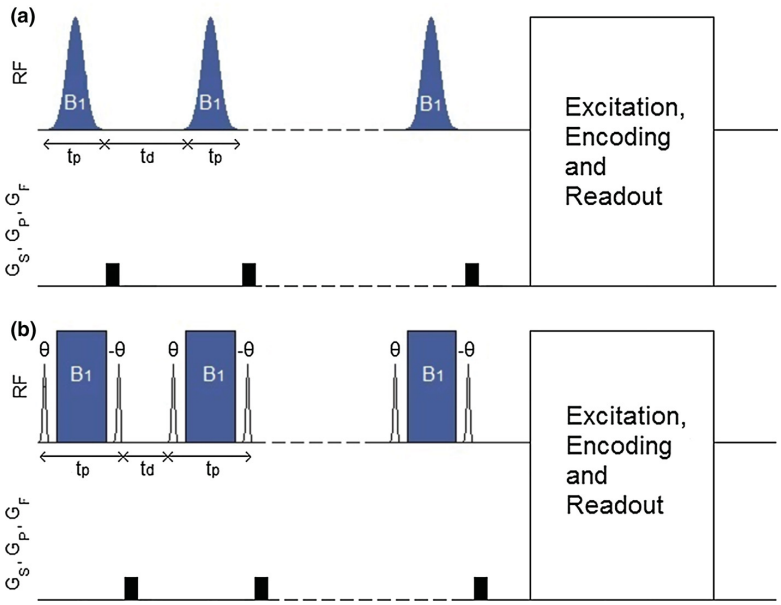

Fig. 6 A simplified schematic CEST pulse sequence diagram with a series of **a** Gaussian-shaped RF saturation pulses and **b** off-resonant spin-lock saturation pulses. Each saturation block consists of n pulses of average amplitude B_1 and duration t_p interleaved by delays t_d. Between the saturation pulses spoiling gradients in all three gradient dimensions are applied. After RF saturation a 2-D single-shot gradient echo sequence (GRE) was used for CEST image data acquisition. Diagram was created based on [22, 28]

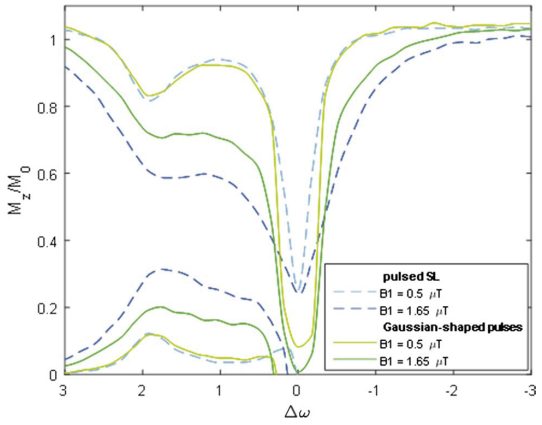

Fig. 7 Z-spectrum and AREX curves obtained with $B_1 = 0.5$ μT and $B_1 = 1.65$ μT using pulsed SL (*dashed blue lines*) and Gaussian-shaped saturation pulses (*solid green lines*). For the pulsed SL saturation, AREX yields higher contrast at higher B_1 compared to saturation with trains of Gaussian-shaped RF pulses

Table 2 Numerical simulation parameters

Quantitative CEST method	Saturation scheme	k_{sw}	B_1 variation (f = const)	f variation (B_1 = const)
AREX	Gaussian-shaped pulses Spin-lock pulses	1–300 Hz in steps of 1 Hz	0.1–5.0 μT in steps of 0.05 μT ($f = 2‰$)	–
AREX-based Ω-plot	Gaussian-shaped pulses Spin-lock pulses	10–500 Hz in steps of 10 Hz 10–1000 in steps of 10 Hz	Six datasets with linearly distributed RF amplitudes B_1 between 0.2 μT and a maximum B_1 value, which ranged between 1.6 and 4.6 μT in steps of 0.1 μT ($f = 2‰$)	0.05–5‰ in steps of 0.05‰ (B_1 = 0.25, 0.5, 1.0, 1.25, 1.65, 2.1 μT)

References

1. Ward KM, Aletras AH, Balaban RS (2000) A new class of contrast agents for MRI based on proton chemical exchange dependent saturation transfer (CEST). J Magn Reson 143:79–87
2. van Zijl PC, Yadav NN (2011) Chemical exchange saturation transfer (CEST): what is in a name and what isn't? Magn Reson Med 65(4):927–948
3. Vinogradov E, Sherry AD, Lenkinski RE (2013) CEST: from basic principles to applications, challenges and opportunities. J Magn Reson 229:155–172
4. Zhang S, Malloy CR, Sherry AD (2005) MRI thermometry based on PARACEST agents. J Am Chem Soc 127:17572–17573
5. Müller-Lutz A, Khalil N, Schmitt B, Jellus V, Pentang G, Oeltzschner G, Antoch G, Lanzman RS, Wittsack HJ (2014) Pilot study of Iopamidol-based quantitative pH imaging on a clinical 3T MR scanner. Magn Reson Mater Phy 27(6):477–485
6. Longo DL, Sun PZ, Consolino L, Michelotti FC, Uggeri F, Aime S (2014) A general MRI-CEST ratiometric approach for pH imaging: demonstration of in vivo pH mapping with Iobitridol. J Am Chem Soc 136(41):14333–14336
7. Wu R, Xiao G, Zhou IY, Ran C, Sun PZ (2015) Quantitative chemical exchange saturation transfer (qCEST) MRI–omega plot analysis of RF-spillover-corrected inverse CEST ratio asymmetry for simultaneous determination of labile proton ratio and exchange rate. NMR Biomed 28(3):376–383
8. Kim J, Wu Y, Guo Y, Zheng H, Sun PZ (2014) A review of optimization and quantification techniques for chemical exchange saturation transfer MRI toward sensitive in vivo imaging. Contrast Media Mol Imaging 10(3):163–178
9. Woessner DE, Zhang S, Merritt ME, Sherry AD (2005) Numerical solution of the Bloch equations provides insights into the optimum design of PARACEST agents for MRI. Magn Reson Med 53:790–799
10. McMahon MT, Gilad AA, Zhou J, Sun PZ, Bulte JW, van Zijl PC (2006) Quantifying exchange rates in chemical exchange saturation transfer agents using the saturation time and saturation power dependencies of the magnetization transfer effect on the magnetic resonance imaging signal (QUEST and QUESP): pH calibration for poly-L-lysine and a starburst dendrimer. Magn Reson Med 55(4):836–847
11. Dixon WT, Ren J, Lubag AJ, Ratnakar J, Vinogradov E, Hancu I, Lenkinski RE, Sherry AD (2010) A concentration-independent method to measure exchange rates in PARACEST agents. Magn Reson Med 63(3):625–632
12. Sun PZ (2012) Simplified quantification of labile proton concentration weighted chemical exchange rate (kws) with RF saturation time dependent ratiometric analysis (QUESTRA): normalization of relaxation and RF irradiation spillover effects for improved quantitative chemical exchange saturation transfer (CEST) MRI. Magn Reson Med 67(4):936–942
13. Sun PZ (2010) Simultaneous determination of labile proton concentration and exchange rate utilizing optimal RF power: radio frequency power (RFP) dependence of chemical exchange saturation transfer (CEST) MRI. J Magn Reson 202(2):155–161
14. Wu R, Liu CM, Liu PK, Sun PZ (2012) Improved measurement of labile proton concentration-weighted chemical exchange rate (kws) with experimental factor-compensated and T1-normalized quantitative chemical exchange saturation transfer (CEST) MRI. Contrast Media Mol Imaging 7(4):384–389
15. Sun PZ, Wang Y, Dai Z, Xiao G, Wu R (2014) Quantitative chemical exchange saturation transfer (qCEST) MRI–RF

spillover effect-corrected omega plot for simultaneous determination of labile proton fraction ratio and exchange rate. Contrast Media Mol Imaging 9(4):268–275
16. Sun PZ, Wang E, Cheung JS, Zhang X, Benner T, Sorensen AG (2011) Simulation and optimization of pulsed radio frequency (RF) irradiation scheme for chemical exchange saturation transfer (CEST) MRI—demonstration of pH-weighted pulsed-amide proton CEST MRI in an animal model of acute cerebral ischemia. Magn Reson Med 66(4):1042–1048
17. Schmitt B, Zaiss M, Zhou J, Bachert P (2011) Optimization of pulse train pre-saturation for CEST imaging in clinical scanners. Magn Reson Med 65:1620–1629
18. Sun PZ, Brenner T, Kumar A, Sorensen AG (2008) Investigation of optimizing and translating pH-sensitive pulsed-chemical exchange saturation transfer (CEST) imaging to a 3T clinical scanner. Magn Reson Med 60:834–841
19. Zaiss M, Xu J, Goerke S, Khan IS, Singer RJ, Gore JC, Gochberg DF, Bachert P (2014) Inverse Z-spectrum analysis for spillover-, MT-, and T1- corrected steady-state pulsed CEST-MRI–application to pH-weighted MRI of acute stroke. NMR Biomed 27(3):240–252
20. Meissner JE, Goerke S, Rerich E, Klika KD, Radbruch A, Ladd ME, Bachert P, Zaiss M (2015) Quantitative pulsed CEST-MRI using Ω-plots. NMR Biomed 28:1196–1208
21. Zaiss M, Bachert P (2013) Exchange-dependent relaxation in the rotating frame for slow and intermediate exchange–modeling off-resonant spin-lock and chemical exchange saturation transfer. NMR Biomed 26(5):507–518
22. Roeloffs V, Meyer C, Bachert P, Zaiss M (2014) Towards quantification of pulsed spinlock and CEST at clinical MR scanners: an analytical interleaved saturation-relaxation (ISAR) approach. NMR Biomed 28:40–53
23. Jin T, Aution J, Obata T, Kim SG (2011) Spin-locking versus chemical exchange saturation transfer MRI for investigating chemical exchange process between water and labile metabolite protons. Magn Reson Med 65:1448–1460
24. Jin T, Kim SG (2014) Advantages of chemical exchange-sensitive spin-lock (CESL) over chemical exchange saturation transfer (CEST) for hydroxyl- and amine-water proton exchange rates. NMR Biomed 27(11):1313–1324
25. Cobb JG, Li K, Xie J, Gochberg DF, Gore JC (2014) Exchange-mediated contrast in CEST and spin-lock imaging. Magn Reson Imaging 32(1):28–40
26. Yuan J, Zhou J, Ahuja AT, Wang YX (2013) MR chemical exchange imaging with spin-lock technique (CESL): a theoretical analysis of Z-spectrum using a two-pool $R_{1\rho}$ relaxation model beyond the fast-exchange limit. Phys Med Biol 57(24):8185–8200
27. Murase K, Tanki N (2011) Numerical solutions to the time-dependent Bloch equations revisited. Magn Reson Imaging 29(1):126–131
28. Goerke S, Zaiss M, Bachert P (2014) Characterization of creatine guanidinium proton exchange by water-exchange (WEX) spectroscopy for absolute-pH CEST imaging in vitro. NMR Biomed 27(5):507–518
29. Kim M, Gillen J, Landmann BA, Zhou J, van Zijl PC (2009) Water saturation shift referencing (WASSR) for chemical exchange saturation transfer experiments. Magn Reson Med 61(6):1441–1450
30. Müller-Lutz A, Matuschke F, Schleich C, Wickrath F, Boos J, Schmitt B, Wittsack HJ (2016) Improvement of water saturation shift referencing by sequence and analysis optimization to enhance chemical exchange saturation transfer imaging. Magn Reson Imaging 34(6):771–778
31. Sun PZ, Farrar CT, Sorensen AG (2007) Correction for artifacts induced by B0 and B1 field inhomogeneities in pH-sensitive chemical exchange saturation transfer (CEST) imaging. Magn Reson Med 58(6):1207–1215
32. Randtke EA, Chen LQ, Corrales LR, Pagel MD (2014) The Hanes-Woolf linear QUESP method improves the measurements of fast chemical exchange rates with CEST MRI. Magn Reson Med 71(4):1603–1612
33. Zhou J, Wilson DA, Sun PZ, Klaus JA, van Zijl PC (2004) Quantitative description of proton exchange processes between water and endogenous and exogenous agents for WEX, CEST and APT experiments. Magn Reson Med 51(5):945–952
34. Sun PZ, Wang E, Cheung JS (2012) Imaging acute ischemic tissue acidosis with pH-sensitive endogenous amide proton transfer (APT) MRI–correction of tissue relaxation and concomitant RF irradiation effects toward mapping quantitative cerebral tissue pH. Neuroimage 60(1):1–6
35. Gudbjartsson H, Patz S (1995) The Rician distribution of noisy MRI data. Magn Reson Med 34(6):910–914
36. Henkelman RM, Stanisz GJ, Graham SJ (2001) Magnetization transfer in MRI: a review. NMR Biomed 14:57–64
37. Jones CK, Huang A, Xu J, Edden RA, Schär M, Hua J, Oskolkov N, Zacà D, Zhou J, McMahon MT, Pillai JJ, van Zijl PC (2013) Nuclear overhauser enhancement (NOE) imaging in the human brain at 7T. Neuroimage 77:114–124
38. Keupp J, Togao O, Zhou J, Suzuki Y, Yoshiura T (2012) Optimization of saturation pulse length in parallel transmission based amide proton transfer MRI for oncology applications. Proc Int Soc Magn Reson Med 20:4258
39. Togao O, Hiwatashi A, Keupp J, Yamashita K, Kikuchi K, Yoshiura T, Yoneyama M, Kruiskamp MJ, Sagiyama K, Takahashi M, Honda H (2016) Amide proton transfer imaging of diffuse gliomas: effect of saturation pulse length in parallel transmission-based technique. PLoS One 11(5):e0155925
40. Zhou Z, Bez M, Tawackoli W, Giaconi J, Sheyn D, de Mel S, Maya MM, Pressman BD, Gazit Z, Pelled G, Gazit D, Li D (2016) Quantitative chemical exchange saturation transfer MRI of intervertebral disc in a porcine model. Magn Reson Med 76(6):1677–1683
41. Heo HY, Zhang Y, Leen DH, Jiang S, Zhao X, Zhou J (2016) Accelerating chemical exchange saturation transfer (CEST) MRI by combining compressed sensing and sensitivity encoding techniques. Magn Reson Med 77:779–786

Appendix B

Publication 2

The results of **study 2** have been published in:

Stabinska J, Neudecker P, Ljimani A, Wittsack HJ, Lanzman RS, Müller-Lutz A. Proton exchange in aqueous urea solutions measured by water-exchange (WEX) NMR spectroscopy and chemical exchange saturation transfer (CEST) imaging in vitro. Magn Reson Med. 2019; 82:935–947. doi: 10.1002/mrm.27778

Impact factor (2019): 3.858

Personal contribution: 80% (data acquisition, data analysis, data interpretation, manuscript writing, manuscript revision)

Received: 25 September 2018 | Revised: 6 March 2019 | Accepted: 28 March 2019

DOI: 10.1002/mrm.27778

FULL PAPER

Magnetic Resonance in Medicine

Proton exchange in aqueous urea solutions measured by water-exchange (WEX) NMR spectroscopy and chemical exchange saturation transfer (CEST) imaging in vitro

Julia Stabinska[1] | Philipp Neudecker[2,3] | Alexandra Ljimani[1] | Hans-Jörg Wittsack[1] | Rotem Shlomo Lanzman[1] | Anja Müller-Lutz[1]

[1]Department of Diagnostic and Interventional Radiology, Medical Faculty, Heinrich Heine University Düsseldorf, Dusseldorf, Germany

[2]Institute of Physical Biology, Heinrich Heine University Düsseldorf, Dusseldorf, Germany

[3]Institute of Complex Systems: Structural Biochemistry (ICS-6), Forschungszentrum Jülich, Julich, Germany

Correspondence
Julia Stabinska, Department of Diagnostic and Interventional Radiology, Medical Faculty, Heinrich Heine University Düsseldorf, Moorenstr. 5, 40225 Düsseldorf, Germany.
E-mail: Julia.Stabinska@med.uni-duesseldorf.de

Purpose: To characterize the proton exchange in aqueous urea solutions using a modified version of the WEX II filter at high magnetic field, and to assess the feasibility of performing quantitative urea CEST MRI on a 3T clinical MR system.

Methods: In order to study the dependence of the exchange-rate constant k_{sw} of urea as a function of pH and T, the WEX-spectra were acquired at 600 MHz from urea solutions in a pH range from 6.4 to 8.0 and a temperature range from $T = 22°C$ to 37°C. The CEST experiments were performed on a 3T MRI scanner by applying a train of 50 Gaussian-shaped pulses, each 100-millisecond long with a spacing of 100 milliseconds, for saturation. Exchange rates of urea were calculated using the (extended) AREX metric.

Results: The results showed that proton exchange in aqueous urea solutions is acid and base catalyzed with the rate constants: $k_a = (9.95 \pm 1.1) \times 10^6$ l/(mol·s) and $k_b = (6.21 \pm 0.21) \times 10^6$ l/(mol·s), respectively. Since the urea protons undergo a slow exchange with water protons, the CEST effect of urea can be observed efficiently at 3T. However, in neutral solutions the exchange rate of urea is minimal and cannot be estimated using the quantitative CEST approach.

Conclusions: By means of the WEX-spectroscopy, the kinetic parameters of the proton exchange in urea solutions have been determined. It was also possible to estimate the exchange rates of urea in a broad range of pH values using the CEST method at a clinical scanner.

KEYWORDS
CEST, exchange rate, proton exchange, urea, urCEST, WEX

1 | INTRODUCTION

Urea is the major end-product of protein catabolism and serves an important role in the maintenance of pH homeostasis in mammals.[1,2] It is formed in the liver from ammonia, and later transported in the blood to the kidneys for excretion in the urine.[3,4] Diseases that compromise the function of the kidney are often associated with reduced urea elimination and consequently its increased concentration in blood, as measured by the blood urea nitrogen (BUN) test.[5] To assess

the structural changes in kidneys, well-established imaging techniques such as ultrasound (US), computed tomography (CT), and magnetic resonance tomography (MRI) are performed. Nevertheless, they usually do not provide adequate functional information.[6]

Chemical exchange saturation transfer (CEST) is a novel mechanism of MRI contrast that may overcome this limitation, since it has been shown to be sensitive to the concentrations of the endogenous metabolites and microenviromental properties such as pH and temperature.[7-10] Urea is a potentially attractive CEST agent for in vivo use. Although the normal blood urea level is relatively low (5-10 mM), the urea concentration in the urine may be 20-100 times higher than in the blood in humans, as reported in Ref. [[11]] Urea is an amide with two $-NH_2$ groups joined by a carbonyl ($C = O$) functional group.[12] Already in 1998, Guivel-Sharen et al. identified urea as a major contributor to the kidney/urine chemical exchange at ca. 1 ppm (with water proton frequency defined as 0 ppm).[13] Two years later, Dagher et al. were able to produce a urea distribution map in vivo at 1.5 T using CEST MRI.[14] Apart from an ISMRM abstract in 2015,[15] no further studies on urea-weighted CEST (urCEST) at a clinical MRI system have been published.

Knowledge about the chemical shift, exchange rate, and relaxation properties of urea leads to better understanding of the saturation transfer effects in the human kidney in vivo. Because many kidney diseases alter pH and urea gradients in kidney, an implementation of pH-sensitive CEST imaging might be of great interest particularly in the clinical context.[7,16] In this study, we characterize the proton exchange properties of urea with water using water exchange spectroscopy (WEX II)[17] at ultrahigh magnetic field, and evaluate the feasibility of performing quantitative urea CEST analysis at 3T. In particular, we determine the chemical exchange rates k_{sw} between urea amide protons s and water w as a function of pH, concentration, and temperature by means of WEX spectroscopy and CEST experiments.

Moreover, in order to examine the specificity of the urea-weighted CEST imaging in kidney, we study the CEST effect of other important kidney metabolites, eg, creatinine, ammonia, hippuric acid, and citric acid at different pH values.[18,19] Eventually, we investigate the contribution of the urCEST to the total CEST effect in urine.

2 | METHODS

2.1 | Preparation of the aqueous urea solutions

For WEX experiments, six aqueous model solutions containing 250 mM urea (≥99.5% cryst. urea, Carl Roth, Karlsruhe, Germany), 50 mM sodium/potassium phosphate buffer (≥99% disodium hydrogen phosphate, and ≥99.5% potassium dihydrogen phosphate, Carl Roth, Karlsruhe, Germany) and 5% (v/v) deuterium oxide (D_2O, 99.8 atom % D, Carl Roth, Karlsruhe, Germany) for the field-frequency lock were prepared at different pH = (6.39, 6.56, 6.96, 7.38, 7.72, 7.97) and measured at temperature $T = 37.0$°C. The samples with pH = 6.56 and pH = 7.97 were additionally measured at varied temperatures T = (22.0°C, 27.0°C, 32.0°C, 37.0°C).

For CEST studies, sixteen 50 ml aqueous solutions with 250 mM urea concentration were mixed with 50 mM Na/K phosphate buffer at pH = (5.66, 5.72, 5.93, 6.12, 6.20, 6.37, 6.54, 6.86, 7.00, 7.20, 7.37, 7.65, 7.80, 8.02, 8.20, 8.41). In addition, four samples containing different urea concentration c_s = (10 mM, 25 mM, 50 mM, 100 mM) at pH 7.60 were prepared.

The other studied metabolites were: creatinine, ammonia, hippuric acid, citric acid, taurine, creatine, histidine, glucose, glutamine, myo-inositol, alanine, lysine, allantoin, threonine, lactate, sorbitol, glutamic acid, choline, and glycogen. The concentration of most compounds was 100 mM, and the remainder determined by their solubility in the sample buffer. Each phantom consisted of four tubes containing model solution dissolved in 50 mM Na/K phosphate buffer at pH = (6.2, 6.6, 7.0, 7.4). Additionally, individual and mixed aqueous solutions of 180 mM urea, 15 mM creatinine, and 1 mM creatine, corresponding to the normal concentrations of these metabolites in urine, were prepared. In addition, an urine sample was collected from a healthy volunteer. The pH value of the model mixture and the urine sample were: 5.97 and 5.90 at $T = 37$°C, respectively.

The temperature of the model solutions during the measurements was kept constant $T = (37 \pm 1)$°C by using an MR-compatible cooling box.

2.2 | WEX experiments

The WEX spectra were acquired on a Bruker Avance III HD 600-MHz NMR spectrometer (Bruker, Ettlingen, Germany) equipped with a cryogenically cooled quadruple resonance probe with z-axis pulsed field gradient capabilities. The sample temperature was calibrated using methanol-d_4.[20] The exchange of water protons with urea was monitored with the pulse sequence shown in Figure 1 using 33 different mixing times (T_m) ranging from 20 milliseconds to 2000 milliseconds. For each mixing time, 32 transients were recorded with a recycle delay of 4.7 seconds. The resulting spectra were processed using NMRPipe and NMRDraw[21] and the ^{1}H resonance of urea was integrated.

2.3 | CEST experiments

All CEST experiments were performed on the 3T whole body MR clinical scanners (Magnetom Trio and Magnetom Prisma, Siemens Healthineers, Erlangen, Germany). Z-spectra were obtained using presaturated gradient-echo imaging with

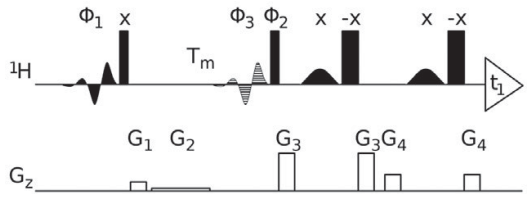

FIGURE 1 WEX II pulse sequence with excitation sculpting and water flip-back. Narrow and wide bars are hard rectangular 90° and 180° pulses, respectively, applied at maximum permissible amplifier power with the phase indicated above each pulse. Water-selective 90° pulses have an E-BURP-1 shape[39] and a duration of 12.0 milliseconds (at 600 MHz). Water-selective 180° pulses have a shape corresponding to the central lobe of a sinc function and a duration of 4.0 milliseconds. The basic phase cycle of the WEX II sequence is ϕ_1: $x, -x, x, -x$; ϕ_2: $x, x, -x, -x$; ϕ_3: $x, -x, -x, x$; receiver: $x, -x, -x, x$ and is expanded by EXORCYCLE phase cycling of the 180° pulses in the excitation sculpting sequence. The pulsed field gradients are G_1: 10 G/cm, 1.0 milliseconds; G_2: 1 G/cm; G_3: 43 G/cm, 0.5 milliseconds; G_4: 19 G/cm, 0.5 milliseconds

the following parameters: $FOV = 130 \times 130\,mm^2$, matrix size: 128×128, slice thickness = 5.0 mm, repetition time $T_R = 7.7$ milliseconds and echo time $T_E = 3.61$ milliseconds. In the urCEST experiments, presaturation was achieved using 50 Gaussian-shaped pulses with low RF saturation power of $B_1 = 1.0\mu$ T, pulse duration $t_{pd} = 100$ milliseconds and interpulse delay $t_{ipd} = 100$ milliseconds (duty cycle $DC = 50\%$, total saturation time $T_{sat} = 9.9$seconds). Forty-three saturated images at evenly distributed frequency offsets between ± 4 ppm and an unsaturated image at 300 ppm were acquired. To determine B_0 maps using the water saturation shift referencing method (WASSR),[22] a single Gaussian-shaped pulse with RF saturation power of $B_1 = 0.1\,\mu$T and pulse duration $t_{pd} = 56$ milliseconds was applied. The WASSR z-spectra were obtained at 42 offsets between −1 ppm and 1 ppm. Additionally, T1-weighted images were measured by a turbo inversion recovery sequence. Altogether, 12 contrasts at different inversion delays (TI) ranging from 25 milliseconds to 5 seconds were fitted to calculate T_1 maps. The same measurement protocol was applied to acquire the CEST signals in the phantom including mixed solution of urea, creatinine, and creatine as well as in the urine sample.

Further phantom experiments were performed using 20 Gaussian-shaped pulses with three different RF amplitudes, $B_1 = (0.8, 1.2, 1.6)\,\mu$T and pulse duration $t_{pd} = t_{ipd} = 100$ milliseconds. Z-spectra were acquired at 45 frequency offsets between −6 and 6 ppm.

2.4 | Data analysis

Post-processing was performed using in-house written programs in MATLAB (Mathworks, Natick, Massachusetts). The T_1 maps were obtained by pixel-by-pixel least-squares fitting of the signal equation $I = I_0 \cdot [1 - 2 \cdot \exp(-TI/T_1)]$, where I is the signal intensity and TI is the inversion time. The exchange rates of urea were calculated as described in the following sections.

2.5 | Determination of k_a and k_b for urea by WEX

As in standard amides, proton exchange in urea solutions is acid and base catalyzed and therefore strongly pH dependent[23,24]:

$$k_{sw} = k_b \cdot 10^{pH - pK_w} + k_a \cdot 10^{-pH} + k_0 \tag{1}$$

where k_b, k_a and k_0 (in l/(mol·s)) are rate constants for the base-, acid- and water-catalyzed protolysis, respectively. The rate of the spontaneous reaction (k_0) is very slow compared to acid and base catalyses, and thus assumed to be negligible.[24] The pK_w refers to the negative decadic logarithm of the ionization constant, which is temperature dependent according to the solution of the van't Hoff equation[25,26]:

$$pK_w(T) = pK_w(T_0) - \left(\frac{\Delta H_R^0}{R \cdot \ln(10)}\right)\left(\frac{1}{T_0} - \frac{1}{T}\right) \tag{2}$$

$pK_w(T_0)$ here refers to the logarithm of the water-ion product at temperature $T_0 = 25°C$, $\Delta H_R^0 = 55.84$ kJ/mol is the standard reaction enthalpy for the self-dissociation of water and $R = 8.314$ J/(mol K) is the gas constant.[25,26] Thus, we assumed $pK_w = 13.617$ at $T = 37°C$. The urea signal intensity $S_s(T_m)$ as a function of the mixing time T_m is given by[26]:

$$S_s(T_m) = \underbrace{\frac{k_{ws} M_{zw}(0)}{k_{sw} + R_{1s} - R_{1w}}}_{C} \left[e^{-R_{1w} \cdot (T_m - T_{WFB})} - e^{-(k_{sw} + R_{1s}) \cdot (T_m - T_{WFB})}\right] \tag{3}$$

where R_{1w}, R_{1s} are the longitudinal relaxation rates of the water and solute pool, respectively; k_{sw} is the chemical exchange rate between solute s and water pool w and k_{ws} is the back-exchange rate; $M_{zw}(0)$ is the z magnetization of the water protons at the beginning of the mixing period. The $k_{sw} + R_{1s}$ values were obtained from a fit of Equation 3 to the measured urea signal integrals $S_s(T_m - T_{WFB})$ at any given pH and temperature in MATLAB, where TWFB is a variable fitting parameter introduced to account for the effects of the water flip-back pulse at the end of the mixing period (see below). Eventually, the k_b and k_a rates at given temperature were estimated by bi-exponential fit of the measured $k_{sw} + R_{1s}$ values with the following equation:

$$k_{sw} + R_{1s} = k_b \cdot 10^{pH - pK_w} + 10^{-pH} + R_{1s} \tag{4}$$

Furthermore, the activation energies $E_{A,b}$ and $E_{A,a}$ of, respectively, base- and acid-catalyzed reactions were calculated by fitting the measured $k_{sw} + R_{1s}$ values at pH 7.97 and pH 6.56 as a function of temperature. It was assumed that at pH 7.97, the proton exchange with water is dominantly base catalyzed, hence[27]:

$$k_{sw} + R_{1s} = k_b(310.15\,\mathrm{K}) \cdot \left[\frac{\mathrm{mol}}{l}\right] \cdot 10^{pH-14+\frac{\Delta H^0_R}{R\cdot\ln(10)}\left(\frac{1}{298.15\,\mathrm{K}}-\frac{1}{T}\right)+\frac{E_{A,b}}{R\cdot\ln(10)}\left(\frac{1}{310.15\mathrm{K}}-\frac{1}{T}\right)} + R_{1s} \quad (5)$$

Similarly, at pH 6.56, the exchange process between water and amide protons of urea is mainly acid catalyzed, and thus[27]:

$$k_{sw} + R_{1s} = k_a(310.15\,\mathrm{K}) \cdot \left[\frac{\mathrm{mol}}{l}\right] \cdot 10^{-pH+\frac{E_{A,a}}{R\cdot\ln(10)}\left(\frac{1}{310.15\mathrm{K}}-\frac{1}{T}\right)} + R_{1s} \quad (6)$$

where $k_b(310.15\,\mathrm{K})$ and $k_a(310.15\,\mathrm{K})$ are the obtained rate constants at $T = 310.15$ K. The R_{1s} was assumed to be independent of temperature.[27]

2.6 | Determination of k_{sw} for urea by CEST

Recently, several theoretical approaches of quantifying proton exchange rates from data obtained in CEST experiments were proposed,[28-33] especially a novel magnetization transfer (MT) ratio called MTR_{Rex}, which eliminates spillover effect and semi-solid macromolecular magnetization transfer, was introduced by Zaiss et al.[34]:

$$MTR_{Rex} = \frac{1}{Z_{lab}} - \frac{1}{Z_{ref}} = \frac{R_{ex}\cdot DC}{R_{1w}} \quad (7)$$

where $Z_{lab} = Z(+\Delta\omega)$ is the label scan around the resonance of the CEST pool s, $Z_{ref} = Z(-\Delta\omega)$, the reference scan at the opposite frequency with respect to water, R_{ex} refers to the exchange-dependent relaxation in the rotating frame and R_{1w}, is the relaxation rate of the water pool w. Duty cycle, $DC = t_{pd}/(t_{ipd} + t_{pd})$, is determined by the pulse duration t_{pd} and the inter-pulse delay t_{ipd}. The MTR_{Rex} metric can be extended to an apparent exchange-dependent relaxation metric, $-AREX$:

$$AREX = MTR_{Rex}\cdot R_{1w} \quad (8)$$

More recently, Roeloffs et al. demonstrated that in the case of exchange rates that are small with respect to the inter-pulse delay, modeling magnetization transfer during the pauses between the RF pulses might be crucial.[35] In their theoretical model, they assume bi-exponential dynamics of the magnetization in the water pool during the inter-pulse delay (ISAR2), instead of a mono-exponential recovery with rate R_{1w} (ISAR1), as had been previously presumed.[36] As a result, the MTR_{rex} metric has to be extended by an additional term[35]:

$$MTR_{Rex} = \frac{1}{Z_{lab}} - \frac{1}{Z_{ref}} = \frac{R_{ex}\cdot DC}{R_{1w}}\cdot\left(1+\frac{1-R_{1w}t_{ipd}}{t_{pd}k_{sw}}\right) \quad (9)$$

In the large shift limit (LS) (i) $\delta\omega_s \to \infty$ and in the full saturation limit (FS) (ii) $\omega_1 \gg R_{2s} + k_{sw}$, when applying RF pulse at the CEST pool s resonance, $R_{ex} = f_s \cdot k_{sw}$ and hence[34]:

$$k_{sw} = \frac{MTR_{Rex}\cdot R_{1w}}{DC\cdot f_s} \quad (10)$$

where k_{sw} describes the exchange rate of urea, f_s the proton fraction (see below), R_{2s} the transverse relaxation rate of the CEST pool s, ω_1 the RF irradiation amplitude and $\delta\omega_s$ corresponds to the frequency offset of pool s. The proton fraction is given by[34]:

$$f_s = \frac{n_s}{n_w}\cdot\frac{c_s}{c_w} \quad (11)$$

c_i and n_i are the concentration and number of exchangeable protons per molecule of pool i ($i = s$ or w). It is assumed that $c_w = 55$ M and $n_w = 2$.

3 | RESULTS

3.1 | Implementation of the WEX II pulse sequence

For the measurement of water exchange rates we used a phase-cycled difference experiment based on water-selective inversion using the WEX II filter sequence with a 1D ^{1}H readout as described by Mori et al.[17] Because the broad ^{1}H resonance of urea (5.45 ⋯ 6.05 ppm) is separated from the ^1H_2O resonance (between 4.66 ppm and 4.80 ppm in the temperature range studied here) by only 0.65 ppm (390 Hz at 600 MHz) (Figure 2), such an experiment requires not only highly frequency-selective water inversion but also a 1D ^{1}H readout with excellent water suppression with water flip-back, a uniform excitation profile with an extremely narrow transition region near the ^1H_2O resonance, and an exceptionally flat baseline. To this end, the 3-9-19-WATERGATE water suppression scheme used in the original WEX II sequence [17] was replaced by an excitation sculpting[37] readout with water flip-back[38] (Figure 1). Water-selective excitation and water flip-back was achieved by 12.0 millisecond self-refocusing E-BURP-1[39] 90° pulses, water-selective refocusing by 4.0 milliseconds 180° pulses with a shape corresponding to the central lobe of a sinc(x) = sin(x)/x function. Simulations based on the Bloch equations and control experiments were used to establish that these pulses are sufficiently frequency selective that their effect on the ^{1}H resonance of urea is negligible. In brief, the initial combination of water selective and hard 90° pulses in Figure 1 selectively aligns the water magnetization along either the negative (−z) or the positive (+z) longitudinal axis in successive transients. Solute magnetization is rotated into the transverse plane and dephased by the crushing gradient G_1. The differential transfer of the (negative or positive) longitudinal magnetization of water protons

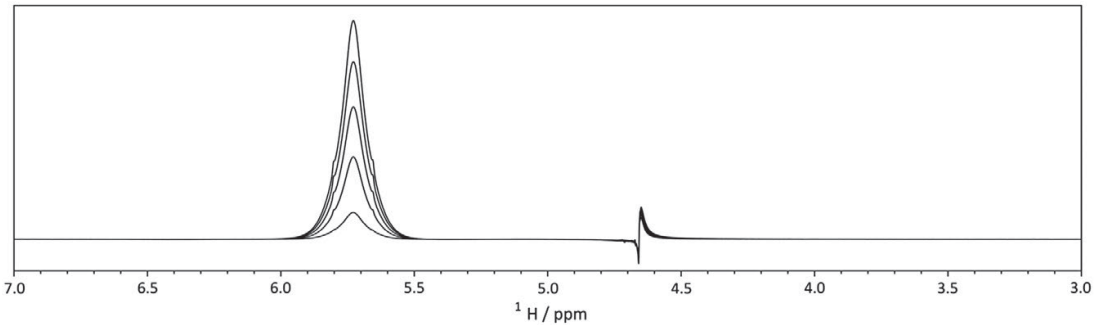

FIGURE 2 Overlay of the 1D ^{1}H WEX II spectra recorded using the pulse sequence shown in Figure 1 at pH 6.96 and 37.0°C with T_m = 20.0 milliseconds, 40.0 milliseconds, 60.0 milliseconds, 80.0 milliseconds, and 100.0 milliseconds (from bottom to top). Due to scalar relaxation of the second kind caused by the fast quadrupolar relaxation of the most abundant nitrogen isotope ^{14}N the urea ^{1}H resonance is very broad[61]; the ^{15}N satellites cause a doublet separated by the scalar coupling $^1J_{NH}$ which is visible as shoulders on the main ^{1}H resonance of urea. Excitation sculpting with water flip-back results in highly efficient suppression of the residual ^1H_2O resonance at approximately 4.66 ppm with a very flat baseline. Magnetization transfer to the urea resonance due to water exchange is approximately linear with the effective mixing time in the initial slope regime, but due to the effects of the water flip-back pulse in Figure 1 the effective mixing time ($T_{m-T_{WFB}}$) is systematically shorter than T_m, which is reflected in the disproportionally weak intensity of the urea resonance for T_m = 20.0 milliseconds

to other metabolites during the mixing time, T_m, in successive scans is obtained by phase cycling the pulses of the WEX II filter together with the receiver.[17] A weak gradient (G_2) is applied during the mixing time to prevent radiation damping.[17] Any longitudinal magnetization transferred to the solute is then detected with a 1D ^{1}H pulse sequence with excitation sculpting[37] preceded by a water flip-back pulse[38] to achieve excellent water suppression and a very flat spectral baseline (Figure 2). While this sequence preserves most of the salient features of the original WEX II sequence,[17] we prefer to apply the long (12.0 milliseconds) water flip-back pulse at the end of T_m before the hard 90° readout pulse in order to keep the excitation sculpting gradient double echo short enough to limit transverse relaxation and any homonuclear scalar coupling evolution. As a result of the complex trajectory of the water magnetization during this water flip-back pulse, the effective mixing time is somewhat shorter than T_m and no longer known a priori, but has to be corrected a posteriori by a variable parameter during data analysis. An important technical consideration—especially on modern high-field instruments with highly sensitive cryoprobes—is the effect of radiation damping, which opposes water-selective pulses that rotate the magnetization away from the positive longitudinal axis ("flip-down") but reinforces water-selective pulses that rotate the magnetization toward the positive longitudinal axis ("flip-up"). As a result, flip-down and flip-up water-selective pulses are significantly different and have to be calibrated independently.[40] The water-selective WEX II excitation pulse in Figure 1 has to be calibrated as a flip-down pulse because it rotates the magnetization from the positive (+z) longitudinal axis into the transverse plane. By contrast, the water flip-back pulse at the end of T_m (hatched in Figure 1) rotates the magnetization from either −z or +z into the transverse plane and therefore alternates between a flip-up and flip-down pulse, respectively, in successive transients. If only flip-down pulses are used for the sake of convenience, water flip-back will be incomplete and it is important to choose a recycle delay long enough for longitudinal relaxation of ^1H_2O between successive transients. As an alternative to the 1D ^{1}H readout presented in Figure 1, it is also straightforward to take advantage of the much sharper linewidth of the $^{15}NH_2$ groups of urea at natural abundance by combining the WEX II filter with a [^{1}H, ^{15}N] HSQC readout sequence with gradient coherence selection and water flip-back[41] if the signal-to-noise ratio is not limiting.

3.2 | Determination of the exchange rate constants k_a and k_b and the activation energies $E_{A,a}$ and $E_{A,b}$ of urea by WEX

The chemical shift of the urea amide protons in the WEX spectra is δ = 5.73 ppm at pH 6.96 and T = 37.0°C. The experimentally determined signal intensities of urea are in an excellent agreement with the fitted function $S_s(T_m)$ (Equation 3) (Figure 3) proven by mean fit quality of R^2 = 1.0.[42] Similarly, the $k_{sw} + R_{1s}$ values obtained from six measured samples at different pH match well the fitted function $k_{sw}(pH) + R_{1s}$ (Equation 4) (Table 1, Figure 4). With a fit quality of R^2 = 0.996, the estimated acid- and base- catalyzed exchange rate constants of urea at 37.0°C (310.15 K) are $k_a = (9.95 \pm 1.11) \times 10^6$ l/(mol·s) and $k_b = (6.21 \pm 0.21) \times 10^6$ l/(mol·s), respectively. The assumption of bi-exponential dependence of the urea exchange rate on pH is thus clearly verified. It is worth noting that the acid-catalyzed rate constant is much faster than the base-catalyzed rate constant. Using the calculated k_a and k_b values, it is possible to extrapolate the k_{sw} for any pH value (Table 2).

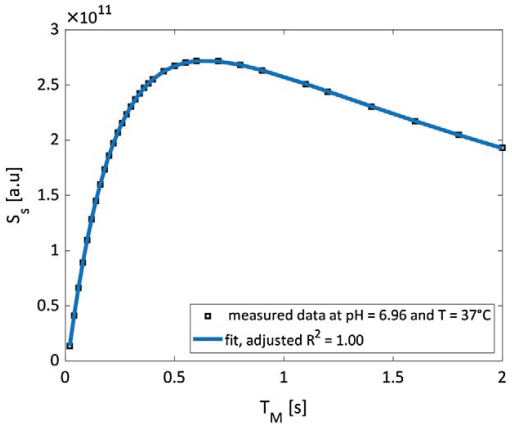

FIGURE 3 Integrated signal intensities S_s of the urea peaks (squares) at pH = 6.96 and T = 37.0°C as a function of mixing time T_m, and the fit function $S_s(T_{m-T_{WFB}})$ (Equation 3) (solid blue line). The quality of the fit was R^2 = 1.00

TABLE 1 $k_{sw} + R_{1s}$ [1/s] and R_{1w} [1/s] values in urea aqueous solutions (c_s = 250 mM) measured by WEX at different pH and temperatures. The standard errors are approximately 0.04% and R^2 = 1.0

pH	T [°C]	R_{1w} [1/s]	$k_{sw} + R_{1s}$ ([1/s])
6.39	37.0	0.29	6.22
6.56	22.0	0.39	2.92
6.56	27.0	0.35	3.56
6.56	32.0	0.33	4.31
6.56	37.0	0.31	5.26
6.96	37.0	0.30	4.63
7.38	37.0	0.30	5.82
7.72	37.0	0.30	9.63
7.97	22.0	0.38	3.78
7.97	27.0	0.35	6.14
7.97	32.0	0.32	9.93
7.97	37.0	0.30	16.19

The activation energies for base- and acid-catalyzed proton exchange in urea solution are $E_{A,b}$ = 43.52 ± 9.56 kJ/mol (quality of the fit: R^2 = 0.995) and $E_{A,a}$ = 79.13 ± 15.87 kJ/mol (quality of the fit: R^2 = 0.975). The Arrhenius plot ($\ln(k_{sw})$ against $1/T$) gives, as expected, a straight line (Figure 4).

3.3 | Determination of the exchange rates k_{sw} of urea by CEST

The CEST peak from urea is located at ca. 1 ppm with respect to the water resonance, which is arbitrarily set at 0 ppm. After correction of the MTR_{Rex} data for effects of T_1 relaxation (by multiplying with the R_{1w} maps), we obtained the apparent exchange-related relaxation metric (AREX) (Equation 8). The bi-exponential dependence of the AREX values on pH confirms that the proton exchange in aqueous urea solutions is acid and base catalyzed (Figure 5). By varying the urea concentration c_s at fixed pH = 8.04 and T = (37 ± 1)°C, we could also demonstrate that the (corrected) AREX is linearly proportional to the urea concentration (R^2 = 0.991) (Figure 5).

Using Equation 11 and the $k_{sw,ref}$ values determined by extrapolation of Equation 4 with the rate constants k_a and k_b measured by means of WEX spectroscopy, we were able to calculate the proton fraction f_s and thus the number of

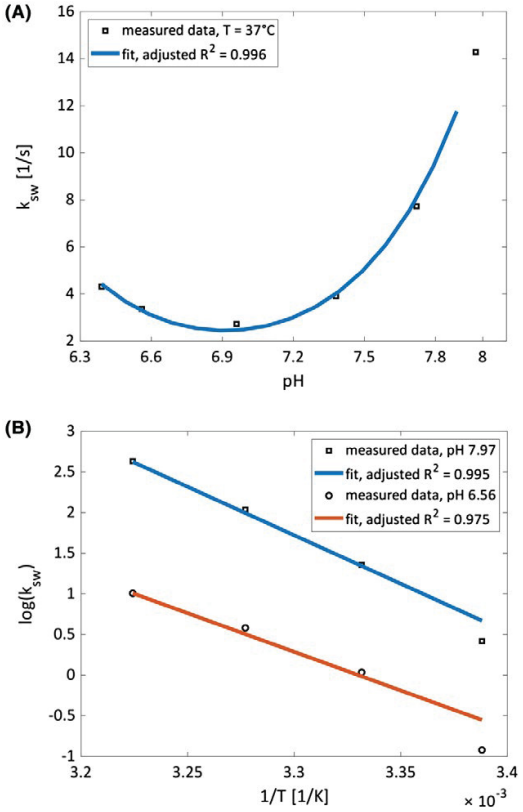

FIGURE 4 Determined k_{sw} (squares) values of urea as a function of (A) pH and (B) temperature. A, Temperature T = 37.0°C and urea concentration c_{urea} = 250 mM were fixed. Data were fitted using Equation 4 (solid blue line) yielding the following parameters: k_b = (6.21 ± 0.21) × 10^6 l/mol ·s, k_a = (9.95 ± 1.11) × 10^6 l/mol ·s and R_{1s} = (1.90 ± 0.31) s^{-1} (R^2 = 0.996). B, Arrhenius plot from data measured at fixed urea concentration c_{urea} = 250 mM at pH 7.97 (square) and pH 6.56 (circle). Data were fitted using Equation 5 (solid blue line) and 6 (solid yellow line) yielding the following values of activation energies: $E_{A,b}$ = 43.52 ± 9.56 kJ/mol (R^2 = 0.995) and $E_{A,a}$ = 79.13 ± 15.87 kJ/mol (R^2 = 0.975)

TABLE 2 Exchange rate k_{sw} [1/s] values in urea model solutions (c_s = 250 mM) obtained from CEST at different pH and $k_{sw,ref}$ estimated from WEX by extrapolation of Equation [5]

pH	T [°C]	k_{sw} [1/s]	$k_{sw,ref}$ [1/s]
5.66	37 ± 1	21.10 ± 2.80	21.84
5.72	37 ± 1	19.92 ± 2.20	19.04
5.93	37 ± 1	14.38 ± 2.33	11.82
6.12	37 ± 1	7.87 ± 2.25	7.75
6.20	37 ± 1	3.88 ± 1.88	6.51
7.37	37 ± 1	1.04 ± 2.10	4.60
7.65	37 ± 1	5.66 ± 2.41	6.92
7.80	37 ± 1	8.07 ± 1.85	9.61
8.02	37 ± 1	15.68 ± 2.31	15.80
8.20	37 ± 1	23.26 ± 3.14	23.83
8.41	37 ± 1	34.11 ± 3.81	38.58

labile protons in urea n_s (Equation 11). Using the AREX maps of eight model solutions at pH = (5.66, 5.72, 5.92, 6.12, 7.8, 8.02, 8.20, 8.41), we obtained $n_s = 4.10 \pm 0.21$. This result suggests that urea possesses four labile protons. Finally, employing the Equation 10 with $f_s = 4$, the exchange rate k_{sw} maps of urea can be calculated (Figure 5). The k_{sw} derived experimentally from CEST data agree well with the reference values $k_{sw,ref}$, at pH values below 6.2 and above 7.4 at 37°C (Figure 5, Table 2). In the neutral solutions the exchange rate of urea is minimal and could not be accurately estimated from the CEST data. In general, it is possible to determine the pH maps by solving the Equation 1 with the k_{sw} values calculated from the CEST data. However, in the case of bi-exponential function we obtain two real solutions and without additional information, we cannot univocally decide which of the two possible pH values is "correct".

3.4 | Assessment of pH dependence of the CEST effect of other kidney metabolites

In order to identify major kidney metabolites, which possess exchangeable protons and may generate an experimentally measurable CEST effect under physiological condition, results from animal[18] and human studies[43] on kidney tissues as well as the Urine Metabolome Database[19] were analyzed.

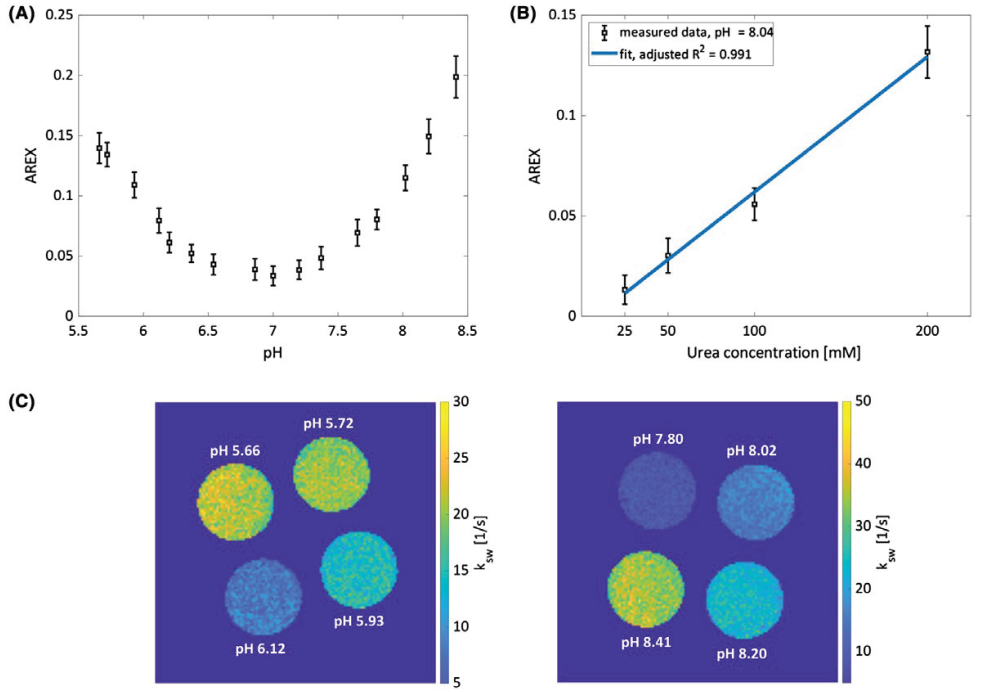

FIGURE 5 Apparent exchange-dependent relaxation (AREX) as a function of (A) pH and (B) urea concentration c_{urea} and (C) two exemplary exchange rates k_{sw} maps. A, Temperature T = (37 ± 1)°C and urea concentration c_{urea} = 250 mM were fixed. The AREX values were obtained from Equations 8 and 9. B, Temperature T = (37 ± 1)°C and pH_{fixed} = 8.04 were fixed. Data were fitted (solid blue line) using Equations 8-11. The fit quality was: R^2 = 0.991. C, The k_{sw} maps for two sets of the urea model solutions: #1 (pH 5.66, c_s = 250 mM), #2 (pH 5.72, c_s = 250 mM), #3 (pH 5.93, c_s = 250 mM), #4 (pH 6.12, c_s = 250 mM), #5 (pH 7.80, c_s = 250 mM), #6 (pH 8.02, c_s = 250 mM), #7 (pH 8.20, c_s = 250 mM), #8 (pH 8.41, c_s = 250 mM) obtained from the quantitative CEST experiments at T = 37°C

TABLE 3 An overview of important kidney metabolites and their CEST properties

Compound	Functional group	δ_s [ppm][a]	k_{sw} [1/s][b]	c_s in urine[c],[19]
Sugars	Hydroxyl protons (−OH)			
Glucose	−OH	1.2, 2.2, 2.8[62]	∼2000[63,64]	37.5 (12.5-58.4)
Sorbitol	−OH	1.0[7]	n/a	9.9 (2.5-18.7)
Glycogen	−OH	1.2, 2.2, 3.0[65]	∼600[65]	n/a
Myo-inositol	−OH	∼0.8, ∼0.9, ∼1.1[66]	600[66]	22.4 (7.9-36.1)
Amino acids	Amino protons ($-NH_2$)			
Creatinine	$-NH_2$	∼1.3	n/a	14743±9797[d]
Creatine	Guanidinium protons	1.9	∼490[e],[55]	46 (3-448)
Histidine	$-NH_2$, −NH	n/a	n/a, 1700[f],[67]	43 (17-90)
Glutamine	$-NH_2$	2.9	n/a	37.3 (19.1-77.9)
Alanine	$-NH_2$	3.0[7]	∼3030[g],[68]	21.8 (7.1-43.1)
Lysine	$-NH_2$	3.0[7]	4000[f],[67]	17.2 (3.7-51.3)
Threonine	$-NH_2$, −OH	n/a, n/a	n/a, 700[f],[67]	13.3 (6.4-25.2)
Glutamate	$-NH_2$	∼3.0	∼2000[i],[65]	8.5 (3.3-18.4)
Miscellaneous				
Urea	$-NH_2$	1.0	∼1	12285 (174-49097)
Ammonia	NH_3	2.4[13]	n/a	1900.0 ± 350.0
Hippuric acid	−OH, −NH	n/a, n/a	n/a, n/a	229 (19-622)
Citric acid	−OH	0.6-0.8[69]	>2000[69]	203 (49-600)
Taurine	$-NH_2$	∼3.0[65]	300[h],[65]	81 (13-251)
Allantoin	$-NH_2$, −NH	∼1.0, ∼3.0	n/a, n/a	15.4 (4.9-29.3)
Lactate	−OH	0.4[70]	350[i],[70]	11.6 (3.5-29.3)
Choline	−OH	∼1.0[65]	∼400[65]	3.5 (1.4–6.1)

[a] δ_s in ppm is relative to the resonant frequency of water. [b]Measured at pH 7.4 and at $T = 25°C$ unless otherwise noted. [c]Concentrations of all compounds are given in [μM/mM creatinine] unless otherwise noted. [d] μM [e]Measured at pH 7.51. [f]Measured at pH 7.0 and $T = 36°C$. [g]Measured at pH 7.0 and $T = 22°C$. [h]Measured at pH 5.6. [i]Measured at pH 7.0.

Only molecules found in relatively high abundance in kidney tissue and urine were investigated. Finally, a comprehensive list of the potential CEST-active metabolites was created (Table 3). The z-spectra and magnetization transfer ratio asymmetry (MTR_{asym}) curves were measured at various pH values. While all of the systematically tested metabolites possess exchangeable protons, not all of them generate large CEST contrast at 3T in the measured pH range of 6.2-7.4 and temperature $T = 37°C$ (z-spectra and MTR_{asym} curves not shown). Creatinine, creatine, glutamine, alanine, allantoin, and glutamate showed the highest CEST effect under physiological conditions (Figure 6).

3.5 | Investigation of the specificity of urea-weighted CEST imaging

To examine the specificity of urCEST, aqueous solutions containing three most abundant urine metabolites that show measurable CEST effect, namely urea, creatinine, and creatine, were prepared at pH 5.97 and measured at $T = 37°C$ (Figure 7). The concentrations of the individual compounds were: 180, 15, and 1 mM for urea, creatinine and creatine, respectively, corresponding to the normal concentrations of these metabolites in urine (Table 3). The determined exchange rate of urea was: $k_{sw} = 9.25 \pm 1.79$, indicating good agreement with the reference k_{sw} value ($k_{sw} = 10.80 \pm 1.13$). Moreover, the calculated z-spectrum and the MTR_{asym} curve of the mixed phantom were similar to those obtained in the urine sample at pH 5.90. Both CEST spectra reveal a dominant peak at ca. 1 ppm, which can be assigned to the exchanging amide protons of urea.

4 | DISCUSSION

4.1 | Proton exchange in aqueous urea solutions

In our study, we were able to determine experimentally the urea exchange rate constants with high accuracy. The previously reported rate constants of urea are: $k_a = (7.0 \pm 2.0) \times 10^6$

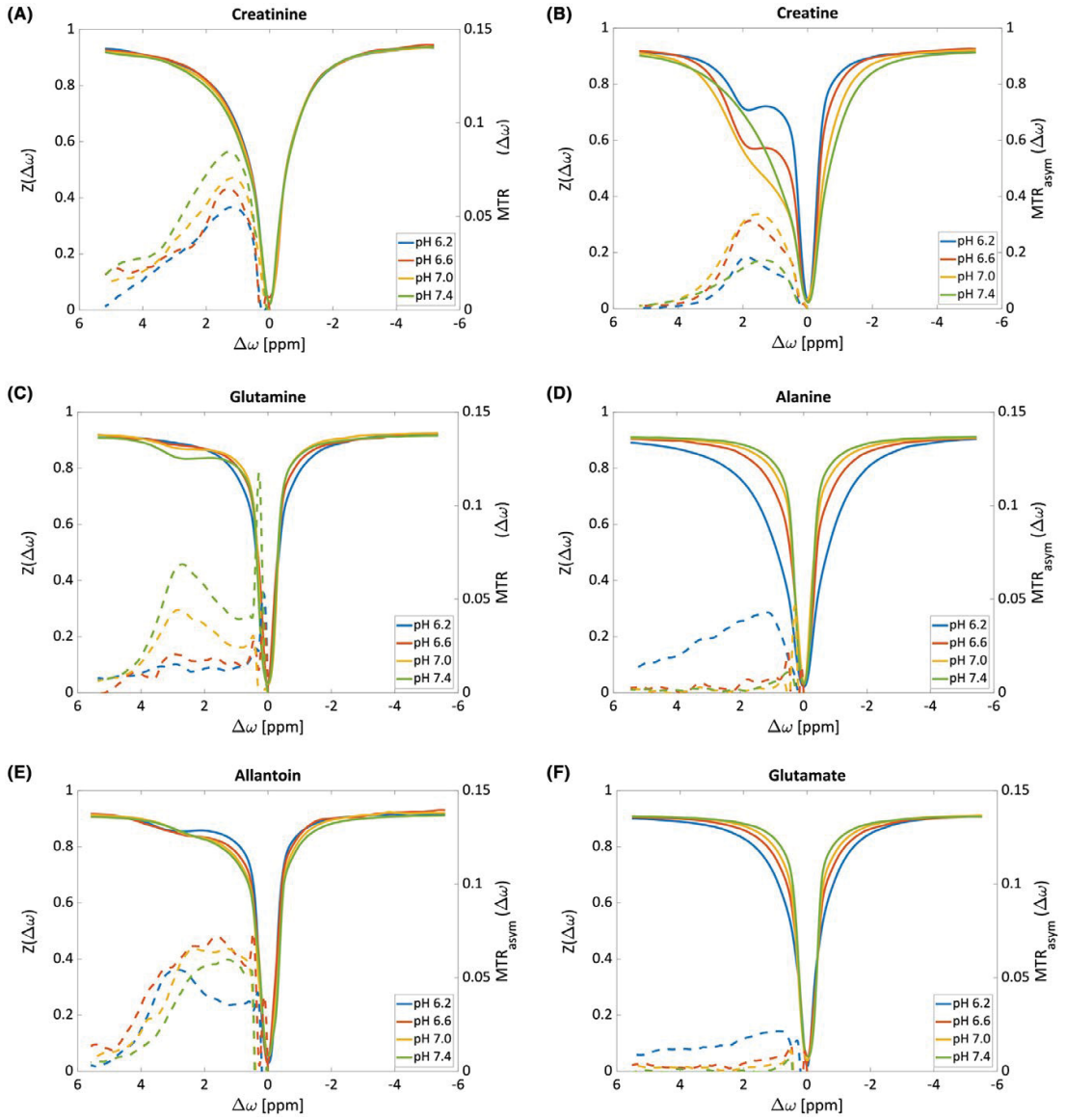

FIGURE 6 Experimentally obtained z-spectra (solid lines) and MTR_{asym} curves (dashed lines) of different kidney metabolites at $T = 37°C$. The metabolites are: (A) creatinine (100 mM), (B) creatine (100 mM), (C) glutamine (100 mM), (D) alanine (100 mM), (E) allantoin (35 mM), (F) glutamate (50 mM)

l/(mol·s), $k_b = (4.8 \pm 1.6) \times 10^6$ l/(mol·s) at $T = 22°C$ (29), and $k_a = (9.0 \pm 1.0) \times 10^6$ l/(mol·s), $k_b = (2.4 \pm 1.0) \times 10^6$ l/(mol·s) at $T = 35°C$ [24,44] and have been measured by use of line shapes of urea and water in ^{1}H NMR. For amides, this method is not exact because of line broadening associated with ^{14}N quadrupole relaxation of the amide nitrogen.[45] As an alternative, line shapes for the proton-coupled ^{15}N NMR spectra were calculated for investigating the NH-exchange rates of urea, yielding the following results: $k_a = (18.0 \pm 12.0) \times 10^6$ l/(mol·s), $k_b = (4.4 \pm 1.0) \times 10^6$ l/(mol·s) at $T = 32°C$.45 It seems that the WEX II method provides smaller standard errors than the linewidth-based methods and thus improves the accuracy and precision of predictions. Although all previous estimated k_a and k_b values are in good agreement, direct comparison of the results is difficult due to differences in the experimental conditions, such as the buffer concentration

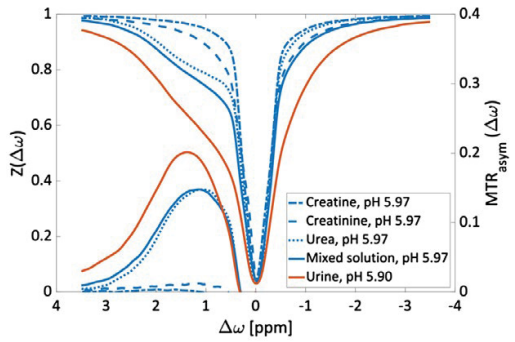

FIGURE 7 Z-spectra and MTR_{asym} curves for the individual solutions of 180 mM urea (blue dotted line), 15 mM creatinine (blue dashed line), 1 mM creatine (blue dash-dot line), their mixture (blue solid line) at pH 5.97 and for the urine sample (red solid line) at pH 5.90. The temperature of the model solutions during the measurements was kept constant at $T = (37 \pm 1)$°C

and temperature. Since the pH in urea solutions tends to drift slowly because of CO_2 absorption and decomposition of urea into ammonium and cyanate ions,[24,46] we dissolved urea in 50 mM Na/K-phosphate buffer. The pH value did not change over a period of several hours.

The acid-catalyzed rate constant of urea is large compared to rate constants for acid-catalyzed protolysis of most amides.[23,44] High k_a rate constant suggests higher probability of H_3O^+ with nitrogen than with oxygen, resulting in observable proton transfer.[44] Thus, the large value of k_a for urea solution implies protonation on urea nitrogen rather than oxygen.[44]

The comparison of the estimated activation energies $E_{A,a} \approx (19 \pm 4)$ kcal/mol and $E_{A,b} \approx (10 \pm 2)$ kcal/mol with the apparent heat of activation for amide hydrogen exchange of about 17 kcal/mol, reported by Englander et al shows good agreement.[47] Recently, Bodet et al. estimated the effective activation energy of amide proton exchange $E_{b,eff} = (54.12 \pm 9.15)$ kJ/mol $\approx (13 \pm 2)$ kcal/mol in carnosine solutions buffered with (1/15) M PBS buffer.[27] The same study also showed that the buffer has a strong influence on the amide hydrogen exchange rate and its dependence on pH and temperature. This finding should be taken into consideration when analyzing our results.

4.2 | WEX and CEST methods

Several methods have been proposed for estimation exchange rates, which is possible due to their dependence on the saturation power and time.[29,31-33,48-50] The water exchange (WEX) filter sequence has already been used for measuring exchange rates of slowly exchanging species.[17,27,37] Therefore, we decided to apply this method to amide exchange in aqueous urea solutions. In contrast to the original WEX II sequence, we used excitation sculpting instead of WATERGATE technique for water suppression. Because of the large width of the urea peak and its nearness to the water resonant frequency, we expect that the WATERGATE water suppression may negatively impact the urea signal due to the lack of sufficient selectivity.[51] One of the challenges with the spectroscopy (MRS)-based methods, such as the WEX approach, is the low sensitivity, which makes it difficult to detect low abundance metabolites in vivo. Furthermore, the WEX experiments are not suitable for measuring faster rates since the signal of the exchangeable peak is reduced owing to exchange with suppressed water proton.[28,52] The WEX spectroscopy has been already used to measure exchange rates of creatine guanidinium protons and amide protons of carnosine on a 3T clinical MRI system.[26,27] However, this method is not applicable to urea samples at low magnetic field.

The exchange rates of urea derived from CEST experiments are in good agreement with those obtained by WEX experiments. However, it was not possible to determine the k_{sw} values of urea in the physiologically relevant pH range. Derivation of the exchange-dependent relaxation rate R_{ex} used here is based on the assumption that the influence of the R_{1s} is negligible against k_{sw} for exchanging system.[53,54] This requirement is not fulfilled for exchange rates that are in the order of the longitudinal relaxation rate R_{1s}. Moreover, in the neutral solutions the CEST effect was minimal and thus the signal to noise ratio was insufficient for a proper quantification.

In order to determine the quantitative CEST parameters of urea, we have applied the extended steady-state method AREX, introduced by Roelloffs et al.[34,35] For extremely slow exchange rates of urea, modeling of bi-exponential decay during the break was important. The exchange rates obtained using the "standard" AREX approach, were significantly overestimated (approximately 40%). Since the CEST contrast depends on both concentration and k_{sw}, it is necessary to employ quantitative methods that allow separating these parameters. Previous study have shown that the CEST effect can be represented as a linear function of $1/B_1^2$ and that the exchange rate and proton fraction can be determined independently by linear regression (the so-called ω-plot).[31-33,48,49] However, this method seems to be not applicable at low exchange rates due to a high noise level and small B_1 dispersion.[26,55]

In our study, we have investigated a number of important kidney/urine metabolites with exchangeable protons that may produce a CEST effect in vivo. However, for most of them no CEST contrast in the examined pH range and at a buffer concentration of 50 mM was observed at 37°C. This is consistent with the fast exchange. Moreover, in the case of hydroxyl groups of, eg, myo-inositol, glucose, and glycogen the resonance peaks were possibly within the linewidth of the water resonance. Therefore, it is unlikely that any of these metabolites contribute to the total CEST effect at ca. 1 ppm in kidney

at clinical field. Besides urea, several other compounds show a measurable CEST effect under physiological conditions at 3T. These might potentially overlap with the urea CEST signal in the urine/kidney in vivo. The absolute urea quantification might be, therefore, considerably hampered. In our study, we were able to estimate the k_{sw} of urea from CEST experiments performed on a mixture model solution of urea, creatinine, and creatine. However, we have assumed that the urea concentration is much higher than the creatinine concentration (12:1), as had been previously measured in urine (Table 3).[19] The difference in MTR_{asym} between the urine and mixture peaks results most likely from slightly different pH values as well as different concentrations of individual metabolites in urine compared with the mixed solution. To the best of our knowledge, no study determined absolute concentrations of metabolites in human kidney in vivo. Further extensive research is necessary in order to assess the contribution of other kidney metabolites superimposed on the urCEST effect at different pH.

pH-sensitive chemical exchange saturation transfer (CEST) MRI is a promising new method for in vivo applications.[56-60] Exogenous CEST agent pH mapping have already been applied for kidney imaging. The measured pH in kidneys was shown to vary between 5.4 and 7.4 for healthy mice.[58] Since the exchange rate of urea is minimal at this pH range, it might be challenging to obtain the pH maps of kidneys using only the quantitative urea-weighted CEST method. On the other hand, pH could be measured independently using paraCEST (eg, Lanthanide-DOTA-tetraamide complexes,[56] Eu3+ based agents[56,57]) or diaCEST agents (eg, Iopamidol[58,59]) in order to derive urea concentration by combining Equations 1 and 10.[60]

5 | CONCLUSIONS

In our study, we present a successful application of the WEX spectroscopy for determining exchange rate constants of urea and evaluate the feasibility of the quantitative urea-weighted CEST imaging at a clinical MRI system. We show that similar to simple amides, proton exchange in aqueous urea solutions is acid and base catalyzed with the rate constants: $k_a = (9.95 \pm 1.1) \times 10^6$ l/(mol·s) and $k_b = (6.21 \pm 0.21) \times 10^6$ l/(mol·s), and activation energies: $E_{A,a} = 79.13 \pm 15.87$ kJ/mol and $E_{A,b} = 43.52 \pm 9.56$ kJ/mol, respectively. Although urea protons undergo a slow exchange with water protons, it was possible to estimate its exchange rate at pH values below 6.2 and above 7.4 at $T = (37 \pm 1)$°C using the quantitative CEST analysis. Moreover, several other kidney metabolites, which are expected to partially conceal the CEST effect of urea in vivo, were examined. Further investigations are needed to characterize the explicit dependence of the exchange rate constant of urea amide protons on different pH buffer systems.

ACKNOWLEDGMENTS

This study was supported by a Grant from the Forschungskommission of the Faculty of Medicine, Heinrich Heine University, Düsseldorf (Grant No: 13/2015). The authors acknowledge access to the Jülich-Düsseldorf Biomolecular NMR Center.

REFERENCES

1. Bennion BJ, Daggett V. The molecular basis for the chemical denaturation of proteins by urea. *Proc Nat Acad Sci USA* 2003;100:5142–5147.
2. Atkinson DE, Bourke E. The role of ureagenesis in pH homeostasis. *Trends Biochem Sci*. 1984;9:297–300.
3. Weiner ID, Mitch WE, Sands JM. Urea and ammonia metabolism and the control of renal nitrogen excretion. *Clin J Am Soc Nephrol*. 2015;10:1444–1458.
4. Champe PC, Harvey RA, Ferrier DR. *Lippincott's Illustrated Reviews: Biochemistry*. 5th ed. Philadelphia: Lippincott Williams & Wilkins; 2004.
5. Baum N, Dichoso CC, Carlton CE. Blood urea nitrogen and serum creatinine: physiology and interpretations. *Urology* 1975;5:583–588.
6. Herget-Rosenthal S. Imaging techniques in the management of chronic kidney disease: current developments and future perspectives. *Seminars Nephrol*. 2011;31:283–290.
7. Ward KM, Aletras AH, Balaban RS. A new class of contrast agents for MRI based on proton chemical exchange dependent saturation transfer (CEST). *J Magn Reson*. 2000;143:79–87.
8. van Zijl PCM, Yadav NN. Chemical exchange saturation transfer (CEST): what is in a name and what isn't? *Magn Reson Med*. 2011;65:927–948.
9. Heo H-Y, Zhang Y, Burton TM, et al. Improving the detection sensitivity of pH-weighted amide proton transfer MRI in acute stroke patients using extrapolated semisolid magnetization transfer reference signals. *Magn Reson Med*. 2017;78:871–880.
10. Zhang S, Malloy CR, Sherry AD. MRI thermometry based on PARACEST agents. *J Am Chem Soc*. 2005;127:17572–17573.
11. Yang B, Bankir L. Urea and urine concentrating ability: new insights from studies in mice. *Am J Phys-Renal Phys*. 2005;288: F881–F896.
12. Hastings J, de Matos P, Dekker A, et al. The ChEBI reference database and ontology for biologically relevant chemistry: enhancements for 2013. *Nucleic Acids Res*. 2013;41:D456–D463.
13. Guivel-Scharen V, Sinnwell T, Wolff SD, Balaban RS. Detection of proton chemical exchange between metabolites and water in biological tissues. *J Magn Reson*. 1998;133:36–45.
14. Dagher AP, Aletras A, Choyke P, Balaban RS. Imaging of urea using chemical exchange-dependent saturation transfer at 1.5T. *J Magn Reson Imaging* 2000;12:745–748.
15. Vinogradov E, Liu Z, Madhuranthakarn A, et al. Endogenous urea CEST (urCEST) for MRI monitoring of kidney function. In *Proceedings of the 23th Annual Meeting and Exhibition of ISMRM*, Toronto, Canada, 2015:3375.
16. Kim J, Wu Y, Guo Y, Zheng H, Sun PZ. A review of optimization and quantification techniques for chemical exchange saturation transfer MRI toward sensitive in vivo imaging. *Contrast Media Mol Imaging* 2015;10:163–178.

17. Mori S, Abeygunawardana C, van Zijl PCM, Berg JM. Water exchange filter with improved sensitivity (WEX II) to study solvent-exchangeable protons. Application to the consensus zinc finger Peptide CP-1. *J Magn Res Ser B*. 1996;110:96–101.
18. Serkova N, Fuller TF, Klawitter J, Freise CE, Niemann CU. ^{1}H-NMR-based metabolic signatures of mild and severe ischemia/reperfusion injury in rat kidney transplants. *Kidney Int*. 2005;67:1142–1151.
19. Bouatra S, Aziat F, Mandal R, et al. The human urine metabolome. *PLoS One* 2013;8:e73076.
20. Findeisen M, Brand T, Berger S. A ^{1}H-NMR thermometer suitable for cryoprobes. *Magn Reson Chem*. 2006;45:175–178.
21. Delaglio F, Grzesiek S, Vuister GW, Zhu G, Pfeifer J, Bax AD. NMRPipe: a multidimensional spectral processing system based on UNIX pipes. *J Biomol NMR* 1995;6:277–293.
22. Kim M, Gillen J, Landman BA, Zhou J, van Zijl PCM. Water saturation shift referencing (WASSR) for chemical exchange saturation transfer (CEST) experiments. *Magn Reson Med*. 2009;61:1441–1450.
23. Berger A, Loewenstein A, Meiboom S. Nuclear magnetic resonance study of the protolysis and ionization of N-Methylacetamide1. *J Am Chem Soc*. 1959;81:62–67.
24. Klotz IM, Hunston DL. Proton exchange in aqueous urea solutions. *J Phys Chem*. 1971;75:2123–2127.
25. Foote HW. Elements of physical chemistry. *Science* 1907;26:588–588.
26. Goerke S, Zaiss M, Bachert P. Characterization of creatine guanidinium proton exchange by water-exchange (WEX) spectroscopy for absolute-pH CEST imaging in vitro. *NMR Biomed*. 2014;27:507–518.
27. Bodet O, Goerke S, Behl NGR, Roeloffs V, Zaiss M, Bachert P. Amide proton transfer of carnosine in aqueous solution studied in vitro by WEX and CEST experiments. *NMR Biomed*. 2015;28:1097–1103.
28. McMahon MT, Gilad AA, Zhou J, Sun PZ, Bulte JWM, van Zijl PCM. Quantifying exchange rates in chemical exchange saturation transfer agents using the saturation time and saturation power dependencies of the magnetization transfer effect on the magnetic resonance imaging signal (QUEST and QUESP): Ph calibration for poly-L-lysine and a starburst dendrimer. *Magn Reson Med*. 2006;55:836–847.
29. Dixon WT, Ren J, Lubag AJM, et al. A concentration-independent method to measure exchange rates in PARACEST agents. *Magn Reson Med*. 2010;63:625–632.
30. Sun PZ. Simplified quantification of labile proton concentration-weighted chemical exchange rate (kws) with RF saturation time dependent ratiometric analysis (QUESTRA): normalization of relaxation and RF irradiation spillover effects for improved quantitative chemical exchange saturation transfer (CEST) MRI. *Magn Reson Med*. 2011;67:936–942.
31. Sun PZ. Simultaneous determination of labile proton concentration and exchange rate utilizing optimal RF power: Radio frequency power (RFP) dependence of chemical exchange saturation transfer (CEST) MRI. *J Magn Reson*. 2010;202:155–161.
32. Wu R, Xiao G, Zhou IY, Ran C, Sun PZ. Quantitative chemical exchange saturation transfer (qCEST) MRI—omega plot analysis of RF-spillover-corrected inverse CEST ratio asymmetry for simultaneous determination of labile proton ratio and exchange rate. *NMR Biomed*. 2015;28:376–383.
33. Meissner J-E, Goerke S, Rerich E, et al. Quantitative pulsed CEST-MRI using Ω-plots. *NMR Biomed*. 2015;28:1196–1208.
34. Zaiss M, Xu J, Goerke S, et al. Inverse Z-spectrum analysis for spillover-, MT-, and T_1-corrected steady-state pulsed CEST-MRI—application to pH-weighted MRI of acute stroke. *NMR Biomed*. 2014;27:240–252.
35. Roeloffs V, Meyer C, Bachert P, Zaiss M. Towards quantification of pulsed spinlock and CEST at clinical MR scanners: an analytical interleaved saturation—relaxation (ISAR) approach. *NMR Biomed*. 2014;28:40–53.
36. Santyr GE, Fairbanks EJ, Kelcz F, Sorenson JA. Off-resonance spin locking for MR imaging. *Magn Reson Med*. 1994; 32:43–51.
37. Hwang TL, Shaka AJ. Water suppression that works. Excitation sculpting using arbitrary wave-forms and pulsed-field gradients. *J Magn Reson Ser A*. 1995;112:275–279.
38. Grzesiek S, Bax A. The importance of not saturating water in protein NMR. Application to sensitivity enhancement and NOE measurements. *J Am Chem Soc*. 1993;115:12593–12594.
39. Geen H, Freeman R. Band-selective radiofrequency pulses. *J Magn Reson (1969)* 1991;93:93–141.
40. Cavanagh J, Fairbrother WJ, Palmer AG, IIIRance M, Skelton NJ. *Protein NMR Spectroscopy*. 2nd ed. Burlington: Elsevier Academic Press; 1996.
41. Zhang O, Kay LE, Olivier JP, Forman-Kay JD. Backbone ^{1}H and ^{15}N resonance assignments of the N-terminal SH3 domain of drk in folded and unfolded states using enhanced-sensitivity pulsed field gradient NMR techniques. *J Biomol NMR* 1994;4:845–858.
42. Seber GAF, Wild CJ. *Nonlinear Regression*; New York: John Wiley and Sons; 1989.
43. Bassi R, Niewczas MA, Biancone L, et al. Metabolomic profiling in individuals with a failing kidney allograft. *PloS One* 2017;12:e0169077-e0169077.
44. Vold RL, Daniel ES, Chan SO. Magnetic resonance measurements of proton exchange in aqueous urea. *J Am Chem Soc*. 1970;92:6771–6776.
45. Yavari I, Roberts JD. Nitrogen-15 nuclear magnetic resonance spectroscopy. NH proton exchange reactions of urea and substituted ureas. *Organ Magn Reson*. 1980;13:68–71.
46. Dortch RD, Horch RA, Does MD. Development, simulation, and validation of NMR relaxation-based exchange measurements. *J Chem Phys*. 2009;131:164502.
47. Englander SW, Downer NW, Teitelbaum H. Hydrogen exchange. *Annual Rev Biochem*. 1972;41:903–924.
48. Wu R, Liu C-M, Liu PK, Sun PZ. Improved measurement of labile proton concentration-weighted chemical exchange rate (kws) with experimental factor-compensated and T_1-normalized quantitative chemical exchange saturation transfer (CEST) MRI. *Contrast Media Mol Imaging* 2012;7:384–389.
49. Sun PZ, Wang Y, Dai Z, Xiao G, Wu R. Quantitative chemical exchange saturation transfer (qCEST) MRI—RF spillover effect-corrected omega plot for simultaneous determination of labile proton fraction ratio and exchange rate. *Contrast Media Mol Imaging* 2014;9:268–275.
50. Bottomley PA, Griffiths JR. *Handbook of Magnetic Resonance Spectroscopy in vivo: MRS Theory, Practice and Applications*. Chichester, UK: Wiley; 2016.
51. Liu L, Mo H, Wei S, Raftery D. Quantitative analysis of urea in human urine and serum by ^{1}H nuclear magnetic resonance. *Analyst* 2012;137:595–600.

52. Valérie CP, Allen MJ. *Contrast Agents for MRI: Experimental Methods (New Developments in NMR)*. 1st ed. Cambridge: Royal Society of Chemistry; 2017.
53. Zaiss M, Bachert P. Exchange-dependent relaxation in the rotating frame for slow and intermediate exchange—modeling off-resonant spin-lock and chemical exchange saturation transfer. *NMR Biomed*. 2012;26:507–518.
54. Zaiss M, Bachert P. Chemical exchange saturation transfer (CEST) and MR *Z*-spectroscopy in vivo: a review of theoretical approaches and methods. *Phys Med Biol*. 2013;58:R221–R269.
55. Stabinska J, Cronenberg T, Wittsack H-J, Lanzman RS, Müller-Lutz A. Quantitative pulsed CEST-MRI at a clinical 3T MRI system. *Magn Reson Mater Phys Biol Med*. 2017;30:505–516.
56. Pavuluri K, McMahon MT. pH Imaging using chemical exchange saturation transfer (CEST) MRI. *Israel J Chem*. 2017;57:862–879.
57. Wu Y, Zhang S, Soesbe TC, et al. pH imaging of mouse kidneys in vivo using a frequency-dependent paraCEST agent. *Magn Reson Med*. 2015;75:2432–2441.
58. Longo DL, Dastrù W, Digilio G, et al. Iopamidol as a responsive MRI-chemical exchange saturation transfer contrast agent for pH mapping of kidneys: in vivo studies in mice at 7 T. *Magn Reson Med*. 2010;65:202–211.
59. Longo DL, Sun PZ, et al. A general MRI-CEST ratiometric approach for pH imaging: demonstration of in vivo pH mapping with iobitridol. *J Am Chem Soc*. 2014;136:14333–14336.
60. Sun PZ, Longo DL, Hu W, Xiao G, Wu R. Quantification of iopamidol multi-site chemical exchange properties for ratiometric chemical exchange saturation transfer (CEST) imaging of pH. *Phys Med Biol*. 2014;59:4493–4504.
61. Finer EG, Franks F, Tait MJ. Nuclear magnetic resonance studies of aqueous urea solutions. *J Am Chem Soc*. 1972;94:4424–4429.
62. Chan KWY, McMahon MT, Kato Y, et al. Natural D-glucose as a biodegradable MRI contrast agent for detecting cancer. *Magn Reson Med*. 2012;68:1764–1773.
63. Hills BP. Multinuclear NMR studies of water in solutions of simple carbohydrates. *Mol Phys*. 1991;72:1099–1121.
64. Wiebenga-Sanford BP, DiVerdi J, Rithner CD, Levinger NE. Nanoconfinement's dramatic impact on proton exchange between glucose and water. *J Phys Chem Lett*. 2016;7:4597–4601.
65. Lee J-S, Xia D, Jerschow A, Regatte RR. In vitro study of endogenous CEST agents at 3T and 7T. *Contrast Media Mol Imaging* 2015;11:4–14.
66. Haris M, Cai K, Singh A, Hariharan H, Reddy R. In vivo mapping of brain myo-inositol. *NeuroImage* 2011;54:2079–2085.
67. Liepinsh E, Otting G. Proton exchange rates from amino acid side chains—implications for image contrast. *Magn Reson Med*. 1996;35:30–42.
68. Wermter FC, Bock C, Dreher W. Investigating GluCEST and its specificity for pH mapping at low temperatures. *NMR Biomed*. 2015;28:1507–1517.
69. Basharat M, deSouza NM, Parkes HG, Payne GS. Determining the chemical exchange saturation transfer (CEST) behavior of citrate and spermine under in vivo conditions. *Magn Reson Med*. 2016;76:742–746.
70. DeBrosse C, Nanga RPR, Bagga P, et al. Lactate chemical exchange saturation transfer (LATEST) imaging in vivo a biomarker for LDH activity. *Sci Rep*. 2016;6:19517.

How to cite this article: Stabinska J, Neudecker P, Ljimani A, Wittsack H-J, Lanzman H-RS, Müller-Lutz A. Proton exchange in aqueous urea solutions measured by water-exchange (WEX) NMR spectroscopy and chemical exchange saturation transfer (CEST) imaging in vitro. *Magn Reson Med*. 2019;00:1–13. https://doi.org/10.1002/mrm.27778

Appendix C

Publication 3

The results of **study 3** have been submitted for publication in:

Stabinska J, Müller-Lutz A, Wittsack HJ, Tell C, Rump LC, Ertas N, Antoch G, Ljimani A. Dixon-based CEST MRI in renal transplant recipients: a preliminary study. (*Submitted to Magn Reson Imaging*)

Personal contribution: 80% (MRI sequence developement, data acquisition, data analysis, data interpretation, manuscript writing, manuscript revision)

Dixon-based chemical exchange saturation transfer (CEST) MRI in renal transplant recipients: a preliminary study

Julia Stabinska[1], Anja Müller-Lutz[1*], Hans-Jörg Wittsack[1], Christian Tell[2], Lars Christian Rump[2], Neslihan Ertas[3], Gerald Antoch[1], Alexandra Ljimani[1]

[1]Department of Diagnostic and Interventional Radiology, Medical Faculty, Heinrich Heine University Düsseldorf, Moorenstr. 5, 40225 Düsseldorf, Germany

[2]Department of Nephrology, Medical Faculty, Medical Faculty, Heinrich Heine University Düsseldorf, Moorenstr. 5, 40225 Düsseldorf, Germany

[3]Department of Vascular and Endovascular Surgery, Medical Faculty, Heinrich Heine University Düsseldorf, Moorenstr. 5, 40225 Düsseldorf, Germany

E-mail addresses:

Julia Stabinska, Julia.Stabinska@med.uni-duesseldorf.de; Anja Müller-Lutz*, Anja.Lutz@med.uni-duesseldorf.de; Hans-Jörg Wittsack, Hans-Joerg.Wittsack@med.uni-duesseldorf.de; Christian Tell, Christian.Tell@med.uni-duesseldorf.de; Lars C. Rump, Christian.Rump@med.uni-duesseldorf.de; Neslihan Ertas, Neslihan.Ertas@med.uni-duesseldorf.de; Gerald Antoch, Antoch@med.uni-duesseldorf.de; Alexandra Ljimani, Alexandra.Ljimani@med.uni-duesseldorf.de;

*** Corresponding author**

Highlights:

- Amide Proton Transfer (APT) imaging of the kidney is affected by fat-induced artifacts
- Dixon-based CEST analysis increases the specificity of APT contrast in the human kidney
- Highest CEST effect in the renal tissue is observed at frequency offset of about 1 ppm

Abstract

Purpose: To assess the feasibility of performing Dixon-based chemical exchange saturation transfer (CEST) imaging for improved fat suppression in renal transplant.

Methods: The Dixon-based CEST MRI has been validated in phantom and in vivo. Fourteen renal transplant recipients were examined at 3T using a multi-echo CEST sequence. The two-point Dixon technique was applied to generate water-only CEST images at different frequency offsets, which were further used to calculate the z-spectra. The asymmetry of the magnetization transfer ratio (MTR_{asym}) values in the frequency ranges of hydroxyl, amine and amide protons were estimated in the renal cortex and medulla.

Results: The Dixon technique enables effective fat peak removal and does not introduce additional asymmetries to the z-spectrum. Our results show that the fat-corrected amide proton transfer (APT) effect in the kidney (-0.06 ± 0.62% for cortex, 0.32 ± 0.62% for medulla) is significantly higher compared to that obtained from the in-phase (IP) CEST data (-1.0 ± 1.0% for cortex, -0.12 ± 0.78% for medulla) at a significance level of 0.05, indicating that the two-point Dixon-based CEST method increases the specificity of the APT contrast by correcting the fat-induced artifacts.

Conclusion: Combination of the dual-echo CEST acquisition with Dixon post-processing provides effective water-fat separation, allowing more accurate quantification of the amide proton transfer (APT) CEST effect in the transplanted kidney.

Keywords: CEST, APT, renal CEST, kidney transplant, Dixon

Introduction

Kidney transplantation is the treatment of choice for many patients with end stage renal disease (ESRD) (1). Early detection and adequate management of renal allograft dysfunction is hereby crucial for graft survival (2). The most commonly used biochemical marker of allograft dysfunction is a rise in serum creatinine level (SCr), which, however, is only observed if considerable damage has occurred in the allograft (3; 4; 5). For diagnosis of acute graft rejection, a percutaneous ultrasound-guided kidney biopsy is considered the gold standard (6). Nevertheless, because of the relatively low sensitivity of creatinine determinations and the invasiveness of renal biopsies, imaging modalities are increasingly used for monitoring renal transplant status (7). A number of studies have demonstrated the efficacy of several functional renal MRI techniques for the evaluation of early and long term post-transplantation complications (8; 9; 10; 11).

Chemical exchange saturation transfer (CEST) is a novel MRI contrast mechanism that enables indirect detection of small metabolites, e.g. creatine (12; 13), urea (14; 15), glucose (16; 17) and proteins (18; 19) as well as in vivo pH mapping (20). The results of recent studies suggest that CEST MRI can provide new insights and a better understanding of renal system diseases on a molecular level and therefore usefully complement the existing techniques (21; 22; 23; 24; 25; 26, 27).

Despite its promising potential to provide additional molecular information, CEST MRI in the human kidney remains technically challenging due to the presence of fat in and around the kidney, large B_0 field inhomogeneity and physiological motion (28). Specifically, it has previously been shown that the strong lipid signals at -3.5 ppm upfield from the water resonance can lead to an erroneous amide proton transfer (APT) contrast at 3.5 ppm (29; 30; 31). The use of this important variant of CEST MRI has lately been investigated for detecting sepsis-induced acute kidney injury (SAKI), and has been proven to be more sensitive to the pathological changes in the injured kidneys than the changes in T1, T2 and MTC effect (26).

Furthermore, a broad lipid peak might impact the quantification of the CEST effects from the labile protons of kidney metabolites with resonance frequencies around 3 ppm, such as glutamate and alanine (32). Therefore, to allow more reliable quantification of the magnetization transfer effects in the human kidney, the fat-signal induced artifacts need to be corrected.

In this preliminary study, we investigated the feasibility of performing Dixon-based CEST imaging of the human kidney transplant on a clinical 3T MRI system. The primary focus was to validate the utility of the two-point Dixon (2pt-Dixon) water-fat separation (33) to obtain water-only CEST images in vivo in renal transplants. For this purpose, we (i) optimized the CEST acquisition protocol and post-processing pipeline for renal graft imaging on a clinical 3T MRI system, and (ii) quantified the cortical and medullary CEST effects in three frequency ranges centered at 1 ppm, 2 ppm and 3.5 ppm from the z-spectra calculated with and without Dixon.

Methods

Phantom

Fresh hen egg was used to verify effectiveness of the Dixon method for the removal of lipid contribution from the CEST data. In fact, fresh and cooked eggs have been used as a phantom in previous MRI studies (34; 35). Egg yolk contains about 16 % proteins and 37% lipids, whereas the egg white mainly consist of water and about 11% proteins (36).

Subjects

The study was approved by the local ethics committee, and the written informed consent was obtained from all participants. Fourteen renal transplant recipients (5 females and 9 males; age range: 23 - 78 years; mean age: 51 ± 16.8) were examined. All images were collected without any restriction on fluid or food intake prior to MRI examination (37).

89 **MRI Experiments**

90 All the experiments were performed on a 3T MAGNETOM Prisma MRI system (Siemens Healthineers,
91 Erlangen, Germany) using an in-house developed multi-echo MT-prepared gradient-echo CEST MRI
92 sequence. The phantom data were acquired with a 16-channel head coil, whereas the in vivo human data
93 were collected using a 18-channel torso array coil and a 32-channel spine coil. A half-Fourier single-shot
94 turbo spin echo (HASTE) with a resolution of $0.8 \times 0.8 \times 4$ mm^3 was used for in vivo anatomical images. The
95 pulsed saturation module of the CEST sequence consisted of 15 Gaussian-shaped RF pulses with a single
96 pulse duration t_{pd} = 100 msec, an interpulse duration t_{ipd} = 100 msec and B_1 = 1.2 µT, followed by a dual-
97 echo gradient echo imaging. Images were acquired at 41 frequency offsets from -6 ppm to 6 ppm. The
98 imaging parameters were: transversal FOV = 380×380 mm^2 and voxel size = $1 \times 1 \times 5$ mm^3 for human data,
99 and coronal FOV = 240×240 mm^2 and voxel size = $0.9 \times 0.9 \times 5$ mm^3 for phantom data, TR/TE_1/TE_2 =
100 (4.2/1.5/2.5) msec, number of averages = 2. To determine B_0 maps using the water saturation shift
101 referencing method (WASSR) (37), a single Gaussian-shaped pulse with RF saturation power of B_1 = 0.2 µT
102 and pulse duration t_{pd} = 25 msec was applied. The WASSR z-spectra were obtained at 34 frequency offsets
103 between ±1 ppm. No motion correction method has been applied in our experiments since the respiratory
104 motion artifacts are usually negligible in renal allograft recipients owing to the placement of the kidney
105 graft in the iliac fossa (39).

106 **Data Analysis**

107 All CEST images were processed voxel-wise and ROI-based in MATLAB (Mathworks, Natick, MA, USA). For
108 each offset, four types of images were obtained using the 2-pt Dixon method: 1) the water-only image, 2)
109 fat-only image, 3) in-phase image (IP), and 4) out-of-phase image (OP). The B_0 maps were generated
110 separately from the WASSR images.

The feasibility of the Dixon method for water-fat separation was assessed in vitro by comparing the z-spectra obtained from phantom data acquired with and without Dixon. As a standard the second echo source image at TE = 2.5 msec (close to IP) was chosen, whereas the CEST-Dixon images were the water-only images.

For the in vivo analysis, the cortical-medullary regions of interest (ROIs) were manually segmented on the anatomical images by an experienced radiologist (AL, 11 years of experience) using the image segmentation toolbox ITK-SNAP (40).

Z-spectra were obtained by plotting the normalized signal intensity as a function of frequency offset $\Delta\omega$. Further, the asymmetry of the magnetization transfer ratio (MTR_{asym}) was calculated as follows:

$$MTR_{asym} = \frac{M_{sat}(-\Delta\omega) - M_{sat}(\Delta\omega)}{M_0}$$

where M_{sat} refers to the magnetization with saturation at a positive frequency position $\Delta\omega$, or a mirrored frequency offset on the opposite side of the water resonance ($-\Delta\omega$). M_0 denotes a reference signal intensity measured at 300 ppm. The ROI-averaged values and pixel-wise maps of MTR_{asym} were calculated in three frequency ranges (i) 0.8-1.2 ppm (ii) 1.8-2.2 ppm, and (iii) 3.3-3.7 ppm, corresponding to respectively hydroxyl, amine, and amide frequency offsets.

Statistical Analysis

The Shapiro-Wilk test was used to determine if the null hypothesis of composite normality is true at a significance level P = 0.05. The homogeneity of variances were tested using Flinger-Killeen test. A post hoc test showed no significant differences in the variance at P = 0.05. After ANOVA test, multiple paired t-test with Bonferroni correction has been applied to compare the cortical and medullary MTR_{asym} values measured using the conventional and Dixon-based CEST method. The statistical data analysis and visualization was performed using SpecVis (https://github.com/hezoe100/SpecVis) (41).

Results

Phantom Experiment

Figure 1 shows the z-spectra of the egg phantom calculated from the images acquired with and without Dixon. A large fat dip at about -3.5 ppm (black arrow), which is mostly due to lipid direct saturation signal, can be observed in the non-Dixon IP z-spectrum of the egg yolk. In the water-only z-spectrum, the lipid signal was effectively removed. Furthermore, higher suppression level around the water resonance was obtained after applying Dixon method. This is consistent with previous results (31). The z-spectra measured in the egg white with and without Dixon were similar, indicating that the CEST effect at 3.5 ppm (red arrow) is not affected by the Dixon water-fat decomposition.

In Vivo Study

Although all subjects were successfully scanned, two datasets had to be excluded from further analysis due to macroscopic motion.

Figure 2 displays water-only and fat only map obtained using the 2pt-Dixon method in an exemplary patient. The overall quality of the water-fat separation was good with only a few water-fat swaps that did not affect the CEST quantification in the transplanted kidney.

Figure 3 compares the z-spectra (Figure 3a and 3b) and the MTR_{asym} curves (Figure 3c and 3d) measured in the renal medulla and cortex/capsule of a representative patient. In the lipid-abundant renal capsule, the signal at about -3.5 ppm was effectively suppressed in the Dixon-based z-spectrum, producing higher MTR_{asym} values at 3.5 ppm compared to the IP z-spectrum (Figure 3d). At the same time, in the renal medulla that is essentially free of fat influence, negligible difference between the z-spectra obtained from the water-only and conventional CEST images can be observed (Figure 3c).

Table 1 summarizes the averaged MTR_{asym} values calculated in the three frequency ranges (0.8 1.2 ppm, 1.8 - 2.2 ppm, and 3.3 - 3.7 ppm) from the Dixon and conventional CEST data. Overall, the mean MTR_{asym} values decreased with increasing frequency offset in the renal cortex and medulla. No significant differences between the cortical and medullary CEST values were observed. The amide MTR_{asym} values obtained from the water-only images (-0.06 ± 0.62% for cortex, 0.32 ± 0.62% for medulla) were significantly higher than those obtained from the IP CEST data (-1.0 ± 1.0% for cortex, -0.12 ± 0.78% for medulla) ($P < 0.05$ for cortex and medulla). At the same time, there were no significant differences in the hydroxyl and amine MTR_{asym} values between the IP-, OP-, and Dixon-based CEST quantification ($P > 0.05$ for all comparisons). The OP CEST data led to significantly higher cortical and medullary MTR_{asym} values at 3.5 ppm (0.8 ± 1.4% for cortex, 0.8 ± 0.9% for medulla) compared to the IP non-Dixon data ($P < 0.05$ for cortex and medulla), most probably due to signal interferences and normalization as discussed elsewhere (30).

Figure 4 shows boxplots of ROI-based MTR_{asym} values in the three frequency ranges obtained in the renal medulla (Figure 4a) and in the renal cortex (Figure 4b) using the non-Dixon- and Dixon-based CEST analysis. Note that the Dixon-based CEST analysis led to overall lower range of variability of the data sets.

Discussion

CEST MRI in the human kidney is considered challenging due to the physiological motion, severe field inhomogeneity and presence of the surrounding adipose tissue, including perirenal and renal sinus fat. In this preliminary study, we addressed these issues to some extent by developing a MR acquisition protocol and a post-processing workflow for measuring chemical exchange saturation transfer effects in the renal graft tissue.

Previous studies in the human breast (31; 42) have shown that the strong lipid signals can lead to an erroneous amide CEST contrast. Hence, for a reliable in vivo CEST quantification, the fat contribution has

to be eliminated from the total MR signal without affecting the water signal. Although a number of different fat suppression techniques such as spectral pre-saturation with inversion recovery (SPIR), spectral attenuated inversion recovery (SPAIR), spectral fat saturation, and short tau inversion recovery (STIR) are available, their potential application with CEST in renal graft is limited owing to the large B_0 and B_1 inhomogeneity that can severely deteriorate the spectral- and excitation selectivity of the preparation pulses. Furthermore, a combination of the fat-selective- and/or inversion RF pulses with the CEST saturation pulse train may lead to the pulse profile instability and higher total specific absorption rate (SAR) (31). To overcome these disadvantages, the fat suppression capability of Dixon method on CEST imaging has previously been explored (43; 44; 31).

Here the 2-pt Dixon-based CEST method was validated in an egg phantom and in vivo in renal transplant recipients. The results of the phantom experiment showed that in the lipid-abundant egg yolk the large CEST peak at -3.5 ppm was effectively reduced after applying Dixon method, whereas the z-spectra in the protein-rich egg white obtained with and without Dixon were similar. This indicates that the Dixon water-fat decomposition does not introduce any additional asymmetries to the CEST spectrum, which is consistent with the previous findings (31). The in vivo findings confirmed the utility of the Dixon method for fat suppression. There were no statistically significant differences in the hydroxyl and amine MTR_{asym} values obtained with and without Dixon. At the same time, the amide CEST effect at 3.5 ppm was significantly higher in the water-only images than in the IP images. Previous studies reported that the appearance of the z-spectrum in the presence of fat is strongly influenced by the fat fraction and echo time. Whereas in the IP images this influence is quite straightforward, the OP images show much more complicated pattern, as water and phase magnetizations have a phase difference of $(2n+1)\pi$. Thus, the OP CEST acquisition may lead to erroneous higher MTR_{asym} values compared to the Dixon-based CEST analysis. Our study tends to support this observation. Furthermore, the variability of the Dixon-MTR_{asym} values was slightly reduced compared with the non-Dixon CEST values. A possible explanation for this could be the

fact that a single water-only image is produced using two CEST scans acquired at different echos, resulting in higher signal-to-noise ratio (SNR).

Nevertheless, there are some concerns regarding the combination of CEST acquisition and Dixon post-processing. Firstly, the Dixon-based separation model usually requires nonsaturated water and fat peaks. This assumption is clearly violated when performing CEST imaging. Secondly, only a single-peak fat model was assumed here, which accounts for about 70% of the total fat protons. In fact, two other fat peaks at about -3.8 ppm and 0.6 ppm may affect the amide and hydroxyl CEST contrast, respectively (45; 46).

To the best of our knowledge, this work is the first to measure in vivo CEST effects in the renal graft tissue on a clinical MRI system. In line with prior research, the highest MTR_{asym} values was obtained at approximately 1 ppm (15; 47), indicating that a major contributor to the total CEST effect in the kidney is urea. However, several other abundant kidney compounds such as creatinine, creatine, glutamine, glutamate, alanine and allantoin show a detectable CEST effect under physiological conditions at 3T as well, and thus might potentially overlap with the urea CEST signal measured in vivo (32). Our preliminary data in 12 revealed high inter-subject variability in the MTR_{asym} values. Because renal pH and metabolite concentrations are influenced by the kidney function (48), we believe that the relatively large standard deviations observed in the current study could be due to the strong pH- and concentration-dependence of the CEST effects from different kidney metabolites.

The current study has several limitations worth-noting. Firstly, our cohort of patients with kidney transplants was small and there was no control group. Since the transplanted kidneys were hardly affected by breathing motion, respiratory gating/triggering and post-processing registration were not. In contrast, proper motion correction technique need to be applied to circumvent the problem of renal respiratory motion and further, to provide a reliable estimation of the CEST effects in the native kidney. Nevertheless, no prospective movement detection method to correct for kidney displacements was available at the time of our experiments. Secondly, in order to obtain an accurate field map that is critical for in vivo CEST

224 quantification, an additional water saturation shift referencing (WASSR) scan was performed after the
225 CEST acquisition. In fact, it has previously been shown that the multi-echo Dixon method can provide an
226 embedded B_0 map estimated directly from the CEST data collected at different echo times (44; 31).
227 However, there are several challenges that make this approach difficult to apply in the transplanted kidney,
228 including poor signal-to-noise ratio (SNR), phase-wrapping artifacts due to large susceptibility effects
229 secondary to bowel gas (49), and chemical-shift. As an alternative to the WASSR approach used here, a
230 new field-inhomogeneity correction method that allows simultaneous mapping of the water shift and B_1
231 (WASABI) could be applied in future studies (51). Thirdly, this study did not regulate dietary and fluid intake
232 of patients (52). We speculate that this might be one of the reasons for the high MTR_{asym} variability. In
233 particular, the urea-weighted CEST effect at ca. 1 ppm measured in the healthy human kidney has
234 previously been shown to be strongly influenced by the hydration status (47). Effects of hydration status
235 and diet on CEST need to be validate in further studies.

236 Due to the limited number of kidney graft patients examined in this preliminary work, a statistically valid
237 correlation between the CEST values and kidney function as measured by glomerular filtration ratio (eGFR)
238 was not possible. Future studies with a larger cohort of renal transplant recipients with varying eGFR are
239 required to explore the potential of CEST imaging in assessing kidney (graft) function.

240 Besides multi-point Dixon, a further interesting approach to correct for fat signal–induced artifacts that
241 uses the residual signal at the spectral position of the direct water saturation has been proposed lately
242 (42). However, its potential applicability in the human kidney still has to be evaluated. Another option that
243 eliminates the need for fat suppression is multi-pool Lorentzian fitting of the z-spectrum (53). An additional
244 advantage of this method is the possibility of isolating CEST effects originating from different exchanging
245 moieties. This could enhance the specificity of the CEST imaging in the renal tissue. Nevertheless, further
246 investigations are needed in order to get a better understanding of the competing magnetization transfer
247 (MT) effects in the kidney.

Conclusions

Application of CEST MRI to functionally image human kidney, although promising, is complicated by several factors including large field inhomogeneity, presence of fat, and respiratory and bowel motion. In this initial study, we demonstrated for the first time the feasibility of performing CEST imaging in the human kidney transplant on a clinical MRI system. By applying an optimized acquisition protocol and a post-processing pipeline we were able to (i) separate water and fat using a two-point Dixon technique, and to (ii) quantify hydroxyl, amine and amide CEST effects in the renal tissue. In line with the literature, the highest CEST contrast was measured at frequency offset around 1 ppm, indicating urea as a major contributor to the total CEST signal. Furthermore, we confirmed that the conventional APT effect measured in the renal tissue tends to be slightly underestimated in the IP images, and overestimated in the OP images due to the confounding fat contribution. The two-point Dixon-based CEST method implemented here increased the specificity of the APT contrast by correcting the fat-induced artifacts and might facilitate the implementation of CEST technique for functional renal (graft) imaging.

Acknowledgments

The authors thank Erika Rädisch for her assistance in gathering the MRI scans, and Eric Bechler and Dr. Helge Zöllner for their help in the data post-processing and visualization.

The study was supported by a grant from the Forschungskomission of the Faculty of Medicine, Heinrich-Heine-University, Düsseldorf (Grant No. 13/2015).

References

1 Abecassis Michael, Bartlett Stephen T, Collins Allan J, et al. Kidney Transplantation as Primary Therapy for End-Stage Renal Disease: A National Kidney Foundation/Kidney Disease Outcomes. Quality

Initiative (NKF/KDOQI™) Conference *Clinical Journal of the American Society of Nephrology.* 2008;3:471 LP - 480.

2 Wang Yu-Ting, Li Ying-Chun, Yin Long-Lin, Pu Hong, Chen Jia-Yuan. Functional assessment of transplanted kidneys with magnetic resonance imaging. *World journal of radiology.* 2015;7:343– 349.

3 Rush D, Nickerson P, Gough J, et al. Beneficial effects of treatment of early subclinical rejection: a randomized study. *Journal of the American Society of Nephrology.* 1998;9:2129 LP - 2134.

4 Pascual Julio, Pérez-Sáez Maria J., Mir Marisa, Crespo Marta. Chronic renal allograft injury: early detection, accurate diagnosis and management. *Transplantation Reviews.* 2012;26:280–290.

5 Eijs Mick J M, Zuilen Arjan D, Boer Anneloes, et al. Innovative Perspective: Gadolinium-Free Magnetic Resonance Imaging in Long-Term Follow-Up after Kidney Transplantation 2017.

6 Hogan Jonathan J, Mocanu Michaela, Berns Jeffrey S. The Native Kidney Biopsy: Update and Evidence for Best Practice *Clinical journal of the American Society of Nephrology : CJASN.* 2016;11:354–362.

7 Aktaş Ayşe. Transplanted Kidney Function Evaluation *Seminars in Nuclear Medicine.* 2014;44:129–145.

8 Neimatallah Mohammed A, Dong Qian, Schoenberg Stefan O, Cho Kyung J, Prince Martin R. Magnetic resonance imaging in renal transplantation *Journal of Magnetic Resonance Imaging.* 1999;10:357–368.

9 Ljimani A, Wittsack HJ, Lanzman RS. Functional MRI in transplanted kidneys. *Abdom Radiol (NY)*. 2018;43(10):2615-2624. doi:10.1007/s00261-018-1563-7.

10 Schutter R, Lantinga VA, Borra RJH, Moers C. MRI for diagnosis of post-renal transplant complications: current state-of-the-art and future perspectives. *Magn Reson Mater Phy* **33,** 49–61 (2020).

11 Lanzman Rotem S, Ljimani Alexandra, Pentang Gael, et al. Kidney Transplant: Functional Assessment with Diffusion-Tensor MR Imaging at 3T. *Radiology.* 2013;266:218–225.

12 Haris Mohammad, Nanga Ravi Prakash Reddy, Singh Anup, et al. Exchange rates of creatine kinase metabolites: feasibility of imaging creatine by chemical exchange saturation transfer MRI. *NMR in Biomedicine.* 2012;25:1305–1309.

13 Kogan Feliks, Haris Mohammad, Debrosse Catherine, et al. In vivo chemical exchange saturation transfer imaging of creatine (CrCEST) in skeletal muscle at 3T. *Journal of Magnetic Resonance Imaging.* 2014;40:596–602.

14 Guivel-Scharen V., Sinnwell T., Wolff S.D., Balaban R.S.. Detection of Proton Chemical Exchange between Metabolites and Water in Biological Tissues. *Journal of Magnetic Resonance.* 1998;133:36–45.

15 Dagher Azar P, Aletras Anthony, Choyke Peter, Balaban Robert S. Imaging of urea using chemical exchange-dependent saturation transfer at 1.5T. *Journal of Magnetic Resonance Imaging.* 2000;12:745–748.

16 Chan Kannie W Y, McMahon Michael T, Kato Yoshinori, et al. Natural D-glucose as a biodegradable MRI contrast agent for detecting cancer. *Magnetic resonance in medicine.* 2012;68:1764–1773.

17 Sehgal Akansha Ashvani, Li Yuguo, Lal Bachchu, et al. CEST MRI of 3-O-methyl-D-glucose uptake and accumulation in brain tumors. *Magnetic Resonance in Medicine.* 2018;81:1993–2000.

18 Zhou Jinyuan, Wilson David A, Sun Phillip Zhe, Klaus Judith A, Zijl Peter C M. Quantitative description of proton exchange processes between water and endogenous and exogenous agents for WEX, CEST, and APT experiments. *Magnetic Resonance in Medicine.* 2004;51:945–952.

19 Goerke Steffen, Breitling Johannes, Zaiss Moritz, et al. Dual-frequency irradiation CEST-MRI of endogenous bulk mobile proteins. *NMR in Biomedicine.* 2018;31:e3920.

20 Wu Yin, Zhou Iris Y, Igarashi Takahiro, Longo Dario L, Aime Silvio, Sun Phillip Zhe. A generalized ratiometric chemical exchange saturation transfer (CEST) MRI approach for mapping renal pH using iopamidol. *Magnetic Resonance in Medicine.* 2018;79:1553–1558.

21 Longo Dario Livio, Busato Alice, Lanzardo Stefania, Antico Federica, Aime Silvio. Imaging the pH evolution of an acute kidney injury model by means of iopamidol, a MRI-CEST pH-responsive contrast agent. *Magnetic Resonance in Medicine.* 2013;70:859–864.

22 Longo Dario Livio, Cutrin Juan Carlos, Michelotti Filippo, Irrera Pietro, Aime Silvio. Noninvasive evaluation of renal pH homeostasis after ischemia reperfusion injury by CEST-MRI. *NMR in Biomedicine.* 2017;30:e3720.

23 Wu Yunkou, Zhang Shanrong, Soesbe Todd C, et al. pH imaging of mouse kidneys in vivo using a frequency-dependent paraCEST agent. *Magnetic Resonance in Medicine.* 2016;75:2432–2441.

24 Wang Feng, Kopylov David, Zu Zhongliang, et al. Mapping murine diabetic kidney disease using chemical exchange saturation transfer MRI. *Magnetic Resonance in Medicine.* 2016;76:1531– 1541.

25 Wang Feng, Takahashi Keiko, Li Hua, et al. Assessment of unilateral ureter obstruction with multi-parametric MRI. *Magnetic Resonance in Medicine.* 2018;79:2216–2227.

26 Liu Jing, Han Zheng, Chen Guoli, et al. CEST MRI of sepsis-induced acute kidney injury. *NMR in Biomedicine.* 2018;31:e3942.

27 Kentrup Dominik, Bovenkamp Philipp, Busch Annika, et al. GlucoCEST magnetic resonance imaging in vivo may be diagnostic of acute renal allograft rejection. *Kidney International.* 2017;92:757–764.

28 Zhang Shu, Li Bian, Greer Joshua, et al. Toward CEST MRI of renal masses: protocol optimization and first preliminary data in *Joint Annual Meeting ISMRM-ESMRMB 2018* 2018.

29 Lu Jianhua, Zhou Jinyuan, Cai Congbo, Cai Shuhui, Chen Zhong. Observation of true and pseudo NOE signals using CEST-MRI and CEST-MRS sequences with and without lipid suppression *Magnetic Resonance in Medicine.* 2015;73:1615–1622.

30 Zhang Shu, Keupp Jochen, Wang Xinzeng, et al. Z-spectrum appearance and interpretation in the presence of fat: Influence of acquisition parameters *Magnetic Resonance in Medicine.* 2018;79:2731–2737.

31 Zhang Shu, Seiler Stephen, Wang Xinzeng, et al. CEST-Dixon for human breast lesion characterization at 3 T: A preliminary study. *Magnetic Resonance in Medicine.* 2018;80:895–903.

32 Stabinska Julia, Neudecker Philipp, Ljimani Alexandra, Wittsack Hans Jörg, Lanzman Rotem Shlomo, Müller-Lutz Anja. Proton exchange in aqueous urea solutions measured by water-exchange (WEX) NMR spectroscopy and chemical exchange saturation transfer (CEST) imaging in vitro. *Magnetic Resonance in Medicine.* 2019;82:935–947.

33 Liu Junmin, Peters Dana C, Drangova Maria. Method of B0 mapping with magnitude-based correction for bipolar two-point Dixon cardiac MRI. *Magnetic Resonance in Medicine.* 2017;78:1862–1869.

34 Jayasundar Rama, Ayyar Savita, Raghunathan P. Proton resonance imaging and relaxation in raw and cooked hen eggs. *Magnetic Resonance Imaging.* 1997;15:709–717.

35 Zhou Jinyuan, Yan Kun, Zhu He. A Simple Model for Understanding the Origin of the Amide Proton Transfer MRI Signal in Tissue. *Applied Magnetic Resonance.* 2012;42:393–402.

36 Kaewmanee Thammarat, Benjakul Soottawat, Visessanguan Wonnop. Changes in chemical composition, physical properties and microstructure of duck egg as influenced by salting. *Food Chemistry.* 2009;112:560–569.

37 Ljimani Alexandra, Caroli Anna, Laustsen Christoffer, et al. Consensus-based technical recommendations for clinical translation of renal diffusion-weighted MRI. *Magnetic Resonance Materials in Physics, Biology and Medicine.* 2019.

38 Kim Mina, Gillen Joseph, Landman Bennett A, Zhou Jinyuan, Zijl Peter C M. Water saturation shift referencing (WASSR) for chemical exchange saturation transfer (CEST) experiments. *Magnetic Resonance in Medicine.* 2009;61:1441–1450.

39 Ren Tao, Wen Cheng-Long, Chen Li-Hua, et al. Evaluation of renal allografts function early after transplantation using intravoxel incoherent motion and arterial spin labeling MRI. *Magnetic Resonance Imaging.* 2016;34:908–914.

40 Yushkevich Paul A., Piven Joseph, Hazlett Heather Cody, et al. User-guided 3D active contour segmentation of anatomical structures: Significantly improved efficiency and reliability. *NeuroImage.* 2006;31:1116–1128.

41 HJ Zöllner, M Považan, SCN Hui, S Tapper, RAE Edden, G Oeltzschner. Comparison of algorithms for linear-combination modelling of short-echo-time magnetic resonance spectra. bioRxiv 2020.

42 Zimmermann Ferdinand, Korzowski Andreas, Breitling Johannes, et al. A novel normalization for amide proton transfer CEST MRI to correct for fat signal–induced artifacts: application to human breast cancer imaging. *Magnetic Resonance in Medicine.* 2019:1–15.

43 Keupp Jochen, Eggers Holger. CEST-dixon MRI for sensitive and accurate measurement of amide proton transfer in humans at 3T in *Proc Intl Soc Mag Reson Med* (Stockholm):18:338, 2010.

44 Togao Osamu, Keupp Jochen, Hiwatashi Akio, et al. Amide proton transfer imaging of brain tumors using a self-corrected 3D fast spin-echo dixon method: Comparison With separate B0 correction *Magnetic Resonance in Medicine.* 2017;77:2272–2279.

45 Hamilton Gavin, Yokoo Takeshi, Bydder Mark, et al. In vivo characterization of the liver fat 1H MR spectrum. *NMR in Biomedicine.* 2011;24:784–790.

46 Wang Xiaoke, Hernando Diego, Reeder Scott B. Sensitivity of chemical shift-encoded fat quantification to calibration of fat MR spectrum. *Magnetic resonance in medicine.* 2016;75:845–851.

47 Vinogradov Elena, Liu Zheng, Madhuranthakarn Ananth, et al. Endogenous urea CEST (urCEST) for MRI monitoring of kidney function in *In Proceedings of the 23th Annual Meeting and Exhibition of ISMRM*(Toronto, Canada) 2015.

48 Goek Oemer-Necmi, Prehn Cornelia, Sekula Peggy, et al. Metabolites associate with kidney function decline and incident chronic kidney disease in the general population. *Nephrology Dialysis Transplantation.* 2013;28:2131–2138.

49 Bechler E., Stabinska J., Wittsack H.-J.. Analysis of different phase unwrapping methods to optimize quantitative susceptibility mapping in the abdomen. *Magnetic Resonance in Medicine.* 2019;82.

50 Schuenke Patrick, Windschuh Johannes, Roeloffs Volkert, Ladd Mark E, Bachert Peter, Zaiss Moritz. Simultaneous mapping of water shift and B1(WASABI)—Application to field-Inhomogeneity correction of CEST MRI data. *Magnetic Resonance in Medicine.* 2017;77:571– 580.

51 Windschuh Johannes, Zaiss Moritz, Ehses Philipp, Lee Jae-Seung, Jerschow Alexej, Regatte Ravinder R. Assessment of frequency drift on CEST MRI and dynamic correction: application to gagCEST at 7 T. *Magnetic resonance in medicine.* 2019;81:573–582.

52 Ljimani, A., Caroli, A., Laustsen, C. *et al.* Consensus-based technical recommendations for clinical translation of renal diffusion-weighted MRI. *Magn Reson Mater Phy* **33,** 177–195 (2020).

53 Cai Kejia, Singh Anup, Poptani Harish, et al. CEST signal at 2ppm (CEST@2ppm) from Z-spectral fitting correlates with creatine distribution in brain tumor. *NMR in Biomedicine.* 2015;28:1–8.

Figures and Tables Captions

Figure 1: The z-spectra obtained in the (A) egg white and (B) egg yolk from the CEST images collected close to IP, and water-only CEST images.

403 **Figure 2:** Representative (A) T2-weighted anatomical image of the lower abdomen, and corresponding (B)
404 fat and (C) water maps obtained using the Dixon post-processing.

405 **Figure 3:** Exemplary (A, B) z-spectra and (C, D) MTR_{asym} curves measured with and without Dixon in the
406 renal medulla and cortex.

407 **Table 1:** MTR_{asym}% values obtained with and without Dixon in three frequency ranges in the renal medulla
408 and cortex.

409 **Figure 4:** Boxplots comparing the MRT_{asym} values obtained from the Dixon-, IP- and OP- CEST data in the
410 (A) renal cortex and (B) medulla.

411 ## Figures and Tables

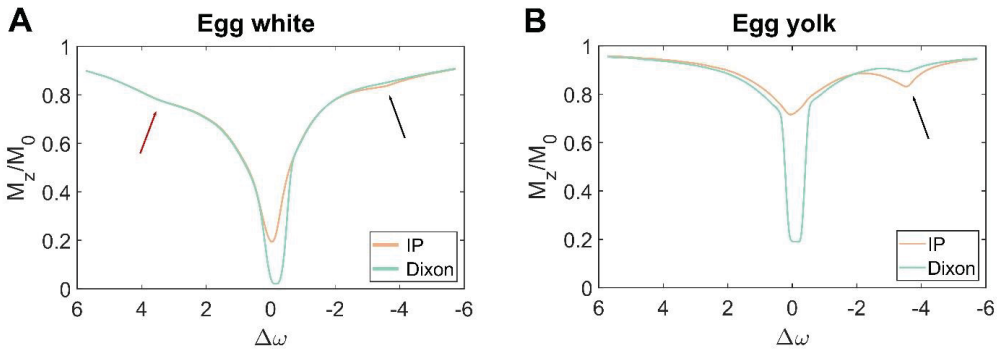

412

413 **Figure 1**

414

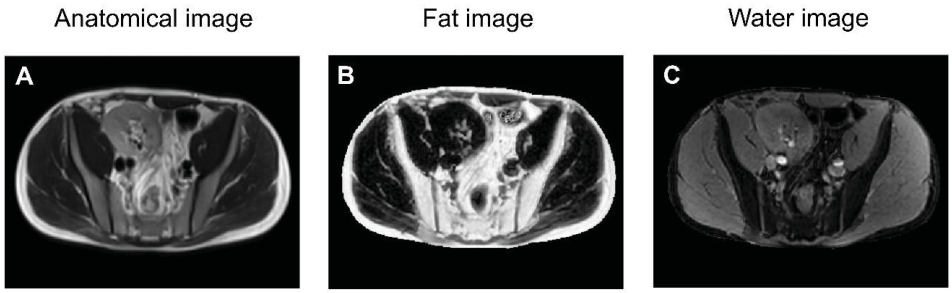

415

416 **Figure 2**

417

418

419

420

421

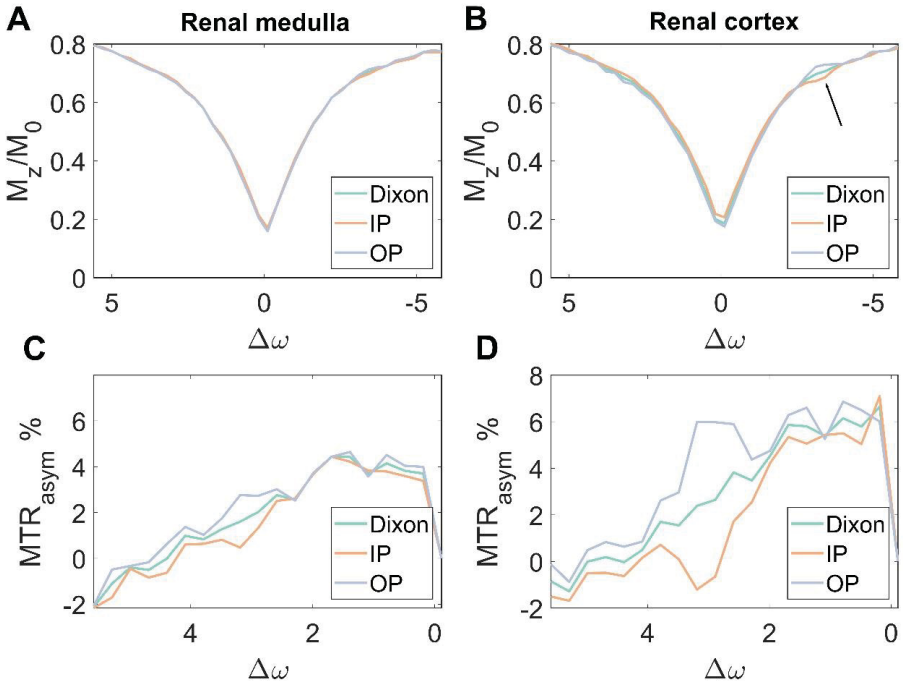

Figure 3

Table 1:

	MTR_{asym}% (IP)			MTR_{asym}% (OP)			MTR_{asym}% (Dixon)		
	0.8-1.2 ppm	1.8-2.2 ppm	3.3-3.7 ppm	0.8-1.2 ppm	1.8-2.2 ppm	3.3-3.7 ppm	0.8-1.2 ppm	1.8-2.2 ppm	3.3-3.7 ppm
Renal medulla (n = 12)	3.0 ± 2.1	1.5 ± 1.1	-0.12 ± 0.78	3.0 ± 2.2	1.6 ± 1.1	0.8 ± 0.9	3.0 ± 2.1	1.6 ± 1.0	0.32 ± 0.62
Renal cortex (n = 12)	2.7 ± 2.4	1.1 ± 1.5	-1.0 ± 1.0	2.9 ± 2.6	1.6 ± 1.5	0.8 ± 0.9	2.5 ± 1.4	1.4 ± 1.4	-0.06± 0.62

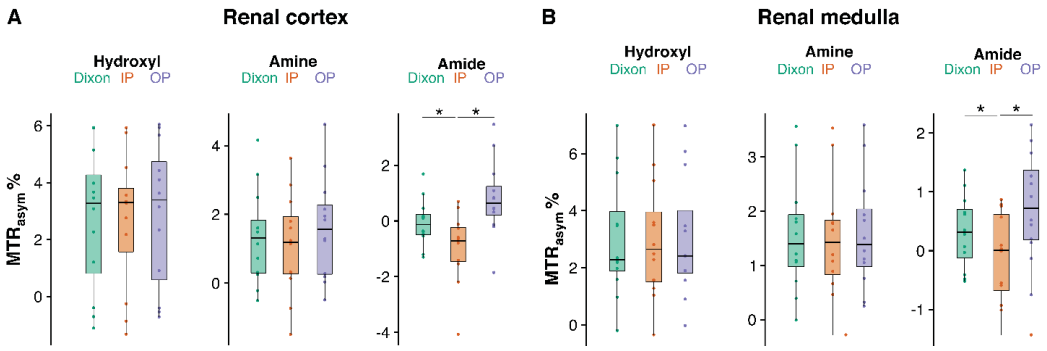
A
Renal cortex
B
Renal medulla
Hydroxyl
Amine
Amide
Dixon IP OP
MTR asym %
*
*

Figure 4

Appendix D

Other Publications

Other relevant publications:

Publication 4

Müller-Lutz A, Ljimani A, Stabinska J, Zaiss M, Boos J, Wittsack HJ, Schleich C. Comparison of B0 versus B0 and B1 field inhomogeneity correction for glycosaminoglycan chemical exchange saturation transfer imaging. Magn Reson Mater Phy. 2018; 31(5):645-651. doi: 10.1007/s10334-018-0689-5

Impact factor (2019): 2.836

Personal contribution: 15% (data analysis, manuscript drafting)

Publication 5

Lanzman RS, Ljimani A, Müller-Lutz A, Weller J, Stabinska J, Antoch G, Wittsack HJ. Assessment of time-resolved renal diffusion parameters over the entire cardiac cycle. Magn Reson Imaging. 2019; 55:1-6. doi: 10.1016/j.mri.2018.09.009.

Impact factor (2019): 2.112

Personal contribution: 5% (manuscript drafting)

Publication 6

Bechler E, Stabinska J, Wittsack HJ. Analysis of different phase unwrapping methods to optimize quantitative susceptibility mapping in the abdomen. Magn Reson Med. 2019; 82(6):2077-2089. doi: 10.1002/mrm.27891.

Impact factor (2019): 3.858

Personal contribution: 15% (manuscript drafting)

Publication 7

Stabinska J, Ljimani A, Frenken M, Feiweier T, Lanzman RS, Wittsack HJ. Comparison of PGSE and STEAM DTI Acquisitions with Varying Diffusion Times for Probing Anisotropic Structures in Human Kidneys. 2020; 84(3):1518-1525. doi: 10.1002/mrm.28217.

Impact factor (2019): 3.858

Personal contribution: 80% (data acquisition, data analysis, data interpretation, manuscript writing, manuscript revision)

Publication 8

Abrar DB, Schleich C, Radke KL, Frenken M, Stabinska J, Ljimani A et al. Detection of early cartilage degeneration in the tibiotalar joint using 3T gagCEST imaging: a feasibility study. *Accepted in Magn Reson Mater Phy*

Impact factor (2019): 1.956

Personal contribution: 5% (MRI sequence development, manuscript drafting)

Publication 9

Ljimani A, Hojdis M, Stabinska J, Valentin B, Frenken M, Appel E et al. Analysis of different image- registration algorithms for Fourier decomposition MRI in functional lung Imaging. *Accepted in Acta Radiol*

Personal contribution: 5% (manuscript drafting)

Publication 10

Bechler E, Stabinska J, Jasse J, Zukovs R, Valentin B, Antoch G et al. Quantitative Susceptibility Mapping (QSM) of the human kidney. *Under Review in Magn Reson Mater Phy*

Personal contribution: 10% (manuscript drafting)

Publication 11

Stabinska J, Ljimani A, Zöllner HJ, Wilken E, Limber J, Esposito I et al. Spectral Diffusion Analysis of Kidney Intravoxel Incoherent Motion MRI in Healthy Volunteers and Patients with Renal Pathologies. *Submitted to Magn Reson Med*

Personal contribution: 80% (data acquisition, data analysis, data interpretation, manuscript writing, manuscript revision)